DESIGN AND CONSTRUCTION OF AN EXPERIMENTAL APPARATUS FOR THE INTERFEROMETRIC MEASUREMENT OF MICROMETER LEVEL CLEARANCES

A THESIS SUBMITTED TO
THE GRADUATE SCHOOL OF NATURAL AND APPLIED SCIENCES
OF
MIDDLE EAST TECHNICAL UNIVERSITY

BY

MURAT YILDIRIM

IN PARTIAL FULLFILMENT OF THE REQUIREMENTS
FOR
THE DEGREE OF MASTER OF SCIENCE

IN

MECHANICAL ENGINEERING

JUNE 2009

Approval of the thesis:

DESIGN AND CONSTRUCTION OF AN EXPERIMENTAL APPARATUS FOR THE INTERFEROMETRIC MEASUREMENT OF MICROMETER LEVEL CLEARANCES

submitted by **MURAT YILDIRIM** in partial fulfillment of requirements for the degree of **Master of Science in Mechanical Engineering Department, Middle East Technical University** by,

Prof. Dr. Canan Özgen _____
Dean, Graduate School of **Natural and Applied Sciences**

Prof. Dr. Suha Oral _____
Head of Department, **Mechanical Engineering**

Prof. Dr. Zafer Dursunkaya _____
Supervisor, **Mechanical Engineering Dept., METU**

Assist. Prof. Dr. Tuba Okutucu Özyurt _____
Co-Supervisor, **Mechanical Engineering Dept., METU**

Examining Committee Members

Prof. Dr. Rüknettin Oskay _____
Mechanical Engineering Dept., METU

Prof. Dr. Zafer Dursunkaya _____
Mechanical Engineering Dept., METU

Prof. Dr. Metin Akkök _____
Mechanical Engineering Dept., METU

Assist. Dr. Tuba Okutucu Özyurt _____
Mechanical Engineering Dept., METU

Dr. Hüsnü Kerpiççi _____
R&D Dept., ARÇELİK

Date

_____

I hereby declare that all information in this document has been obtained and presented in accordance with academic rules and ethical conduct. I also declare that, as required by these rules and conduct, I have fully cited and referenced all material and results that are not original to this work.

Name, Last Name: Murat YILDIRIM

Signature :

ABSTRACT

DESIGN AND CONSTRUCTION OF AN EXPERIMENTAL APPARATUS FOR THE INTERFEROMETRIC MEASUREMENT OF MICROMETER LEVEL CLEARANCES

Yıldırım, Murat

M.Sc., Department of Mechanical Engineering

Supervisor : Prof. Dr. Zafer Dursunkaya

Co-Supervisor : Assist. Prof. Dr. Tuba Okutucu Özyurt

June 2009, 179 pages

In this study a fiber optic interferometer (FOI) was designed and constructed to measure micron level clearances occurring in piston cylinder arrangements. A Cartesian model of the piston cylinder assembly is manufactured and lateral motion and vertical displacement are generated via a step motor, and micrometers, respectively. Clearance measurements are conducted in air and also in a lubricant. The range of vertical displacements is kept between 0-50 μm, and the lateral motion is 13.5 mm. The effect of the step motor and lateral motion carriage on distance measurement is determined and this is used to correct displacement measurements.

Keywords: Micron level clearances, lubrication, fiber optic interferometry, Fourier transform.

ÖZ

MİKROMETRE MERTEBESİNDEKİ BOŞLUKLARIN ENTERFEROMETRİK ÖLÇÜMÜNE DAYANAN DENEYSEL DÜZENEĞİN TASARIMI VE KURULUMU

Yıldırım, Murat
Yüksek Lisans, Makine Mühendisliği Bölümü
Tez Yöneticisi : Prof. Dr. Zafer Dursunkaya
Ortak Tez Yöneticisi : Yrd. Doç. Dr. Tuba Okutucu Özyurt

Haziran 2009, 179 sayfa

Bu çalışmada fiber optik girişimölçer (FOI) tasarımı ve kurulumu piston silindir sistemlerinde görülen mikrometre seviyelerindeki mesafeleri ölçmek amacıyla gerçekleştirilmiştir. Piston silindir sisteminin kartezyen kordinat düzlemindeki modeli üretilmiş ve bu modelde yatay ve dikey yönlerdeki hareketler sırasıyla step motor ve mikrometreler aracılığıyla sağlanmıştır. Mesafe ölçümleri hem havada hem de kırılma indisi ölçülen yağ tabakası kullanılarak yapılmıştır. Dikey yöndeki yer değiştirme miktarı 0-50 mikrometre arasında değiştirilmiş ve yatay yöndeki hareket miktarı ise 13.5 milimetreye sabitlenmiştir. Deney sonuçları incelendiğinde step motorun ve yatay hareketi sağlayan mekanizmanın ölçümlerdeki etkileri belirlenmiştir. Bu etkiler uzeklık hesaplamalarından çıkarılarak dikey yöndeki yer değiştirmeler daha hassas bir şekilde ölçülmüştür.

Keywords: Mikron seviyesindeki boşluklar, yağlanma, fiber optik girişim ölçer, Fourier transform.

To My Family and My Love

ACKNOWLEDGEMENTS

The author wishes to express his deepest gratitude to his supervisor Prof. Dr. Zafer Dursunkaya and his co-supervisor Assist. Prof. Dr. Tuba Okutucu Özyurt for their guidance, advice, criticism, encouragements and insight throughout the research.

The author wishes to mention his gratitude to Mrs. İlkay Ayaz for her encouragement, patience and support from the beginning to the end of this study.

Technical assistance of Mr. Mustafa Yalçın is gratefully acknowledged.

The author would also like to thank research assistants Mr. Bekir Bediz, Mr. Salih Alan, Mr. Hakan Çalışkan and Sparc research group members Mr. Serdar Üşenmez, Mr. Ulaş Yaman and Mr. Barış Ragıp Mutlu for their support to perform different tasks in this study.

The refractive index and the AFM measurements are conducted at the Central Lab of Middle East Technical University (METU).

This study was supported by The Scientific and Technological Research Council of Turkey (TUBITAK). Moreover, ARÇELİK ARGE is the industrial partner in this study.

TABLE OF CONTENTS

LIST OF TABLES

TABLES

LIST OF FIGURES

FIGURES

LIST OF SYMBOLS

I : total intensity detected by photo detector

I_1 : reference signal intensity

I_2 : sensing signal intensity

N : number of fringes

n : refractive index of the cavity

d : cavity length

h_1 : distance between probe end and reference setting at the beginning

h_2 : distance between probe end and reference setting at the end

Δh : height difference between h_1 and h_2

δ : total phase difference

I_{max} : constructive interference intensity

I_{min} : destructive interference intensity

V : visibility of the interference fringes

Δr : coherence length

λ : wavelength of the laser

R_1 : reflectivity of the end face of the fiber

ε : ratio of gap and the coherence length of the laser

R : reflectivity of an external mirror

H_1 : distance between left micrometer and reference setting

H_2 : distance between right micrometer and reference setting

L_p : horizontal displacement of probes

L_m : horizontal distance between the micrometers

$\Delta\phi$: total phase difference in the numerical code

A : average of summation of the local maximum and minimum intensities in the numerical code

B : average of difference of the local maximum and minimum intensities in the numerical code

a, b, c : coefficients of generated pure cosines and exponentially decaying functions

∂I : partial derivative of detected intensity

∂x : partial derivative of measured clearance

$\overrightarrow{E_1}$: electric field vector of the first wave

$\overrightarrow{E_2}$: electric field vector of the second wave

$\overrightarrow{k_1}$: propagation vector of the first wave

$\overrightarrow{k_2}$: propagation vector of the second wave

ω : frequency of the both waves

$\vec{r}$: position vector of the both waves

ε_1 : phase of the first wave

ε_2 : phase of the second wave

$\overrightarrow{E_p}$: electric field vector of the disturbance wave

CHAPTER 1

INTRODUCTION

Ringless small reciprocating hermetically sealed compressors are widely used to compress coolant gas in household refrigerators and air conditioners. In them the piston becomes a key component influencing all major performance criteria of reciprocating compressor, such as pumping efficiency, noise, power consumption, wear, and so on. This is because of the fact that piston dynamics characterizes oil leakage, piston slap phenomenon and frictional loss, which determine performance. While moving up and down along the lubricated cylinder wall, a piston displays oscillatory radial translation and rotation within the oil film clearance owing to the unbalance of dynamic forces acting on it. Understanding this secondary motion in piston dynamics has become a crucial research subject in order to improve the performance of reciprocating compressor. The piston-pin and piston-cylinder clearances encountered in hermetically sealed compressor are of the order of 5 μm, much smaller than conventional applications, such as automotive pistons, where the clearances are of the order of 30-500 μm. The power loss in these bearings account for a substantial percentage of the total loss, in addition, wear encountered in these bearings affects the reliability of the compressor. The presence of elastic deformations of the surfaces under the effect of the hydrodynamic and boundary pressures is a complicating factor, which needs to be accounted for in the analysis. Therefore, the detection of clearances and the lubricant thickness occurring in the hermetically sealed compressors is important to design new piston-cylinder arrangements to reduce the power loss, friction and wear rates in the piston-cylinder mechanism.

1.1 Aim of the Study

Currently, there is an increasing demand of high technology household appliances. Moreover, the total power requirement of the household appliances such as refrigerators, washing machines, air conditioners, ovens continues to increase due to the effect of the increase in the human population and economic growth.

Refrigerators are widely used in today's world. Although the principle of refrigeration has not changed since its introduction, the design of the components of the refrigerators has changed to minimize power consumption. The energy need of the developing world has started to increase. Since energy sources are scarce, every industry needs to limit their energy consumption levels. Therefore, energy consumption level of the refrigerators is a key factor for the manufacturers. Since the compressors are the components which require work input to compress the refrigerant in the refrigerators, the design of the compressors is important to minimize the power consumption of the refrigerators.

In this study, a Cartesian model of the piston-cylinder mechanism is manufactured to measure clearances with the same magnitude of the clearances occurring in hermetically sealed compressors. The experimental technique is based on fiber optic interferometry since the radial clearances occurring in the piston cylinder system is of the order of 5 μm. The feasibility of installation of this experimental method to a working hermetically sealed compressor piston cylinder mechanism is investigated in this project. This project is sponsored by The Scientific and Technological Research Council of Turkey (TUBITAK). Arçelik ARGE Inc. is the industrial partner in this project.

1.2 Hermetically Sealed Compressors

Vapor-compression refrigeration cycle is the most preferred one used in household refrigerators. The schematic view of the vapor compression cycle is shown in Figure 1.1.

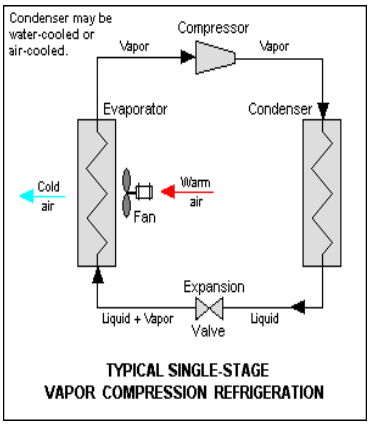

Figure 1.1. Schematic view of vapor compression refrigeration cycle [1]

In this cycle, the refrigerant enters the compressor with low pressure and exits with higher pressure and it enters the condenser in which it condenses because of the heat transfer to the low temperature surroundings. Then, it leaves the condenser in the liquid phase and it is directed to the expansion valve where the pressure of the refrigerant decreases. After leaving the expansion valve, the refrigerant is a two-phase mixture with a lower pressure and then enters the evaporator in which heat is transferred from the refrigerated space to the refrigerant and the refrigerant leaves the evaporator as vapor and then it again enters the compressor.

The compressors used in refrigerators are hermetically sealed because of the high stability, reliability of these devices.

1.3 Lubrication

Lubrication is the process, or technique employed to reduce wear of one or both surfaces in close proximity, and moving relative to each another, by interposing a substance, a lubricant, between the surfaces to carry or to help carry the load (pressure generated) between the opposing surfaces. The interposed lubricant film can be a solid, (eg graphite, MoS_2) a solid/liquid dispersion, a liquid, a liquid-liquid dispersion (greases) or exceptionally a gas. There are different types of lubrication:

a) Hydrodynamic
b) Hydrostatic
c) Elastohydrodynamic
d) Boundary
e) Solid-film

In hydrodynamic lubrication, there is a lubricant between the load carrying surfaces to prevent their contact. The mechanism occuring in hydrodynamic lubrication can be explained with the laws of fluid mechanics [2].

In hydrostatic lubrication, there is also a lubricant in the load-bearing area with a higher pressure to separate the surfaces. However, there is no need to have a relative motion of the surfaces as in the hydrodynamic lubrication.

In elastohydrodynamic lubrication, there is a rolling contact and the lubricant is used within these contacts.

When there is a drop in the velocity of a moving surface, an increase in the load of the bearing, increase in the lubricant temperature, the formation of hydrodynamic lubricant can be prevented. Therefore, the asperities can be separated with a thin lubricant film. This is called boundary lubrication.

Solid film lubrication occurs when the bearings should operate in extreme temperatures.

1.4 Piston Lubrication

The dimensions of the piston cylinder mechanism used in hermetically sealed compressors are shown in Figure 1.2.a and Figure 1.2.b.

(a)

(b)

Figure 1.2 Photo of piston cylinder assembly

As it can be seen from Figure 1.2 that the bore of the piston cylinder mechanism is approximately 2 cm and the length of the piston cylinder mechanism is approximately equal to 3 cm. The piston makes reciprocating motion in the

cylinder. First, the refrigerant is taken into the cylinder and compressed by the piston and then refrigerant leaves the compressor. The photo of the piston is shown in Figure 1.3.

Figure 1.3 Piston

There is a circumferential oil groove on to the piston. There are holes on the oil groove opening on the compressor side of the piston.

CHAPTER 2

LITERATURE SURVEY

There is numerous literature regarding the lubricant thickness measurement and fiber optic interferometry.

Hu et.al [3] summarizes recent progress in investigation of nano-rheology and thin film lubrication, as well as their contribution to conventional tribology. As the thickness of a lubricating film becomes comparable to molecular dimensions, a lubricant confined between solid walls undergoes a dramatic transition in its rheological properties and physical state, including the formation of ordered structure, enhanced viscosity and slow relaxation, glass transition or solidification, and consequent stick-slip motion. As a result, it is recognized that there is a special regime between EHL and boundary lubrication, identified as thin film lubrication, where lubricant flow and hydrodynamics are still in action but behave differently from expectations of the classical theory. Generalized theories of thin film lubrication are under development. Microscopic studies of thin film lubrication provide a solid theoretical basis to the development of high-tech and micro devices, the understanding of lubrication failure, the generalization of classical lubrication theory, and friction control and interface design. Zhang summarizes the recent researches on thin film lubrication (TFL), which involves the origin of the TFL concept, advancement of measuring techniques, TFL film-forming features, investigation on its mechanism, and computation theories. A key problem in the investigation of the characteristics of TFL is to devise an available rig for measuring the film thickness. The determination of lubricant film thickness distribution is of crucial importance for understanding many physical and chemical processes occurring in such contacts. The family of techniques based on optical interferometry is one of the most important contributors to experimental research [4].

Cann et.al [5] mentioned that conventional interferometry has two major limitations that prevent it from being able to measure very thin films. One is that, for optical interference to occur, the optical path difference must be at least half of the wavelength of the light, which means that it is not practical to measure films less than about one-quarter of the wavelength of the light, i.e. about 50 nm. The second is an inherent inability of the human eye accurately to distinguish interference colors, which means that measurement resolution is limited to about ± 10 nm . The limitations of optical interferometry give impetus to further extensions so as to enable it capable for measuring lubricant film thickness falling down to a few nanometers. In 1991, Johnston et al. used a method of spacer layer in combination with the spectrum analysis of reflective light to expand the interference technique, enabling it available to measure thin film thickness down to nano scale[6]. In 1994, Luo and Huang et al. implemented a relative optical reference intensity method to measure film thickness, which has a vertical resolution of 0.5 nm [7]. Later, in 1999, Hartl and co-workers measured film thickness down to 5 nm by applying the colorimetric interferometry technique [8]. Recently, the multi beam based interference method also reported the measured film thickness value down to about 1 nm [9]. Spikes reviews the various experimental techniques that have contributed to an understanding of elastohydrodynamic (EHD) lubrication. After a brief historical overview, attention focuses on the main methods for studying the behavior of lubricant films in lubro, within EHD contacts, in particular ultra thin film interferometry, film thickness mapping, in-contact infrared and Raman spectroscopy, fluorescence and temperature/shear stress mapping. From this review, the important role of the experimentalist in the study of EHD lubrication is identified and appreciated [10]. Krupka et al. uses colorimetric interferometry to study the EHD lubrication of point contacts under pure rolling conditions to obtain lubricant film shapes with high accuracy and resolution. An RGB CCD camera together with extensive image processing software has enabled real time evaluation of chromatic interferograms. The classical numerical isothermal solution of EHD lubrication of point contacts has been used for the comparison with three-dimensional representations of film thickness distributions obtained from experiments. A good agreement was found between experimental and numerical

EHD film shapes by comparing lubricant film profiles and positions of minimum film thickness. Both experimental results and numerical solution confirm the ratio between central and minimum film thickness to change significantly with operating conditions [11]. Glovnea et. al [12] used ultra-thin film interferometric method for measuring the thickness of very thin films in lubricated contacts. Therefore, it has been refined so as to be able to measure films down to 0.3 nm with a Standard deviation of 0.15 nm. The main remaining source of measurement variation for films below 3 nm thick is the surface roughness of the contacting solids. This modified technique has been applied to study the film forming properties of the three fluids, hexadecane, a dilute solution of surfactant in hexadecane, and cyclohexane. Purified hexadecane shows slightly enhanced oil-film thickness below 1 nm. The long-chain surfactant forms a boundary film 2 nm thick. Cyclohexane behaves as though it forms a surface layer about 1 nm thick with viscosity three times the bulk fluid viscosity. Guo and Wong [13] introduces a newly developed lubricating film thickness measuring system, which implements the multi-beam intensity based (MBI) scheme. Some details about the software of the testing system and instrumentation of the MBI approach are discussed. For efficient determination of the fringe order range of measured points, a simple counting strategy was suggested. It is shown that this measuring system can provide a measurement range from nano to micrometers and a high resolution on the nanometer level. Besides being able to detect ultra thin lubricating film thickness, the system can also measure tiny local variations in film thickness on a nano-scale in the conventional EHL regime. The capability of the system is demonstrated by the determination of film thickness in the range of 1 nm to 2.542 μm with a standard deviation of 0.89 nm. Cho and Moon [14] emphasized the influence of the piston secondary motion on the major characteristics of lubrication in a reciprocating compressor, such as the oil leakage, the piston slap phenomenon and the frictional power loss. Therefore, they concentrated on the finite element analysis for the piston dynamic response. By coupling FDM for the lubricating pressure field with FEM for the piston dynamic piston motion, they numerically approximate the lubricant-structure interaction in a reciprocating compressor. Prata et al. made dynamic analysis of piston secondary motion for small reciprocating compressors.

The results of this study explored the effects of some design parameters and operating conditions on the stability of the piston, the oil leakage, and friction losses [15].

There are also several studies related to the fiber optic interferometry applications. The first one related with a fiber optic interferometric sensor for the dynamic measurement [16]. In this study, an optical fiber Fabry Perot interferometer (FFPI) is proposed and demonstrated for dynamic measurements in a mechanical vibrating target. A polishing metal with a low reflectance value adhered to a mechanical vibrator was excited via a function generator at various excitation frequencies. Output interference fringes were generated by modulating the reference and sensing signal at the output arm. A fringe counting technique was used for interpreting the displacement information on the dedicated computer. The fiber interferometer is capable of displacement measurements between 1.28 μm - 96.01 μm. A commercial displacement sensor was employed as a reference sensor for investigating the measurement errors from the fiber sensor. Nagaike et al. [17] made a sub-micron position sensor with using fiber optic interferometer. It is mentioned that the wide applications of piezoelectric transducers in position server systems make the measurement and control of sub-micron displacement more and more important these days. In their study, a novel system based on the fiber optic interferometer and digital signal processing techniques is proposed. The size of the sensor is reduced by the fiber optics and the precision of measurement is assured by the digital analysis of the linear interference fringes. In the experiments of evaluating two types of piezoelectric transducers, a sensitivity of 5 nm has been realized [17]. Djinovic et al. [18] used fiber optic white light interferometry to measure wear rate and vibrations. The proposed contactless technique is capable of measuring the wear rate and vibrations of the pin in a standard pin-on-disc tribometer remotely and simultaneously. All data are obtained by an interferometric reading of the sensing fibers displacement using a passive demodulation technique employing a 3x3 fiber optic coupler and mechanical scanner. The results obtained in a pin position have resolution better than 100 nm in the range of 400 μm as well as minimal detectable amplitude of the pin vibration of about 50 pm/$\sqrt{Hz}$. Iannuzzi et

al. [19] used an atomic force microscope (AFM) based on fiber-top design. The results demonstrate that the performance of fiber-top AFMs in contact mode is comparable to those of similar commercially available instruments. The device thus represents an interesting alternative to existing AFMs, particularly for applications outside specialized research laboratories, where a compact, user friendly, and versatile tool might often be preferred [19]. Hlubina et al. [20] presented a white light sprectral interferometric technique for measuring the thickness of SiO_2 thin film on a silicon wafer. The technique utilizes a slightly dispersive Michelson-interferometer with a cube beam splitter and a fibre-optic spectrometer to record channeled spectra in two configurations.

CHAPTER 3

DISTANCE MEASUREMENT USING INTERFEROMETRY

When light beams originating from the same source are superimposed on an observation screen by suitable optical elements, the intensity on the overlapped region can be changed from point to point. The maximum intensity can exceed the sum of the intensities of the two beams; the minimum intensity may be zero. This phenomenon is known as interference, which is one of the most important results of the wave nature of light. Today, interferometry is used for important measurements in different areas of science.

3.1 Theory

The interference phenomenon is explained in Figure 3.1. Two wave planes are projected onto a screen. The observed intensity is not simply the sum of the intensities of the two waves in the region where two waves meet. Instead, interference fringes are observed. However, interference phenomenon is not common in daily life so interference occurs under in specific circumstances.

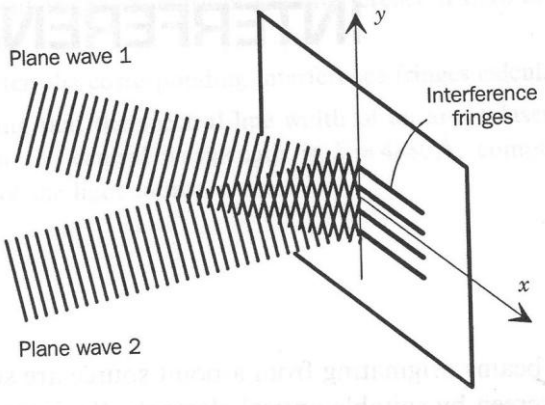

Figure 3.1. Interference of two plane waves[21]

In order to realize the condition for interference, the superposition principle should be understood. The superposition principle is explained in Appendix A [22]. The resultant intensity detected by the photo-detector is given in Eq. 3.1.

$$I = I_1 + I_2 + 2\sqrt{I_1 I_2}\cos(\delta) \tag{3.1}$$

In order to have a stable intensity distribution, the phase difference at any given point must be the same. This means that the difference in initial phase shift between the two light waves $(\varepsilon_1 - \varepsilon_2)$ should be constant. At various points in space, the resultant intensity can be greater than, less than, or equal to $I_1 + I_2$, depending on the value of δ. It is apparent that maximum resultant intensity occurs when $\cos(\delta) = 1$, such that

$$I_{\max} = I_1 + I_2 + 2\sqrt{I_1 I_2} \tag{3.2}$$

when

$$\delta = 0, \pm 2\pi, \pm 4\pi, ... \tag{3.3}$$

In this case, the phase difference between the two waves is an integer multiple of 2π, and the two light waves are said to oscillate in phase. The minimum resultant intensity occurs when $\cos(\delta) = -1$, such that

$$I_{\min} = I_1 + I_2 - 2\sqrt{I_1 I_2} \tag{3.4}$$

when

$$\delta = \pm\pi, \pm 3\pi, \pm 5\pi, ... \tag{3.5}$$

When the resultant intensity is maximum, the resulting interference is called *constructive interference*. When the resultant intensity is minimum, the resulting interference is called *destructive interference.*

The assumptions in the derivation of Eq. 3.1 are:

1. The two waves which interfere with each other should have the same polarization
2. The two waves should oscillate at the same frequency to cancel the frequency dependent term in the argument of cosine function in Eq. A.1.
3. The phase difference represented in Eq. 3.1 must be constant at any given point in the superimposed region. Otherwise, no stable fringes can be observed.

Light waves meeting these conditions are called coherent waves. They are usually derived from the same light source and then split by some optical equipment such as mirrors, beam splitters, or slits. The methods of beam splitting are generally categorized into two classes: wave front splitting and amplitude splitting. Interferometers can be classified in terms of these classes.

3.2 Visibility of Fringes

In practice, the sharpness (i.e, contrast) of the fringes decreases as the phase difference between the two beams increases. When the phase difference exceeds some limit, the fringes totally vanish. This is the result of the coherence of the light sources. The contrast of the fringes, or visibility, can be defined as

$$V = \frac{I_{\max} - I_{\min}}{I_{\max} + I_{\min}} \tag{3.6}$$

The value of the visibility varies between 0 and 1. When the fringes are at the highest possible intensity value in the brightest areas and zero intensity in the darkest areas, the visibility is equal to 1, as shown in Figure 3.2.a. As the phase difference increases, the coherence between the light waves decreases and the visibility is reduced, as shown in Figure 3.2.b. Finally, as the coherence between the two waves vanishes, $I_{\max}$ and $I_{\min}$ converge and visibility is equal to 0. No fringes can be observed, as shown in Figure 3.2.c.

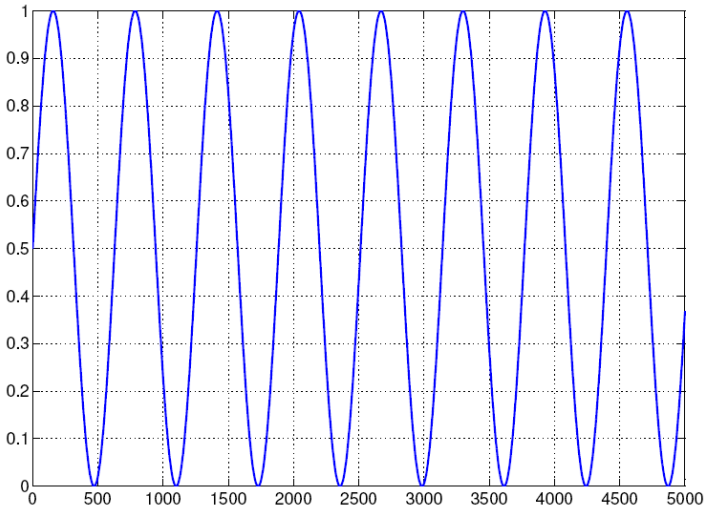

(a)

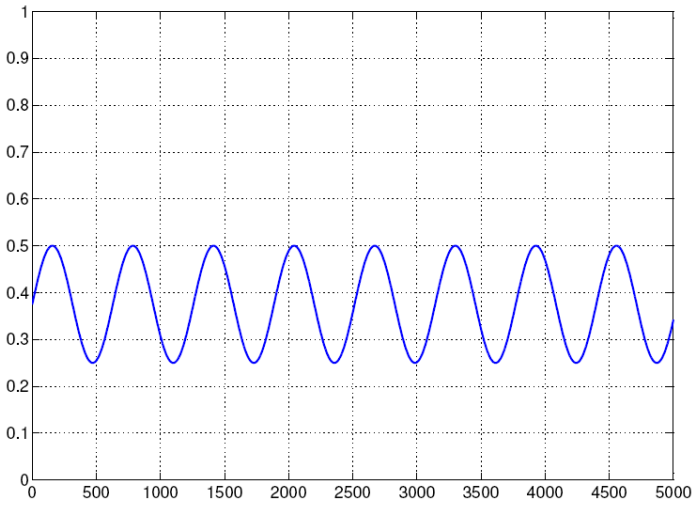

(b)

Figure 3.2 Fringes with different visibility values, (a) V=1, (b) 0<V<1, (c) V=0

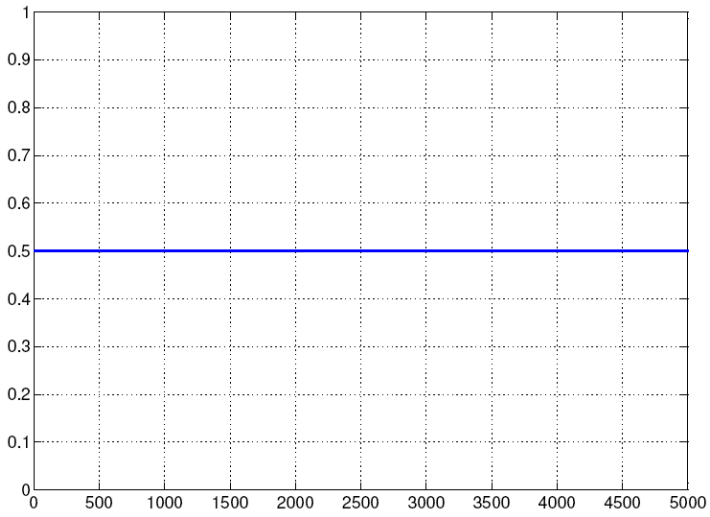

(c)

Figure 3.2. Fringes with different visibility values, (a) V=1, (b) 0<V<1, (c) V=0 (continued)

In practice, the spectrum of a light source always has a finite bandwidth. If a light source with finite spectral bandwidth is used, the visibility is smaller than 1 even though the two light waves have very small phase difference. The visibility is a measure of the temporal coherence of the light source, which can be determined by the spectral bandwidth of the source. The maximum optical path difference between two beams that leads to visible fringes is called coherence length. For a light source with spectral bandwidth of $\Delta\lambda$, the coherence length is given by

$$\Delta r = \frac{\lambda^2}{\Delta\lambda} \tag{3.7}$$

3.3 Michelson Interferometer

The Michelson interferometer, developed by Albert Michelson in the 1880s, played an important role in the development of modern physics, particularly in the theory of relativity. It is a highly accurate measuring instrument and is widely used in

many scientific and engineering applications. The arrangement of Michelson interferometer is shown schematically in Figure 3.3.

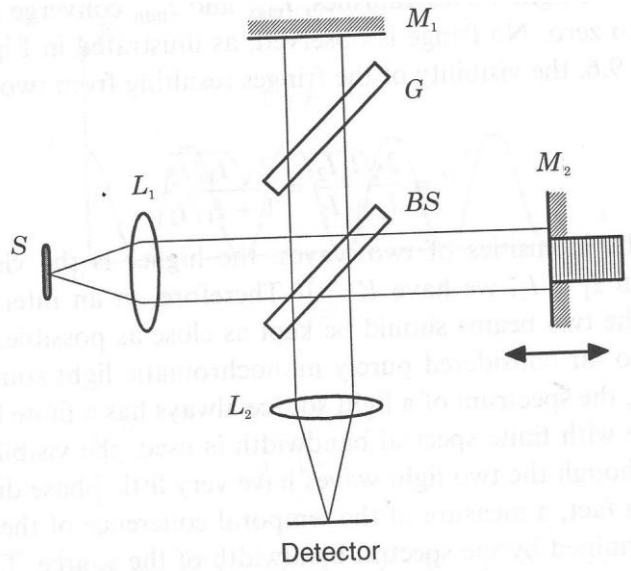

Figure 3.3 Michelson Interferometer. *S* light source; *BS* beam splitter; M_1 Mirror; M_2 moving mirror; *G* compensating glass; *L* lense.[21]

As an example of amplitude-splitting interferometers, the two interfering beams are obtained using a half-reflective and half-transmissive mirror, the so-called *beam splitter*. These two beams are then sent in different directions against two highly polished plane mirrors, where they are reflected and combined again by the beam splitter to form interference fringes. A plate made of the same material as the substrate of the beam splitter may be set in one of the two arms as a compensation plate. This ensures that optical path in each arm is rendered equivalent by passing through the same thickness of the same material. Mirror M_2 is equipped with a micrometer screw so that it may be moved along the optical axis, thereby adjusting the optical path difference between the two arms.

If a point source is placed at the front focal point of lenses L_1, the input light to the interferometer is a collimated beam. The output beam is then focus by lens L_2 onto the detector. Although no fringes are observable, the detected intensity does change

while the mirror M_2 moves. It changes from $I_{\max}$ to $I_{\min}$, and then back to $I_{\max}$ again, when M_2 moves at a distance $\frac{\lambda}{2}$. If the mirror moves a distance of l, the number of cycles in the intensity change is,

$$N = \frac{2*l}{\lambda} \tag{3.8}$$

3.4 Mach-Zehnder Interferometer

The Mach-Zehnder interferometer is another amplitude-splitting interferometer. As shown in Figure 3.4, it consists of two beam splitters and two totally reflecting mirrors. The two waves within the apparatus travel along different paths. If the incoming light is collimated beam, straight fringes with uniform fringe spacing can be obtained by slightly tilting one beam splitter.

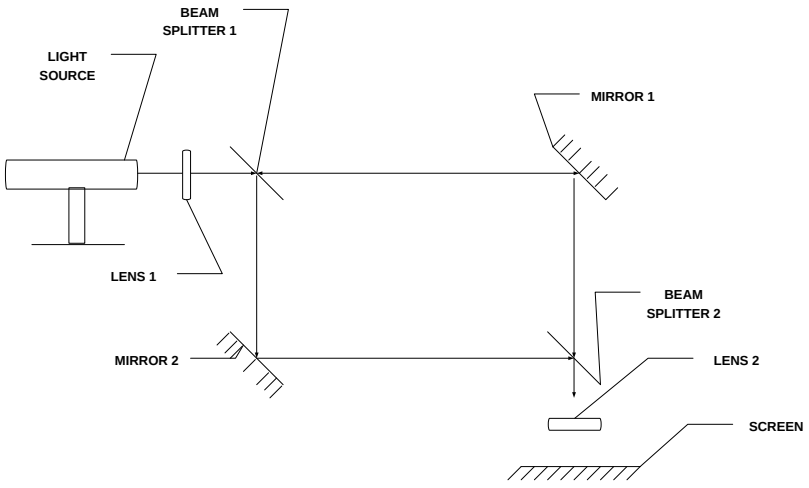

Figure 3.4 The Mach-Zehnder Interferometer. *S* light source; BS_1, BS_2 beam splitter; $L_1, L_2,$ lenses; $M_1, M_2,$ mirrors.

The beams are produced at the light source and then they are collimated by the first lens to the first beam splitter. The first beam splitter reflects half of the coming light

and transmits the remaining part of the coming light. Reflected part of the light is directed to the first mirror and then directed to the second beam splitter. The beam splitter reflects half of the light and transmits the remaining part of it. Transmitted light at the first beam splitter is directed to the test chamber and then second mirror. The mirror reflects the light to the second beam splitter where two light beams are interfering with each other. After the light beams interfere, they are directed to the second lens and this lens is focused the interfering beams to the screen. Since the two paths are separated, the insertion of some samples into one of the arms produces a path difference, which generates interference fringes in the observing plane.

3.5 Fiber Optics

Before introducing the fiber optic interferometer, fiber optic components are introduced to explain the construction, types and applications of the fiber optic components.

3.5.1 Fiber Optic Cables

The structure of a typical optical fiber is illustrated schematically in Figure 3.5. The center of the fiber is a cylindrical *core* with a refractive index η_1, surrounded by a layer of material, called the *cladding*, with a lower refractive index η_2. The light waves are restricted by the cladding within the core and propagate along the fiber. The outer jacket layers not only protect the fiber from moisture and abrasion, but also provide the strength that is required practically.

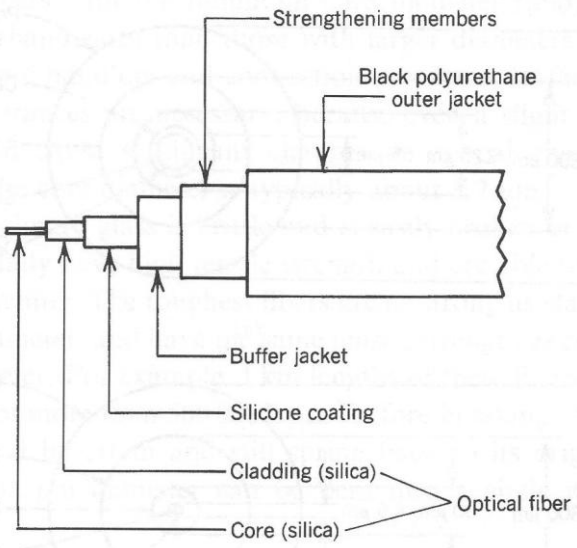

Figure 3.5. Cross section of an optical fiber [21]

Fiber optics (optical fibers) are long, thin strands of very pure glass about the diameter of a human hair. They are arranged in bundles called optical cables and used to transmit light signals over long distances. Hundredths or thousands of these optical fibers are arranged in bundles in optical cables. There are two types of optical fibers:

1. Single- mode fibers
2. Multi-mode fibers

Single mode optical fibers have small cores (about 9 μm) and transmit infrared laser light (wavelength range of 1300-1550 nanometers). Multi-mode fibers have larger cores (about 62.5 μm) and transmit infrared light (wavelength range 850-1300 nanometers) from light emitting diodes (LED). Some optical fibers can be made from plastic. These fibers have a large core (about 1 mm diameter) and transmit visible red light (wavelength of 650 nm) from LEDs.

The light in a fiber optic cable travels through the core by constantly bouncing from the cladding, a principle called total internal reflection. Since the cladding does not

absorb any light from the core, the light wave can travel great distances. This process is shown in Figure 3.6.

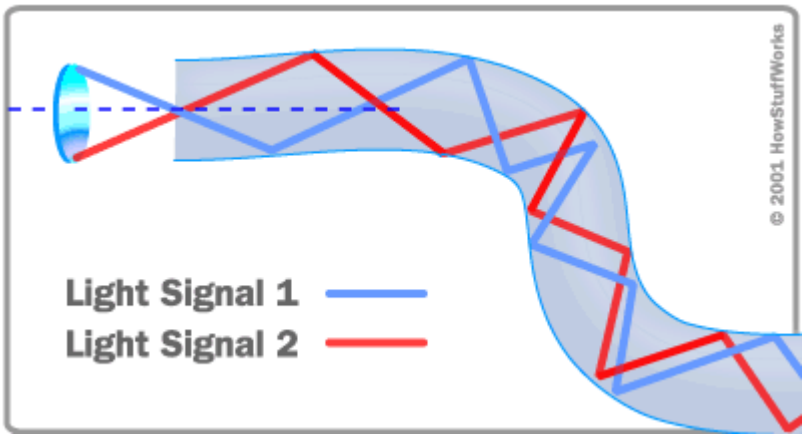

Figure 3.6. Total internal reflection in an optical fiber [23]

However, some of the light signal degrades in the fiber, mostly due to the impurities in the glass. The extent that the signal degrades depends on the purity of the glass and the wavelength of the transmitted light.

There are a lot of advantages of using fiber optic cables:

1. Cost - Several kilometers of optical cable can be made cheaper than equivalent lengths of copper wire.
2. Size – Optical fibers can be drawn to smaller diameters than copper wire.
3. Signal carrying capacity – Since optical fibers are thinner than copper wires, more fibers can be bundled into a given diameter cable than copper wires.
4. Signal degradation – The loss of signal in optical fiber is less than in copper wire.
5. Interference – Unlike electrical signals in copper wires, light signals from one fiber do not interfere with those of other fibers in the same cable.
6. Safety – Since no electricity is passed through optical fibers, there is no fire hazard.
7. Lightweight – An optical cable weighs less than the copper wire.

8. Flexibility – The fiber optic cables are very flexible and can transmit the information in different shapes.

Due to the several advantages of fiber optic cables, they are used in medical imaging (endoscope, bronchoscopes and laparoscopes), mechanical imaging (inspecting mechanical welds in pipes and engines), vibration measurements and distance measurements.

3.5.2 Fiber Optic Interferometer

A fiber optic interferometer is a typical multiple beam interferometer. It consists of a laser source, a single mode fiber optic cable, a beam splitter or a coupler, a target and a photo detector. A classical configuration of a fiber optic interferometer is shown in Figure 3.7.

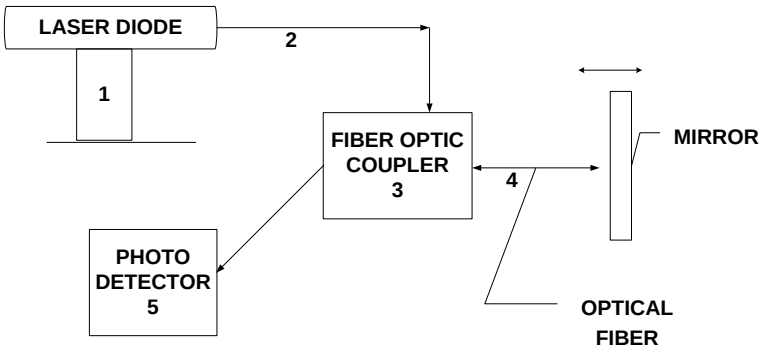

Figure 3.7. Classical configuration of a fiber optic interferometer

In Figure 3.7, the infrared laser beam emitted from the laser source (1) is directed into the fiber cable (2) and propagates through the coupler (3) to fiber (4). Laser radiation reflected from the end face of the fiber (4) interferes with the laser beam reflected from the mirror. Then, interfering beams are directed to the photo detector. The detected intensity is given by [23],

$$I = I_0 \times (R_1 + (1-R_1)^2 \times R + 2 \times (1-R_1) \times \sqrt{R \times R_1} \times \frac{\sin(\varepsilon)}{\varepsilon} \times \cos(4 \times \pi \times \frac{x_0}{\lambda})) \quad (3.9)$$

where $I_1 = I_0 * R_1$ is the intensity of the light reflected from the end face surface of the fiber and $I_2 = (1-R_1)^2 * R * I_0$ is the intensity of the light reflected from an external mirror and returned back into the fiber, where I_0 is the intensity of the laser diode radiation couple into the fiber, R_1 is the reflectivity of the end face of the fiber, ε is the ratio of gap and the coherence length of the laser and R is the reflectivity of an external mirror. The detected density versus the gap between the fiber end and the target is shown in Figure 3.8.

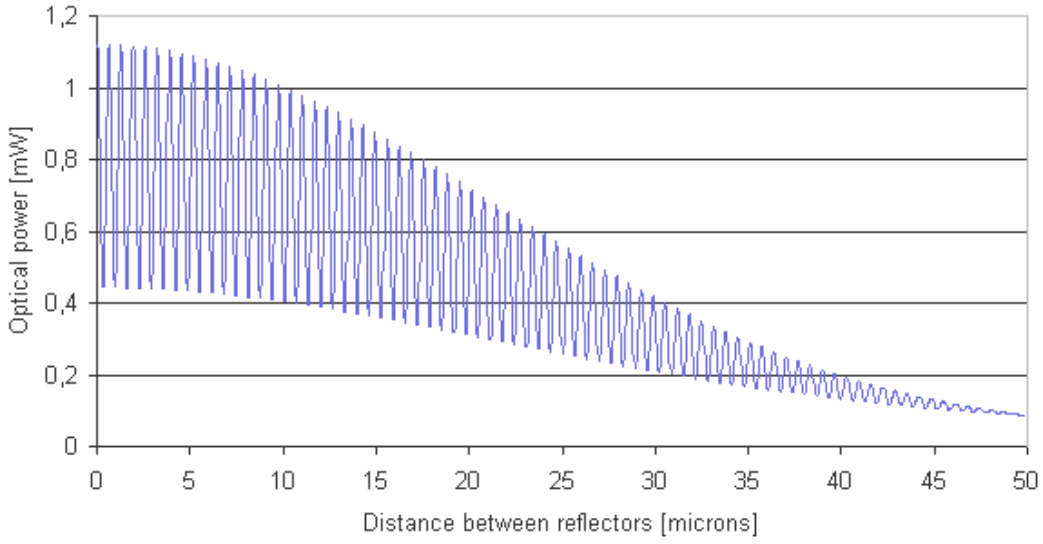

Figure 3.8. Variation of optical power of interferometer with distance [24]

As it can be seen from Figure 3.8, the direction of the motion can be easily determined by using fiber optic interferometry, whereas direction of the motion can not be determined easily in other interferometers. In fiber optic interferometer, the direction of the motion can be determined by only looking at the trend of the local maximum intensities. In Figure 3.8, local maximum intensities have a decreasing trend which means that the gap between the fiber end and the reflective surface increases.

CHAPTER 4

EXPERIMENTAL SETUP AND EXPERIMENTAL PROCEDURE

In this chapter, the experimental setup and the experimental procedure are explained. The experimental setup contains three main components, namely the optical system, the mechanical stage and data acquisition system. The experimental procedure also includes a step by step set of instructions to perform experiments.

4.1 Experimental Setup

The experimental setup contains three main components which are the optical bench, mechanical stage and data acquisition system. Optical bench contains the optical equipments such as laser, fiber optic isolator, fiber optic connectors, fiber optic circulators, fiber optic beam splitter, photo- detectors, fiber optic cables, and optical table. Mechanical stage contains numerous mechanical parts such as step motor, step motor driver, PIC card, power source, coupling, micrometers, magnetic bases, lateral motion carriage, first plate, guide rails, second plate, gold coated mirror, shaft, third plate and encoder probe holder. Data acquisition system contains BNC connectors, data acquisition platform, data acquisition cable, data acquisition card, data acquisition software, laptop computer and desktop computer.

4.1.1 Optical System

The optical system consists of different optical components to be used for building up a modified fiber optic interferometer.

4.1.1.1 Laser

The laser used in this study has a wavelength of 1550 nanometers. It is a Oz Optics HIFOSS distributed feedback (DFB) laser which has a flat connector in one end and angled polished connector in other end (FC/APC) receptacle. This receptacle enables it to reduce transmission loss occurring during the connection of the laser and a fiber optic cable. The photo and the specifications of the laser are shown in Figure 4.1 and in the Appendix B.1, respectively.

Figure 4.1 A view of laser source

4.1.1.2 Isolator

The isolator used in this study is an Oz Optics polarization insensitive isolator whose wavelength is 1550 nanometers. In order to reduce the transmission loss, it has angle FC/PC connectors on both ends. It is used to reduce the rate of back reflection of the laser beams from other optical components to the laser. The photo and the specifications of the isolator are shown in Figure 4.2 and in the Appendix B.2, respectively.

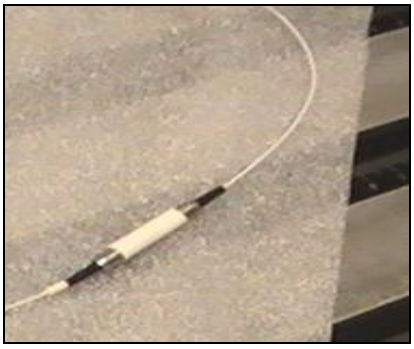

Figure 4.2 A view of isolator

4.1.1.3 Beam Splitter

The beam splitter used in this study is a Oz Optics single mode fiber pigtailed beam splitter. It has a one input and four output ports. It divides the laser beam's optical intensity into four equal intensity parts. It has angle FC/APC connectors on both ends. The photo and the specifications of the beam splitter are shown in Figure 4.3 and in the Appendix B.3, respectively.

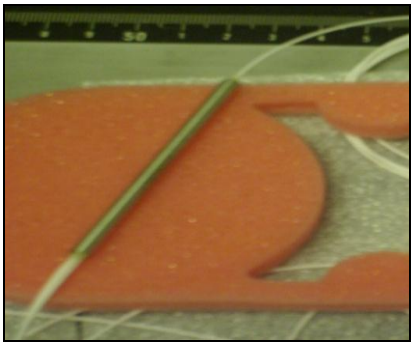

Figure 4.3 A view of beam splitter

4.1.1.4 Connectors

The connectors used in this study are Oz Optics flanged sleeve through connectors for polarization maintaining. They have FC/PC connectors on both ends. They are used to connect the different optical components in which the laser beams are passing. The photo of the connector is shown in Figure 4.4.

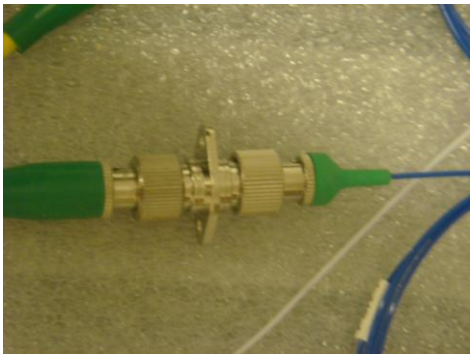

Figure 4.4. A view of connector

4.1.1.5 Circulators

The circulators used in this study are Oz Optics fiber optic miniature circulators. They are used first for directing the laser beams coming from the laser source to the mechanical stage. Then, they are used for directing the laser beams coming from the mechanical stage to the photo detectors without any loss. They have one input and two output ports named as T, R and 1, respectively. When the laser beams come to the circulator port T is opened and directs the laser beams to the mechanical stage to port 1. When the laser beams return back from the mechanical stage to the circulator port in port 1, port R is opened and the laser beams are directed through the photo detectors. They have angled FC/APC connectors on all ports. The photograph and the specifications of the connector are shown in Figure 4.5 and in the Appendix B.4, respectively.

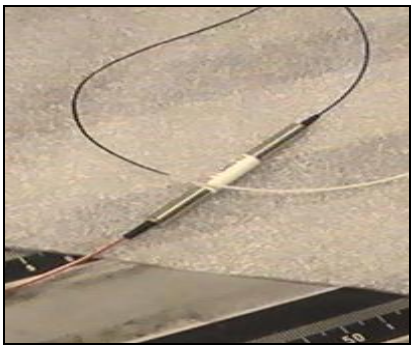

Figure 4.5 A view of circulator

4.1.1.6 Photo – Detector

The photo-detectors used in this study are Thorlabs switchable gain detectors. The wavelength range of these photo–detectors is 800-1800 nanometers. Since they have switchable gains, there is no need to use an amplifier circuit to amplify the optical outputs. They are used to convert the optical outputs coming from the circulator into the electrical signals in the range of -10 to 10 volts. They also have FC/APC adapter to be compatible with fiber optic cables. In order to transmit the electrical signals from the photo-detector to the data acquisition platform, Bayonet Neill-Concelman (BNC) connectors are used. The photo and the specifications of the circulator are shown in Figure 4.6 and in the Appendix B.5, respectively.

Figure 4.6 A view of photo-detector

4.1.1.8 Fiber Optic Cable

The fiber optic cables used in this study are Oz Optics special type single mode fiber optic cables. In order to install these fiber optic cables on to the third plate in the mechanical stage, one end of these fiber optic cables has angled FC/PC connectors, other end has flat polished ferrule (white part of the fiber optic cables). This end of the fiber optic cables is called “fiber optic probe” in this study. They operate in the wavelength range of 1300-1550 nanometers. The photograph and the specifications of the fiber optic cable are shown in Figure 4.7 and in the Appendix B.6, respectively.

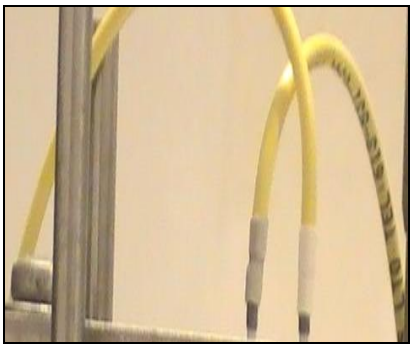

Figure 4.7 A view of fiber optic cables

4.1.1.8 Optical Table

All the optical bench parts and some of the mechanical stage parts are placed on to the optical table. The optical table dimensions are $70 \times 120 \times 20$ centimeters. It has four pads on its four corners in order to reduce the external vibration effects. It is placed on a rectangular base whose dimensions are $75 \times 130 \times 85$ centimeters. The photograph of the optical table and its base is shown in Figure 4.8.

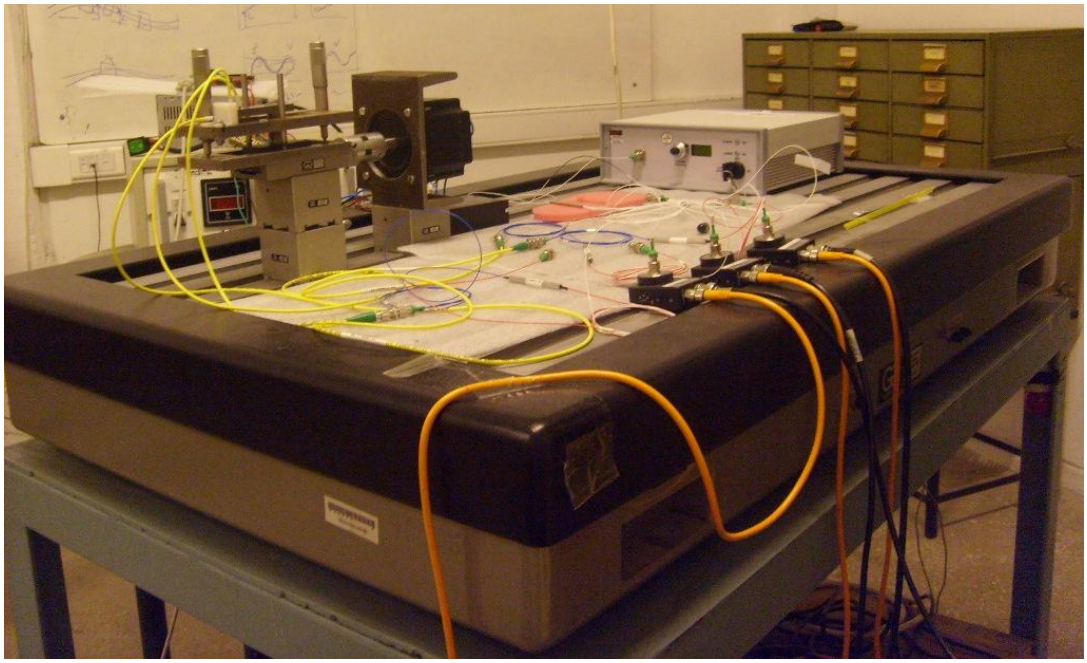

Figure 4.8 A view of optical table and its holding

4.1.2 Mechanical Stage

The mechanical stage consists of different mechanical parts to simulate piston cylinder motion in a hermetically sealed compressor in the Cartesian coordinate system. The parts of the mechanical system are shown in Figure 4.9.

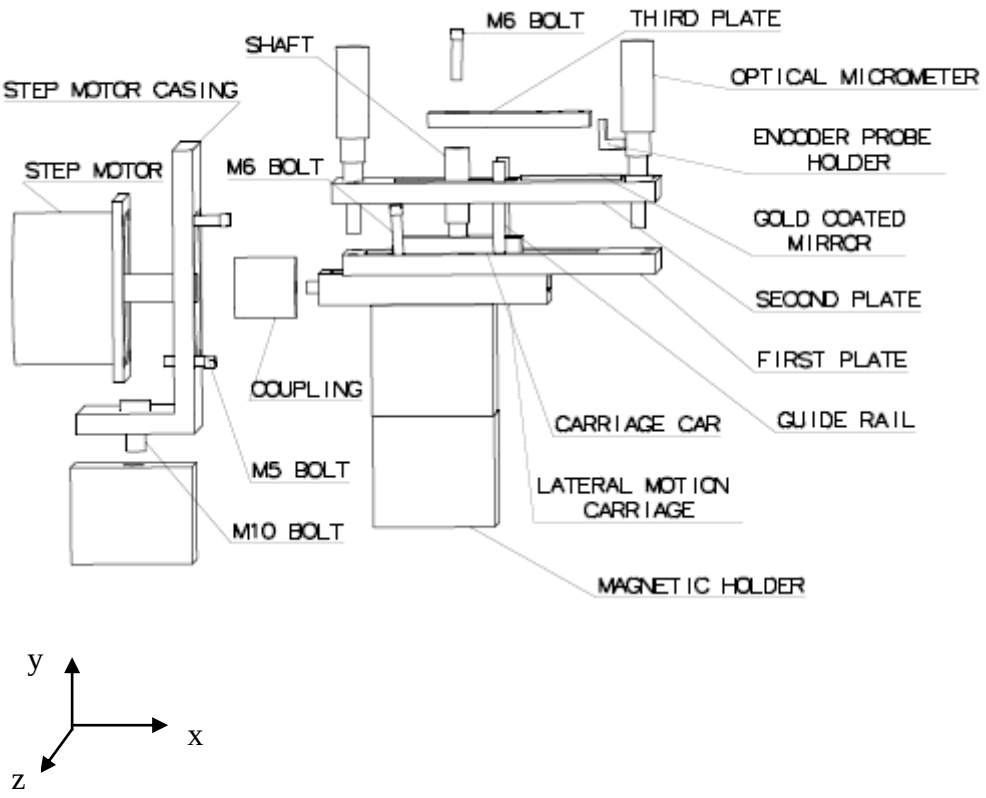

Figure 4.9 Mechanical system components

The step motor is connected to the step motor casing with four M5 bolts at its four corners. The step motor casing is fixed to the magnetic base with an M10 bolt at its center. A coupling is used to transmit the rotary motion of the step motor to the lateral motion carriage which is fixed to the optical table by two magnetic bases. The first plate is fixed on the lateral motion carriage with four M5 bolts and two guide rails are fixed to the first plate. Two micrometers are clamped to the second plate and they are free to move in the vertical "*y*" direction. There are clearance holes on to the second plate to allow guide rails to move in the vertical direction. The gold coated mirror is placed on to the part which has a 2-mm height difference

with the second plate. The shaft is used to transmit the lateral motion of the carriage to the third plate in the horizontal "*x*" direction. The shaft is fixed to the lateral motion carriage car and the third plate is fixed to the shaft with an M5 bolt and nut. There are three drilled holes on the third plate to place the three fiber optic probes. Furthermore, there is an encoder probe holder on to the second plate to hold the encoder fiber optic probe and there is a small gold coated mirror at the back right hand side of the third plate. The fiber optic encoder probe is used to detect the horizontal displacement of the third plate using the small gold coated mirror.

4.1.2.1 Step Motor and Step Motor Casing

Since the step motor generates a continuous rotational motion, the lateral motion is generated via a step motor in this study. In order to reduce the vibration motion of the step motor, a step motor casing is manufactured and the step motor is connected to this casing with four (M5) bolts and nuts. Furthermore, the step motor and step motor casing are fixed to the optical table with a magnetic base. The photograph, the specifications of the step motor, and technical drawings of the step motor and step motor casing are shown in Figure 4.10, in the Appendix B.7 and in the Appendix C.1, respectively.

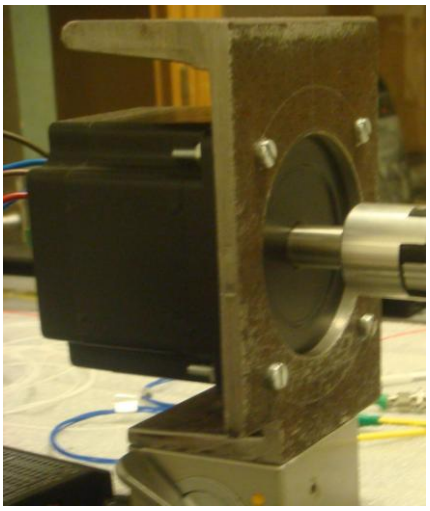

Figure 4.10 A view of step motor and step motor casing

4.1.2.2 Step Motor Driver, PIC Card and Power Source

In order to control the driver, PIC card, step motor driver and a power source are used. Furthermore, an interface code is written to send signals from the computer to the PIC card to control the direction of the motion and number of the revolutions that step motor should perform. The photographs and the specifications of step motor driver, PIC card and power source are shown in Figure 4.11 and in the Appendix B.8, respectively.

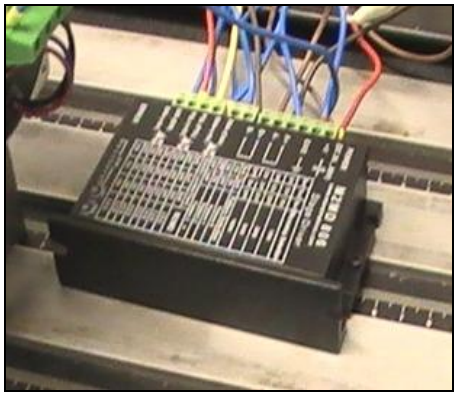

(a)

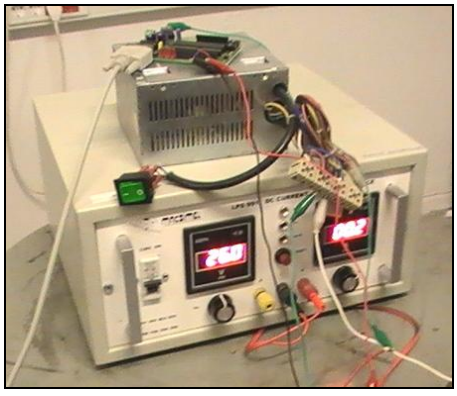

(b)

Figure 4.11 (a) Step motor driver, (b) Power source and PIC card, (c) Interface

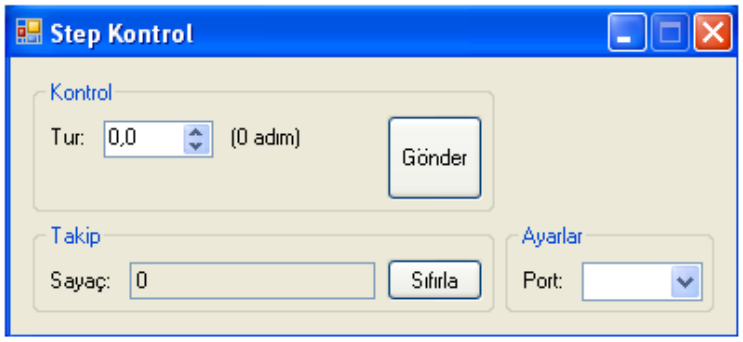

(c)

Figure 4.11 (a) Step motor driver, (b) Power source and PIC card, (c) Interface (continued)

The interface of the step motor control is shown in Figure 4.11.c. The number of the revolutions can be adjusted by using *"tur"* button located at the upper left hand side on this interface. The positive revolution values indicate that the step motor is turned in the clockwise direction, and negative revolution values indicate that the step motor is turned in the counter clockwise direction. There is another *"sayaç"* button, used for counting operation during the experiments located on the lower left hand side of the interface. This button is used to remind the distance travelled during the experiments by the third plate to the user. Therefore, the start and finish point's locations of the third plate can be kept constant with this control. In order to achieve the communication between the computer and PIC card, the *"port"* button is used to select the suitable port of the computer.

4.1.2.3 Coupling

Coupling is used to transmit the rotary motion of the step motor to the lateral motion carriage. A rubber material is placed between the two mating parts of coupling to reduce the transmission level of vibration of the step motor. Furthermore, one hole is drilled on the step motor side and two holes are drilled on the lateral motion carriage side of the coupling to fix the coupling on to the step

motor and lateral motion carriage, respectively. The photo and technical drawing of the coupling are shown in Figure 4.12 and in the Appendix C.2, respectively.

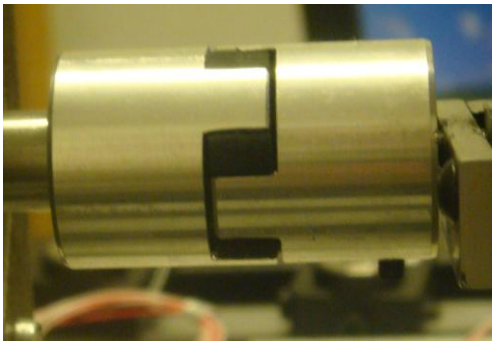

Figure 4.12 A view of coupling

4.1.2.4 Magnetic Bases

In this experimental study, three magnetic bases are used. Two of them are used to fix the lateral motion carriage and the other mechanical stage parts and one of them is used to fix the step motor and its casing on to the optical table. Moreover, different types of external effects occurring inside the lab environment can be eliminated by the aid of magnetic bases. The photograph and the technical drawing of the magnetic base are shown in Figure 4.13 and in the Appendix C.3, respectively.

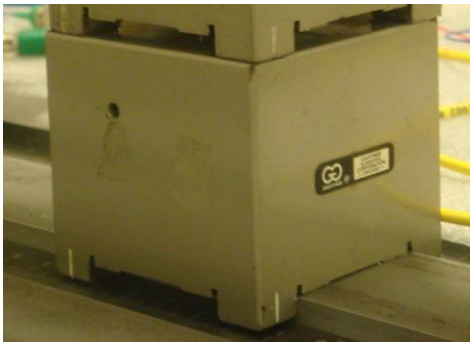

Figure 4.13 A view of magnetic base

4.1.2.5 Lateral Motion Carriage

Optical lateral motion carriage is used to generate lateral motion in the Cartesian model of piston cylinder motion in this study. It is fixed to the optical table by two magnetic bases. In this carriage, there is a moving car connected to the carriage shaft and it is connected to the coupling. Therefore, rotational motion of the step motor is transmitted to the carriage shaft by the coupling and this rotational motion is converted to lateral motion by the carriage shaft and carriage car can be moved in the forward and backward directions. The photograph and technical drawing of the lateral motion carriage are shown in Figure 4.14 and in the Appendix C.4, respectively.

Figure 4.14 A view of lateral motion carriage

4.1.2.6 First Plate

First plate is fixed to the lateral motion carriage with four M6 bolts. It has a rectangular groove for allowing the carriage car motion in the lateral direction and six clearance holes for guide rails. In this experimental setup, only two guide rails are used. This plate and other plates are designed for performing the vertical motion in the Cartesian model of the piston cylinder. The photograph and the technical drawing of the first plate are shown in Figure 4.15 and in the Appendix C.5, respectively.

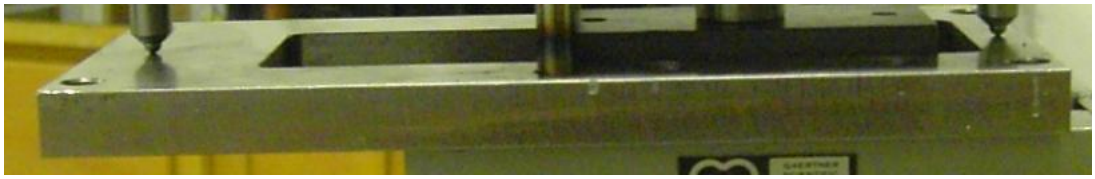

Figure 4.15 A view of first plate

4.1.2.7 Guide Rails

Guide rails, fixed on to the first plate, are used to guide the second plate in the vertical direction with the motion of two micrometers. Although there are six guide rail holes on to the first and second plate, only two of them are used. In order to guide the second plate in the vertical motion, the clearance in the drilled holes on the second plate must be accurately estimated and manufactured to avoid any tightness or looseness during the vertical motion. The photo and the technical drawing of the guide rails are shown in Figure 4.16 and in the Appendix C.6, respectively.

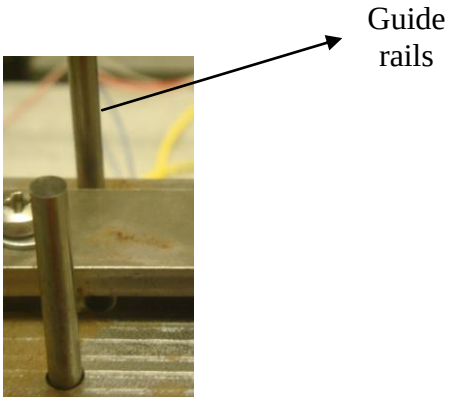

Figure 4.16 A view of guide rails

4.1.2.8 Second Plate

Second plate is moved in the vertical direction with the movement of two micrometers and guide rails in this study. It has six drilled clear guide rail holes and two drilled micrometer holes. Furthermore, it has a rectangular shape groove for the

lateral motion of carriage car and a rectangular protrusion, which is two millimeters higher than the second plate, used for placing the gold coated mirror. This rectangular part has a higher level in order to avoid spreading the lubricants on the second plate in the experiments with lubricants. The photograph and the technical drawing of the second plate are shown in Figure 4.17 and in the Appendix C.7, respectively.

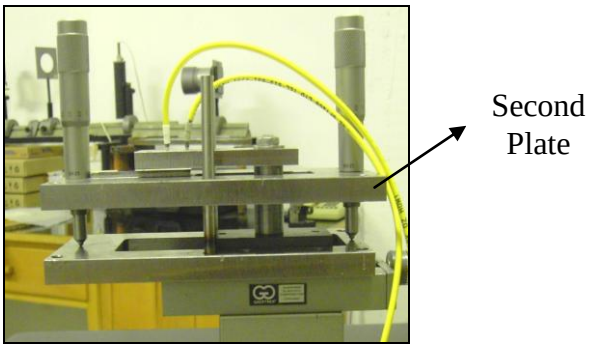

Figure 4.17 A view of second plate

4.1.2.9 Micrometers

Two Newport SM-25 micrometers are used to generate vertical motion in this study. The sensitivity of the micrometers is one μm. However, since the length of the gold coated mirror is less than the distance between the two micrometers, the sensitivity of the vertical distances measured in the experiments is less than one μm and this sensitivity can be changed according to the lateral motion range generated by the step motor in the experiments. The photo and the technical drawing of the micrometers are shown in Figure 4.18 and in the Appendix C.8, respectively.

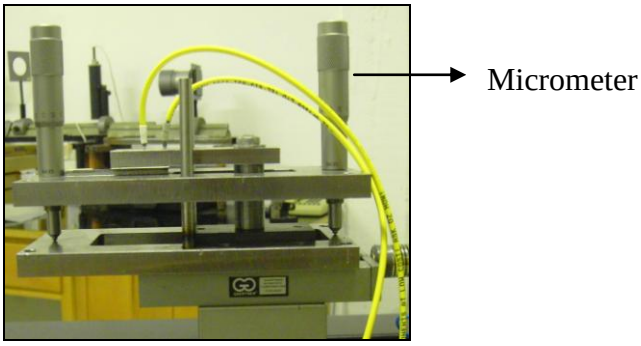

Figure 4.18 A view of micrometers

4.1.2.10 Gold Coated Mirror

Gold coated mirror is used to reflect the laser beams leaving the fiber optic cables. Since the wavelength of the laser is 1550 nm and reflectivity of gold at this wavelength is approximately 0.98, this type of mirror is chosen in this study. Ti/Au sputter is used to manufacture the gold coated mirror comprises of 50 nanometers titanium and 500 nanometers gold in thickness. This mirror is manufactured at the Department of Electrical and Electronics Engineering. This mirror is placed on to the rectangular part on to the second plate. The dimensions are $50mm \times 10mm \times 550nm$. The photograph of the gold coated mirror is shown in Figure 4.19.

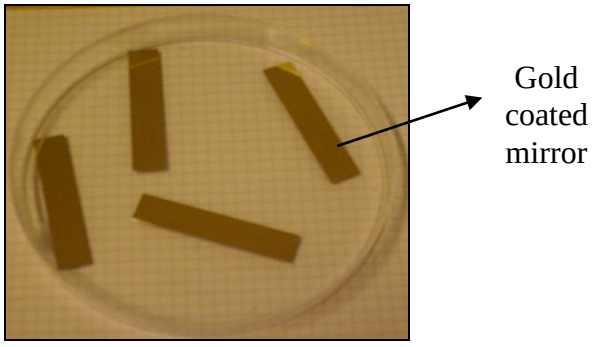

Figure 4.19 A view of gold coated mirror

4.1.2.11 Shaft

A shaft is used to transmit the lateral motion of the carriage car to the third plate on which fiber optic cables are placed. Therefore, the shaft is fixed to the carriage car and the third plate is fixed on to the shaft. The length of the shaft is designed according to the two parameters. First one is the vertical distance between the first and the second plate and the second one is the vertical distance between third plate and the gold coated mirror. In the design phase of this study, the vertical distance between the first and second plate is calculated when the two micrometers are set to half of their moving range. Moreover, the vertical distance between third plate and the gold coated mirror is taken as one millimeter. The photograph and the technical drawing of the shaft are shown in Figure 4.20 and in the Appendix C.8, respectively.

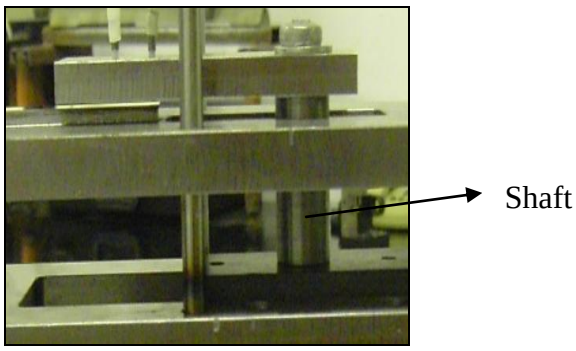

Figure 4.20 A view of shaft

4.1.2.12 Third Plate

Third plate is used to perform the lateral motion and to hold the fiber optic cables. There are three drilled clear holes for fiber optic cables. These holes have small tolerances to have a tight fiber optic cables installation. The third plate and the shaft are connected to each other by metric 10 (M10) bolt and nut. There is a small gold coated mirror attached to the back right hand side of the third plate. The photograph and the technical drawing of the third plate are shown in Figure 4.21 and in the Appendix C.9, respectively.

Figure 4.21 A view of third plate

4.1.2.12 Encoder Probe Holder

Encoder probe holder is placed on to the second plate in one of the drilled guide rail holes with metric 6 (M6) bolt and nut. There is a fiber optic cable fixed in to the encoder probe holder and this fiber optic cable is used as an encoder probe in this study. This probe detects the horizontal gap between the fiber optic cable end and the small gold coated mirror glued to the back right hand side of the third plate. In other words, this probe detects the lateral motion generated by the step motor in time domain. The photograph and the technical drawing of the encoder probe holder are shown in Figure 4.22 and in the Appendix C.10, respectively.

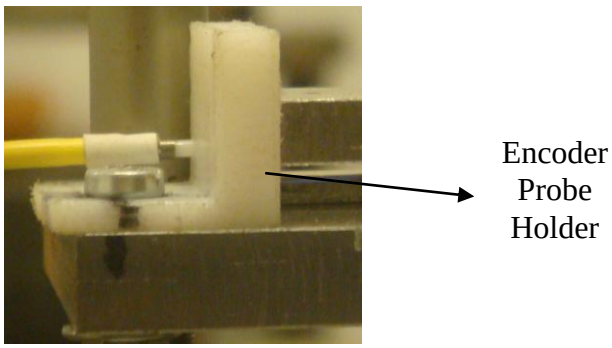

Figure 4.22 A view of encoder probe holder

4.1.3 Data Acquisition System

Data acquisition system consists of BNC connectors, data acquisition platform, data acquisition cable, data acquisition card, data acquisition software, laptop computer and desktop computer.

4.1.3.1 BNC Connectors

BNC connectors are used to transmit the electrical signals from the photo-detectors to the data acquisition platform. Since the output of the photo-detectors and the data acquisition platform are BNC type, BNC connectors are used in this study. The length of the cables is two meters. Since the BNC cables are shielded cables, the noise level is smaller than the bare cables. The photograph of the BNC connectors is shown in Figure 4.23.

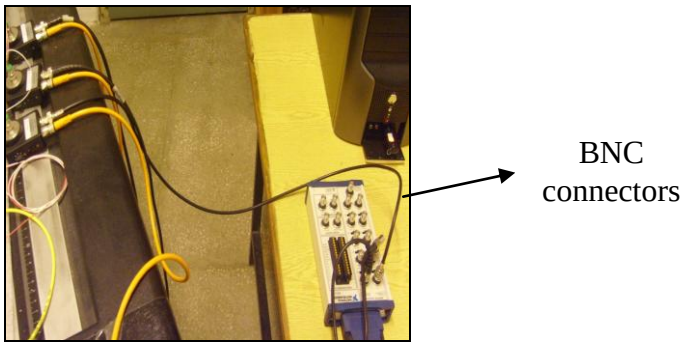

Figure 4.23 A view of BNC connectors

4.1.3.2 Data Acquisition Platform

National Instruments BNC 2110 data acquisition platform is used to transfer the data coming from the photo-detectors to the data acquisition cable. Since this is a shielded desktop data acquisition platform, the noise level is so small with respect to the industrial type data acquisition platforms. The photograph and the

specifications of the data acquisition platform are shown in Figure 4.24 and in the Appendix B.9, respectively.

Figure 4.24 A view of data acquisition platform

4.1.3.3 Data Acquisition Cable

National Instruments SH68-68-EPC data acquisition cable is used to transfer the data coming from the photo-detectors to the data acquisition card. This cable features additional shielding and specific cable pairings to improve the performance of data acquisition. The photograph and the specifications of the data acquisition cable are shown in Figure 4.25 and in the Appendix B.10, respectively.

Figure 4.25 A view of data acquisition cable

4.1.3.4 Data Acquisition Card

National Instruments 6036E data acquisition card is used to transfer the data coming from the photo-detectors to the laptop PC. The sampling rate of the data acquisition is set to 5000 during the experiments. The photograph and the specifications of the data acquisition card are shown in Figure 4.26 and in the Appendix B.11, respectively.

Figure 4.26 A view of data acquisition card

4.1.3.5 Data Acquisition Software

Matlab R2007b version is used to perform data acquisition process. In order to record and monitor the experimental data in real time, data acquisition toolbox of Matlab R2007b is used. First, the data acquisition card driver is installed on the the laptop PC. Then, a simulink block interface is prepared for performing data acquisition process. The photograph of simulink block interface is shown in Figure 4.27.

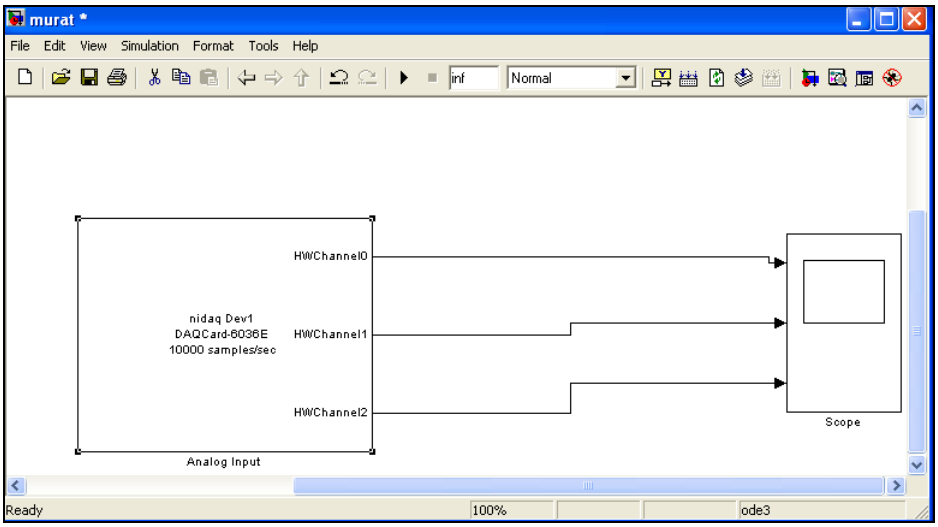

Figure 4.27 Simulink block

The data acquisition features can be adjusted with the help of the source block properties interface. The photograph of the source block properties interface is shown in Figure 4.28.

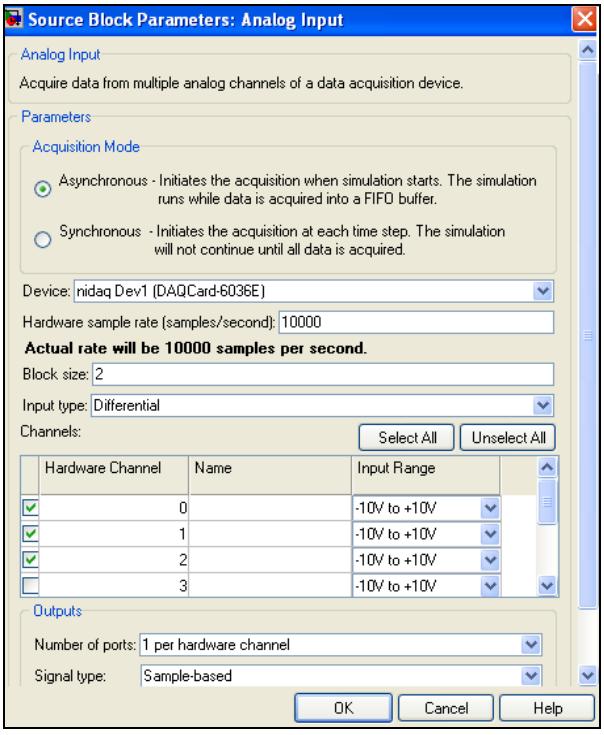

Figure 4.28 Source block properties interface

It can be seen from Figure 4.28 that data acquisition mode is asynchronous and sampling rate is 10000 samples / second. However, the actual sampling rate is 5000 samples/second because there are two blocks for each data acquisition channels. Input type for data acquisition process is differential. It is also seen that three hardware channels are used to perform data acquisition process.

4.1.3.5 Laptop Computer

Data acquisition process is performed on to the laptop computer. The data acquisition process is performed on to the laptop computer because data acquisition card used in this study is a laptop computer compatible card. The photograph and the specifications of the laptop computer are shown in Figure 4.29 and in the Appendix B.12, respectively.

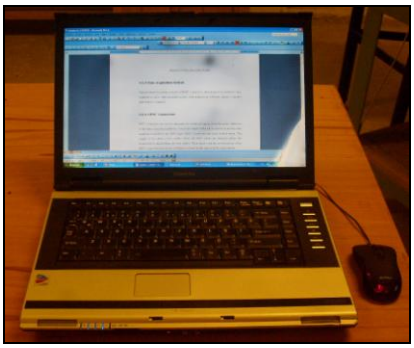

Figure 4.29 A view of laptop computer

4.1.3.6 Desktop Computer

Desktop computer is used to perform data analysis procedure. After data acquisition process is finished, the raw data is sent from the laptop computer to desktop computer. Then, the raw data is processed with the numerical code written in Matlab language in the desktop computer. The photograph and the specifications of

the desktop computer are shown in Figure 4.30 and in the Appendix B.13, respectively.

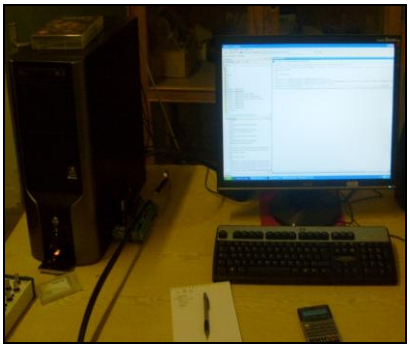

Figure 4.30 A view of desktop computer

4.2 Experimental Procedure

The experimental procedure contains general view of the experimental setup and the steps to be followed in order to perform the experiments in this study.

4.2.1 General view of the Experimental Setup

Photograph and schematic view of experimental setup is shown in Figure 4.31 a and 4.31.b.

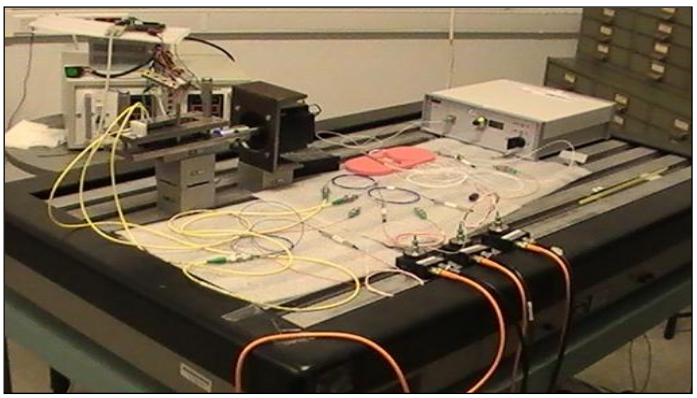

(a)

Figure 4.31 (a) Photo, (b) Schematic view of the experimental setup

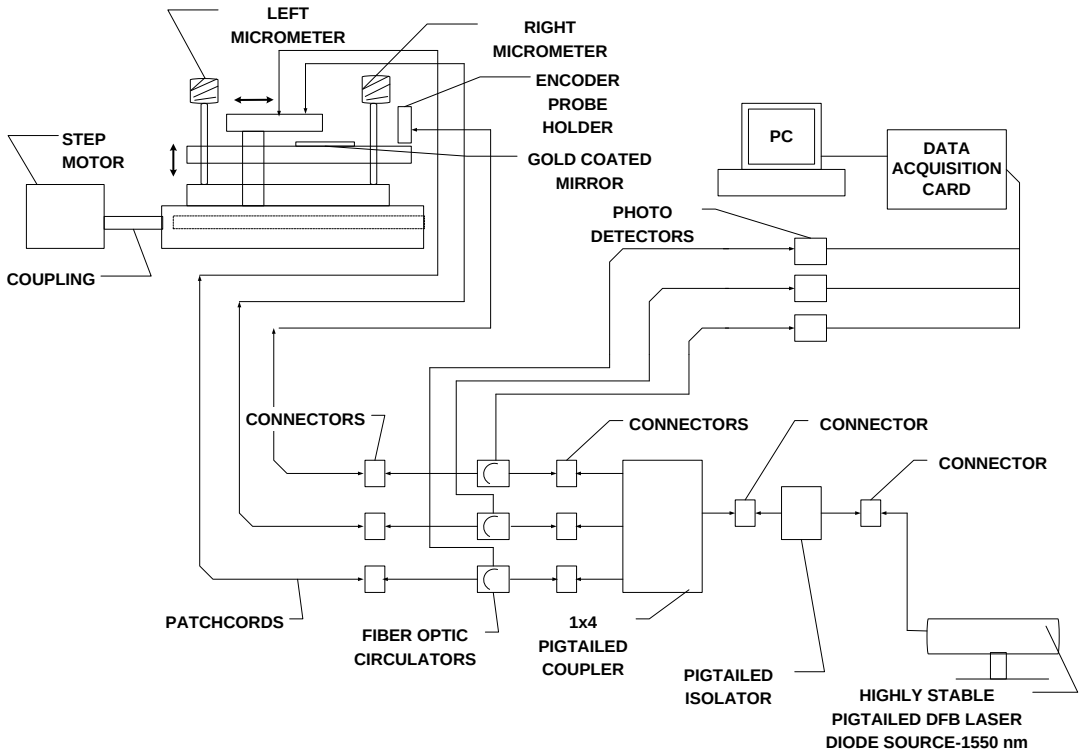

(b)

Figure 4.31 (a) Photo, (b) Schematic view of the experimental setup (continued)

In the experimental setup, a highly stable pigtailed distributed feedback laser (DFB), whose wavelength is 1550 nanometers, is used as laser source. The laser beams emitted from this source are coupled into a fiber optic cable and directed to the pigtailed isolator. Connector is used to connect the isolator and the fiber optic cables. The function of the isolator is to block the back reflected laser beams coming from the other optical components. After the isolator, laser beams are propagating through the 1×4 fiber optic coupler and isolator and fiber optic coupler are connected to each other by using another connector. The function of 1×4 coupler is to divide the coming laser beams into four equal intensity laser beams. Since there are three photo-detectors in this study, one branch of the fiber optic coupler is not used. The laser beams are then directed to the circulators and coupler and circulators are connected to each other by using three connectors. The circulators are used to direct the coming laser beams first to the mechanical stage and second to the photo-detectors after interference occurs. This task is performed

by using fiber optic beam splitters in most of the classical fiber optic interferometers. However, the beam splitters have a cross talk problem between channels. Therefore, the detected intensity decreases with the beam splitters. However, there is no cross talk problem in circulators. There are three ports in the circulators. For the laser beams coming from the laser source, first port is opened and it directs the laser beams to the second port and the laser beams are directed to the mechanical stage. After interference occurs for the interfering beams coming to the circulator, the second port is opened and directs the laser beams to the third port. After that process, the laser beams are directed to the photo-detectors. Therefore, the accuracy of the measured data is increased by using fiber optic circulators in this study.

The laser beams are carried to the mechanical stage with special type patch cords whose one end is a classical fiber optic cable end but the other end is only ferrule. Therefore, three special type patch cords are installed on to the mechanical stage. Two of them are installed to the third plate and detect the vertical distance between the patch cord fiber cable end and the gold coated mirror. The remaining patch cord is installed on to the encoder probe holder and detects the horizontal gap between the patch cord fiber cable end and the small gold coated mirror placed on the right hand side of the third plate. In the mechanical stage, lateral and vertical motions are generated via a step motor and two micrometers, respectively. Step motor motion can be controlled by using a PIC card and interface code in this study. The rotary motion of the step motor is transmitted to the lateral motion carriage shaft with a coupling. This rotary motion is converted to the lateral motion by the lateral motion carriage and transmitted to the third plate by using another vertical shaft. Therefore, third plate moves in the lateral direction in this study. Two micrometers are fixed to the second plate and have a contact with the first plate. Therefore, when the two micrometers move in the vertical direction, the second plate moves in the same direction. In other words, the second plate moves in the vertical direction in this study. First, the two micrometers are set to the required positions and then the three fiber optic cables start to detect vertical and lateral distances in the experiments.

After interference occurs in the patch cords, interfering beams are carried to the circulators again. At that instant, the circulators direct the laser beams to the photo-detectors. The radiation intensity of the laser beams is converted into electrical signals by the photo-detectors. The electrical signals are sent to the data acquisition platform with BNC cables and sent to the laptop computer with data acquisition cable and data acquisition card. Then, the experimental data are recorded on the laptop. Later, the recorded experimental data are sent to the desktop computer in order to perform signal processing of the experimental data.

4.2.2 Steps to be followed in the Experiments

The experiments are conducted in two different mediums namely, air and lubricant. The steps in the experiments in each medium are a little different than each other and they are listed above:

1. Turn on the DFB laser, photo-detectors, power source and PIC card.

2. Plug the USB cable of PIC card to the parallel port of the laptop computer.

3. Start the step motor control interface and choose USB cable port of laptop computer.

4. Connect the data acquisition cable with data acquisition card and plug the data acquisition card on to the laptop computer.

5. Start Matlab R2007b software and data acquisition toolbox of the simulink.

6. Choose the data acquisition card from the data acquisition toolbox interface, select the sampling rate as 10000 samples per second, set the block size as two, select the input type as differential, select three analog input channels, set the number of ports as one per hardware channel and select the signal type as sample-based.

7. Set the micrometers to the required values in the experiments with air. In the experiments with lubricant, first micrometers are set to the reference setting values for the air. Turn the two micrometers in the clockwise direction in order to make closer the probes and the gold coated mirror. Stop turning action when the probes are touching the gold coated mirror. Then, inject the lubricant on to the gold coated mirror by using injector. Wait 2-3 hours for lubricant to diffuse the whole surface.

8. Start the data acquisition process by using data acquisition toolbox interface.

9. Start the step motor by using the step motor control interface in the forward or backward direction with a required number of revolutions.

10. After the step motor finishes its motion, stop the data acquisition process by clicking “Stop” button from the data acquisition toolbox interface.

11. Turn off the laser.

12. Record the experimental data on to the laptop computer and transferring these data on to the desktop computer.

13. Refresh the data acquisition process by clicking the “Build all” button from the data acquisition toolbox interface.

14. Perform data analysis process on to the desktop computer.

Apart from the procedure explained in the above 14 steps, there are four different types of experiments to perform different tasks. These four experiments are:

i) Obtaining “V” curve experiments

ii) Vertical motion experiments

iii) Nonlinear part of “V” curve experiments

iv) Vertical distance measurement experiments

A view of the mechanical stage during the experiments with lubricant is shown in Figure 4.32.

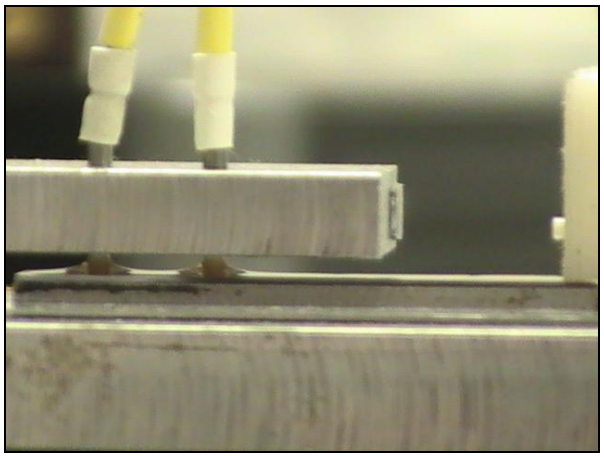

Figure 4.32. A view of the experiment with lubricant

The lubricant used in the experiments is SAE 20 type. The reason why SAE 20 is chosen to be used in the experiments is that it has higher surface tension value. Therefore, the lubricant can spread along the whole gold coated mirror and can not flow on to the second plate. The spread of the lubricant on to the gold coated mirror can be represented with the photos in different durations in Appendix E.

4.2.2.1.1 Obtaining “V” Curve

The reference micrometer settings should be determined to guarantee that a reference setting is found in which the probes and the gold coated mirror are parallel. In order to achieve this, one of the micrometers is fixed and the other one is displaced, and the relative vertical displacement of the two surfaces is measured

via the interferometer. The schematic view of these experiments in the forward direction with air is shown in Figure 4.33.

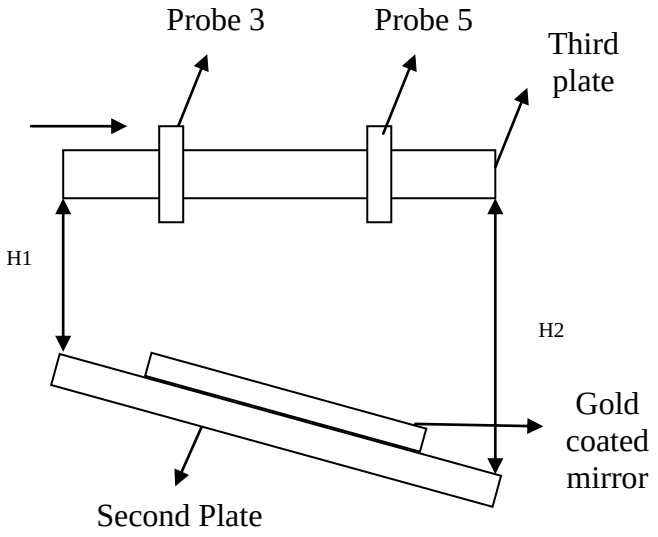

Figure 4.33 Schematic view of "V" curve experiment

This procedure results in a "V" shaped curve, the minimum of which indicates the setting where the two plates are parallel. By determining the reference micrometer settings, the desired slope between the two plates can be implemented. The "V" shaped curves used in obtaining a parallel configuration of the two surfaces with air and a lubricant is shown in Figure 4.34.a and 4.34.b, respectively.

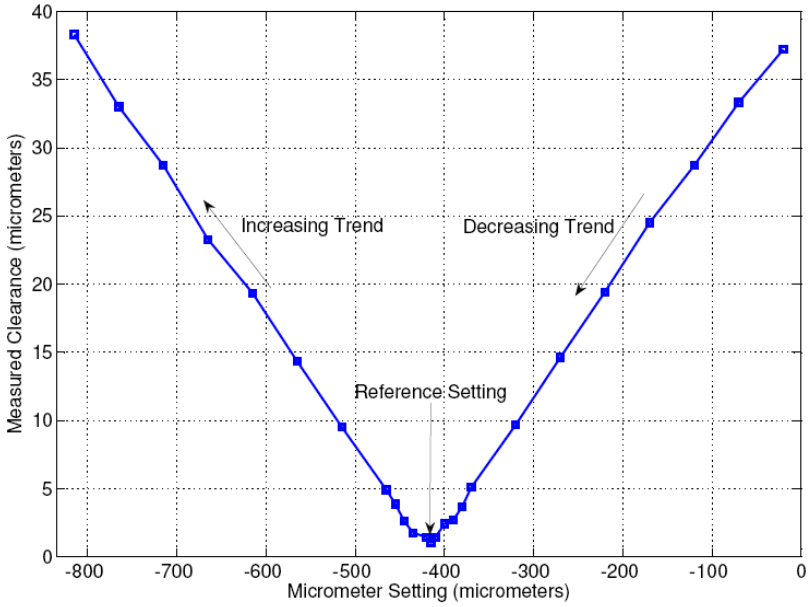

(a)

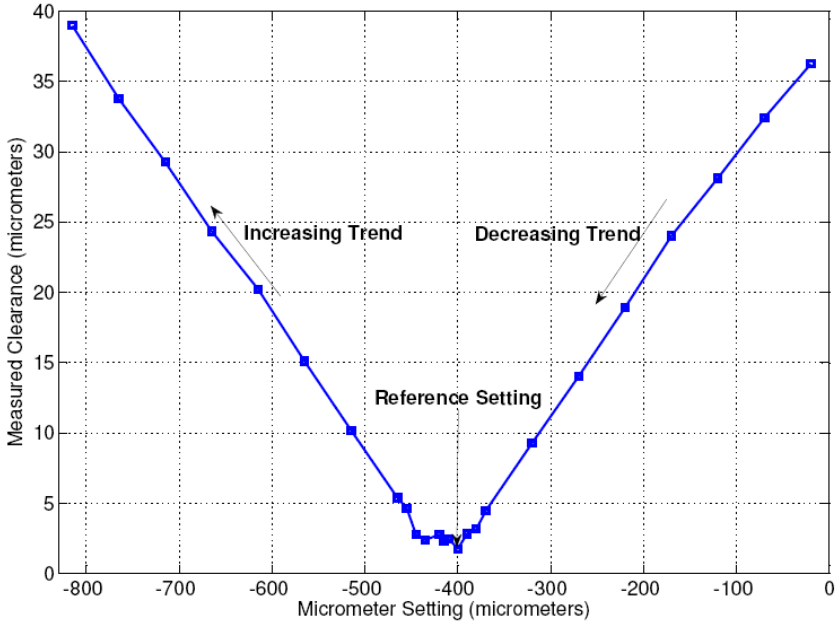

(b)

Figure 4.34. “V” curve (a) air, (b) lubricant

In Figure 4.34, values on the vertical axis represent vertical distances between the patch cord end and the gold coated mirror measured via fiber optic interferometer. On the other hand, the values on the horizontal axis represent the micrometer setting of the micrometer in motion. In order to obtain this “V” curve, first the two

micrometers are set to the same value and this setting can be represented as the zero value on the horizontal axis. Then, this micrometer is turned into the counter clockwise direction and the values with minus signs mean that the micrometer is turned into the counter clockwise direction. From this "V" curve, it is seen that the vertical distances start to decrease up to the -415 μm setting value for air and -400 μm setting value for lubricant. After these setting values, the vertical distances start to increase. Therefore, parallelism of the patch cord ends and the gold coated mirror can be achieved by setting the micrometer at -415 μm and -400 μm for air and lubricant, respectively. There are two different trend regions in Figure 4.34. There is a decreasing trend region between the micrometer setting values of 0 to -415 μm for air and 0 to -400 μm for lubricant and there is a increasing trend region between the micrometer setting values of -415 μm to -800 μm for air and -400 μm to -800 μm for lubricant. If this "V" curve is not determined, the parallelism setting of the two micrometers can not be determined. Therefore, there may occur some unsmooth interferometry results in the experiments since there is always a possibility of passing through two different trend regions, i.e. decreasing and increasing, in the same experiment. All experiments are performed after setting the parallelism according to the "V" curve.

4.2.2.1.2 Vertical Motion Experiments

After determining the parallelism of the probe and the gold coated plate, the vertical motion experiments are conducted. Initially, the two micrometers are set to the reference value settings, -415 μm for air and -400 μm for lubricant , at which probes and gold coated plate are parallel to each other. Later, the two micrometers are rotated in the clockwise direction and the vertical distance between the probe and the gold coated plate decreases. This process continues till the two probes are within a very close proximity of the gold coated plate. Finally, the two micrometers are rotated in the counter clockwise direction so that the vertical distance increases and the data for this process is recorded on laptop. The schematic view of this motion in air and lubricant is shown in Figure 4.35.a and 4.35.b, respectively.

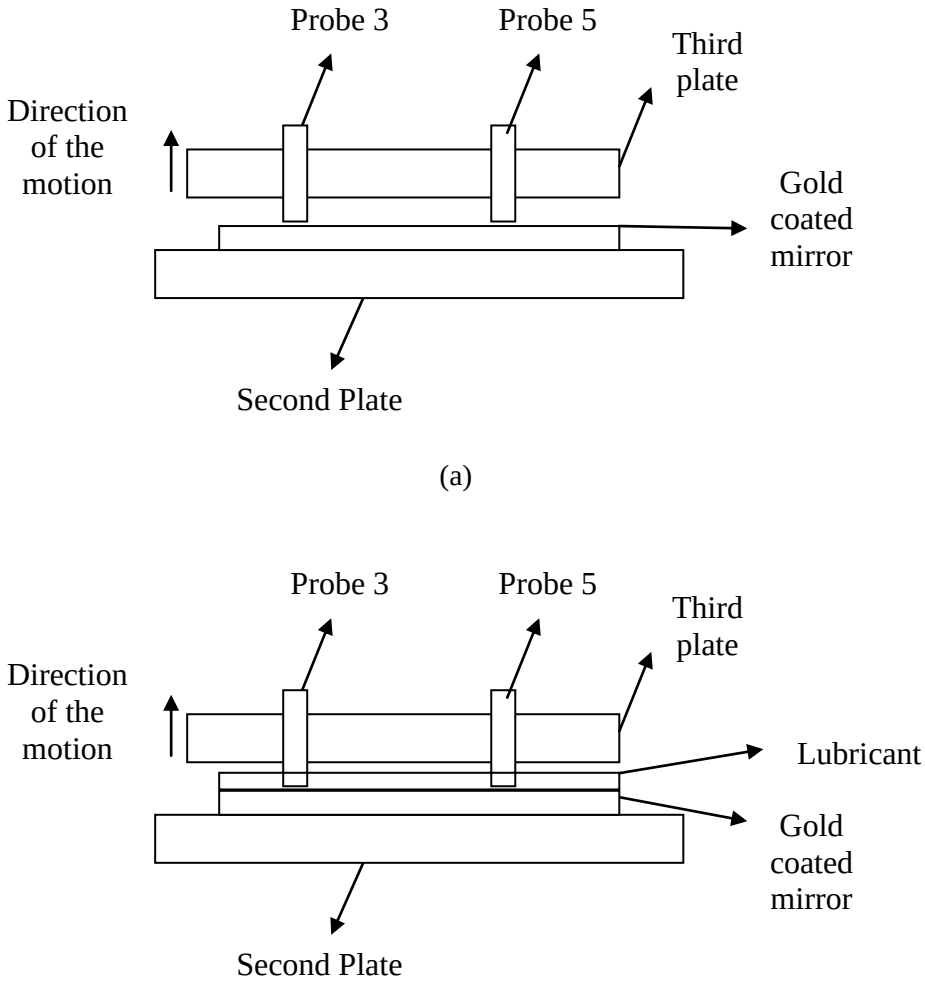

Figure 4.35 Schematic view of vertical motion experiment. (a) air, (b) lubricant

The experimental data for this vertical motion for the probe 3 and probe 5 in air and lubricant are shown in Figures 4.36a , 4.36.b, 4.36.c and 4.36.d, respectively.

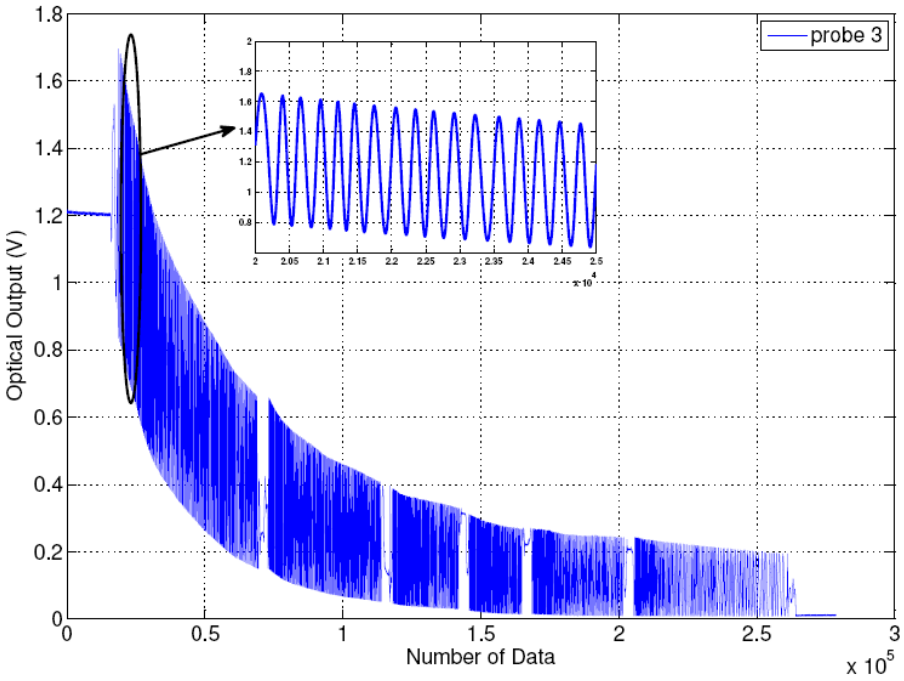

(a)

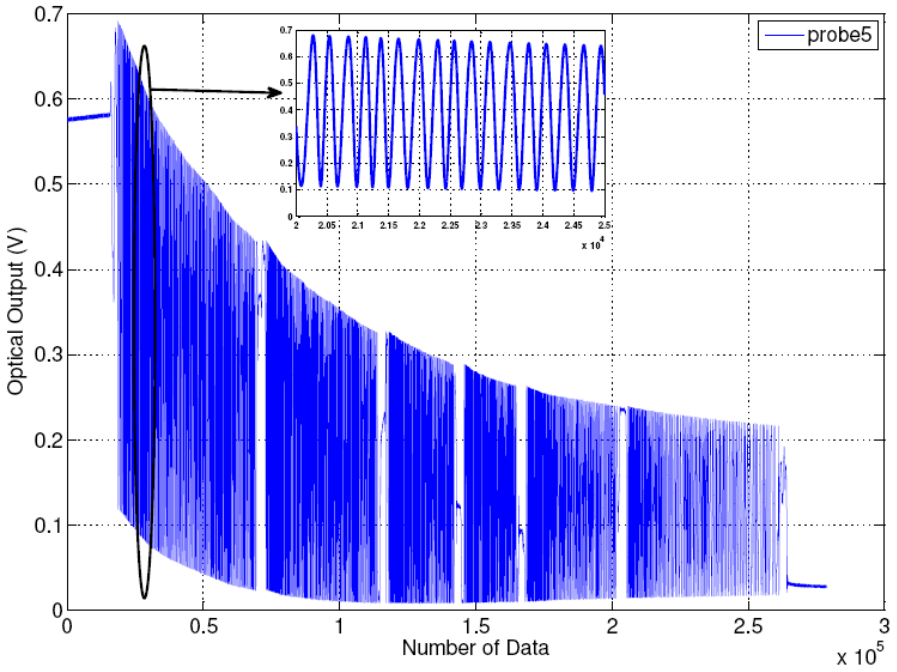

(b)

Figure 4.36. (a) Probe 3 in air, (b) Probe 5 in air, (c) Probe 3 in lubricant, (d) Probe5 in lubricant

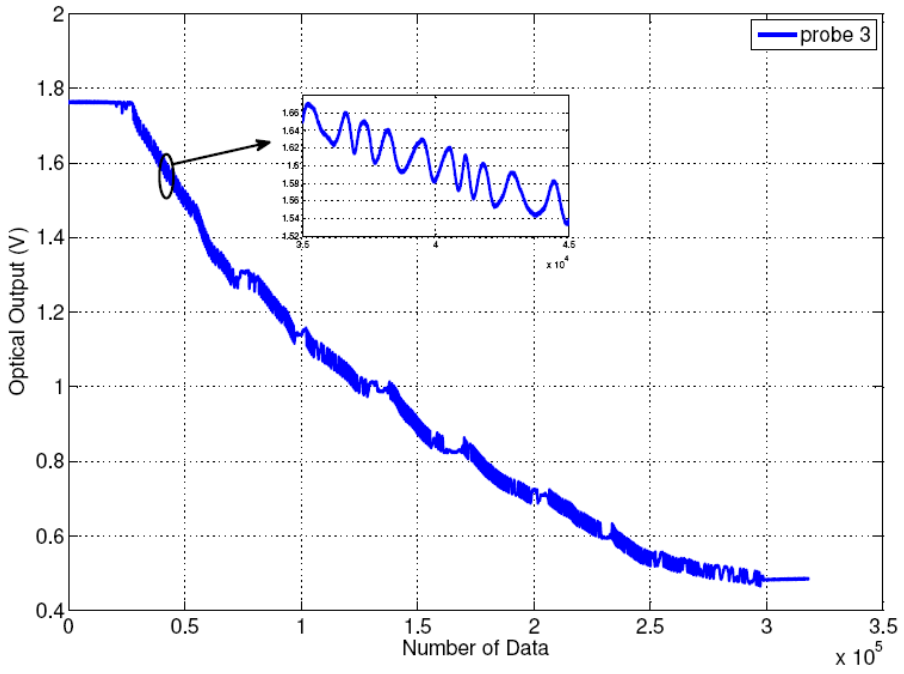

(c)

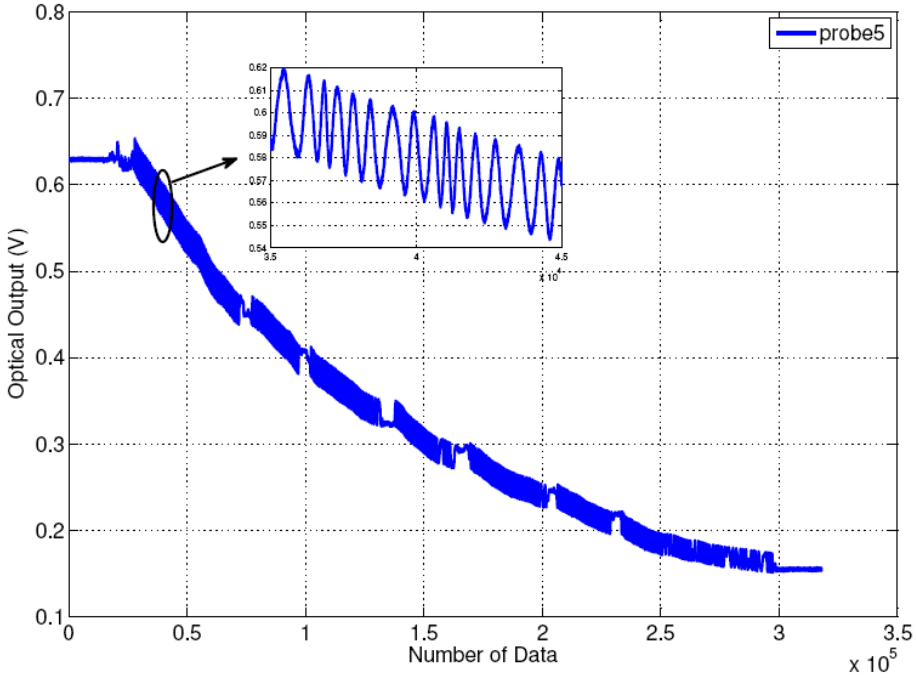

(d)

Figure 4.36. (a) Probe 3 in air, (b) Probe 5 in air, (c) Probe 3 in lubricant, (d) Probe5 in lubricant (continued)

In the Figure 4.36a, b, c and d, the experimental results in the vertical motion are represented for probes 3 and 5 in air and lubricant, respectively. It can be seen that the vertical distances between the probes and the gold plated mirror are not equal since the detected intensities are different for probe 3 and probe 5. The aim of these experiments is to determine the absolute vertical distances between the probe ends and the gold coated mirror in any experiments. In order to detect the vertical distances between the probe ends and the gold coated mirror, the detected intensity at any location and it's nearest maximum and minimum intensities are put into the 4.36a, 4.36b, 4.36c and 4.36d. The absolute vertical distance can then be calculated using the numerical code written in Matlab. The details of the numerical code are explained in the Chapter 5 and Appendix D.

4.2.2.1.3 Nonlinear Part of "V" Curve Experiments

After performing the vertical motion experiments, experiments are conducted for the nonlinear part of "V" curve to check the reference setting values of the two micrometers. The nonlinear part of "V" curve results for air and lubricant are shown in Figure 4.37a and 4.37.b, respectively.

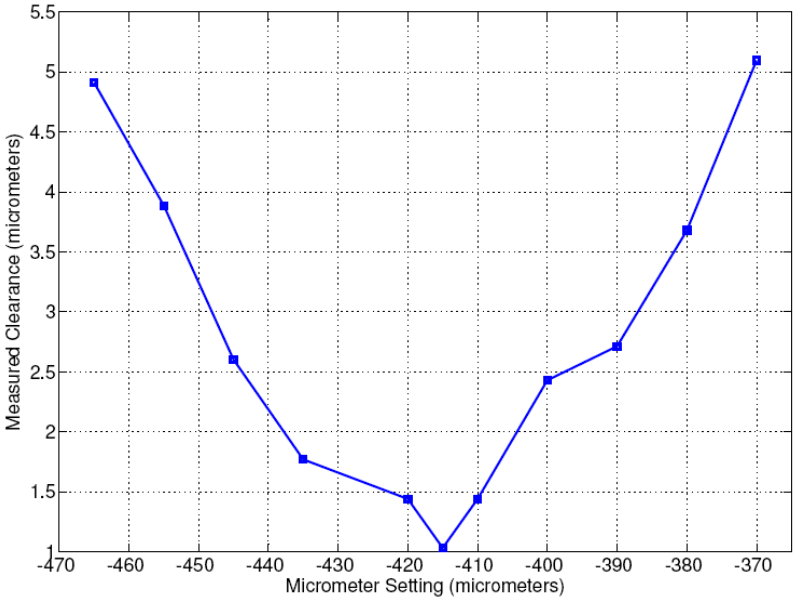

(a)

Figure 4.37 Nonlinear part of "V" curve experiments.(a) air, (b) lubricant

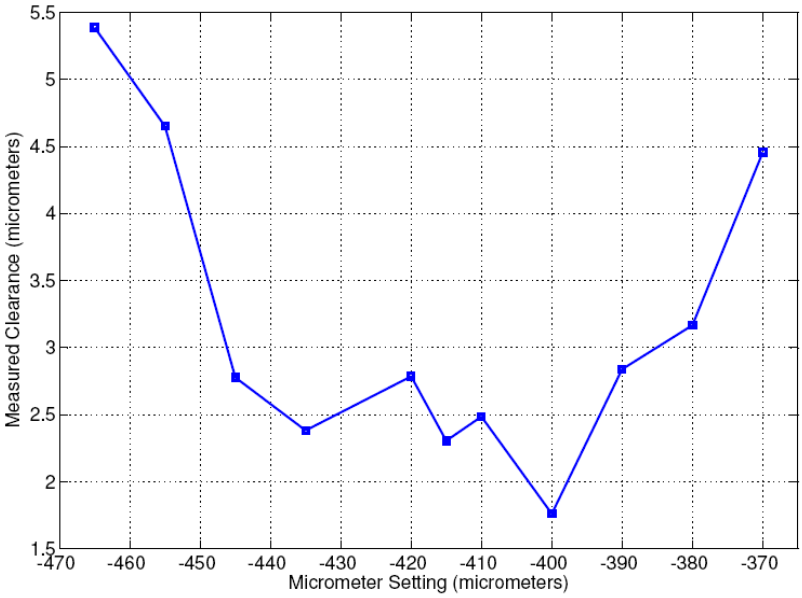

(b)

Figure 4.37 Nonlinear part of "V" curve experiments.(a) air, (b) lubricant (continued)

It is seen from Figures 4.37.a and 4.37.b that the minimum value obtained from the nonlinear part of the "V" curve remains unchanged compared to the original "V" curves shown in Figures 4.34.a and 4.34.b.

4.2.2.1.4 Vertical Distance Measurement Experiments

After performing nonlinear part of the "V" curve experiments, the vertical distance measurement experiments are conducted. In these experiments, two micrometers are used to adjust the relative vertical distances between the probe ends and the gold coated mirror. The vertical distances are detected by using two probes installed on to the third plate and the lateral displacement is detected by using another probe called "encoder probe" installed on to the encoder probe holder. The schematic views of these experiments in the forward direction in air and lubricant are shown in Figure 4.38a and 4.38b, respectively.

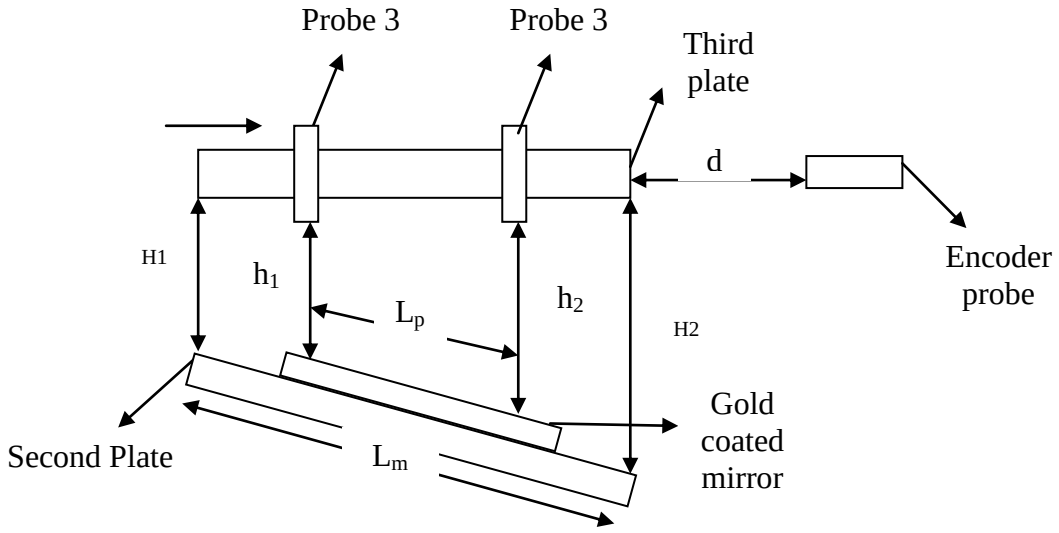

(a)

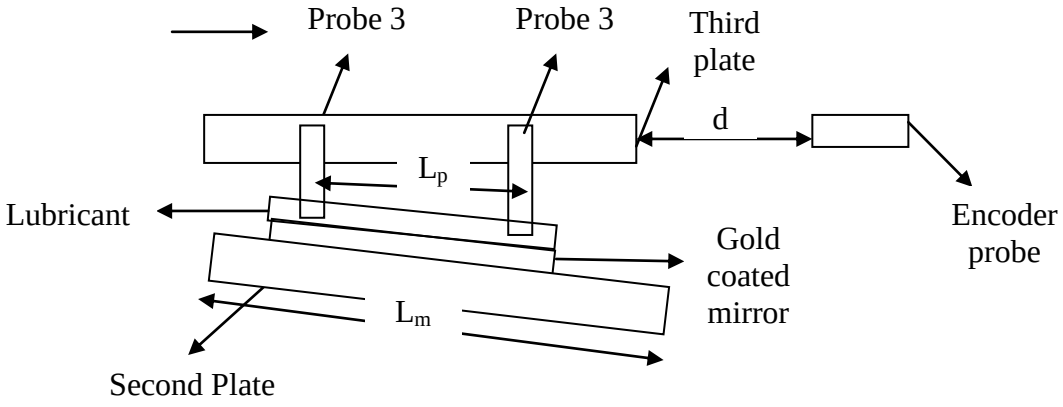

(b)

Figure 4.38. Schematic views of vertical distance measurement experiments (a) air , (b) lubricant

Using the encoder probe as an interferometer, the lateral displacement is measured to be 900 μm of each revolution of the step motor. Since the horizontal distance between the two micrometers is known and the number of the revolutions of step motor during the experiments is 15, the vertical distance between the starting and end points of the probes is equal to:

$$\Delta h = | h_1 - h_2 | = \frac{| H_1 - H_2 | \times L_p}{L_m} \qquad (4.1)$$

where, Δh represents the relative vertical distance between the starting and the end points of the experiments and the probe, H_1 and H_2 are the vertical distances between the second plate and the third plate at the left and right micrometer locations, respectively, d is the gap between the encoder probe and the small gold plated mirror on the third plate, L_p is the lateral motion displacement of the probes during the experiments and L_m represents the horizontal distance between the two micrometers. Therefore, Δh values can be easily calculated by knowing the micrometer settings with respect to the reference settings representing the parallelism of the second and the third plates.

Another numerical code is written to find h_1 and h_2 values in each experiment. The detailed explanation of this code is mentioned in the Appendix F. Then, h_1 and h_2 values are aimed to be kept constant for all of the experiments in the forward and backward directions, respectively. Therefore, the intensities detected by photo-detectors are the same in all experiments in the same directions.

CHAPTER 5

DATA ANALYSIS PROCEDURE

In this chapter, data analysis procedure which consists of the rough data filtering operation, numerical code algorithm, linear curve fit process, 9^{th} degree polynomial curve fit and sinusoidal curve fit processes are explained.

5.1 Rough Data Filtering

Initially, rough data is obtained with data acquisition system. The rough data is shown in Figure 5.1 when $\Delta h = 15\ \mu$m with air in the forward direction for fiber optic probe 3.

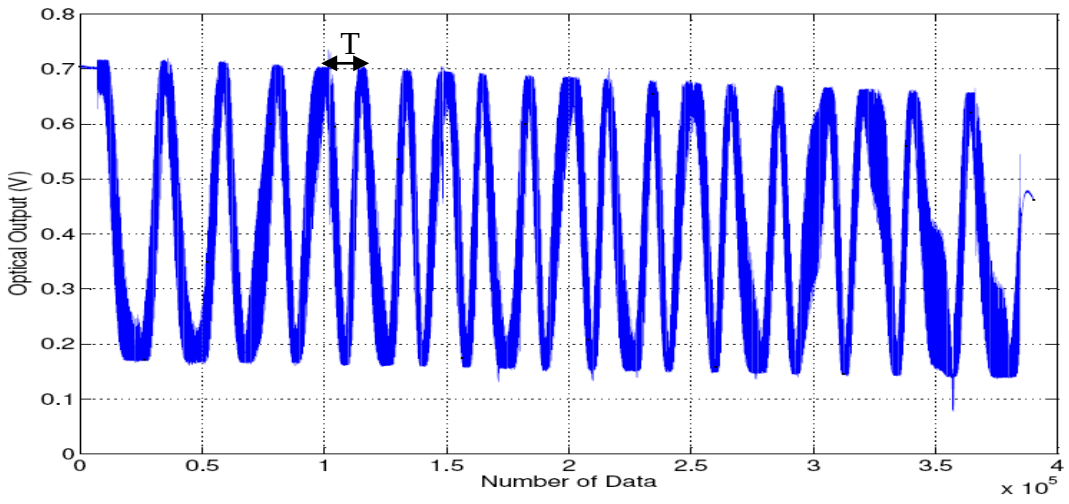

Figure 5.1. Rough data

After obtaining rough data, it can be seen that there are different noise levels in the rough data. Therefore, Fourier transform of the rough data is taken in order to

interpret the different dynamics in the experimental setup. Fourier transform of the rough data is shown in Figure 5.2.

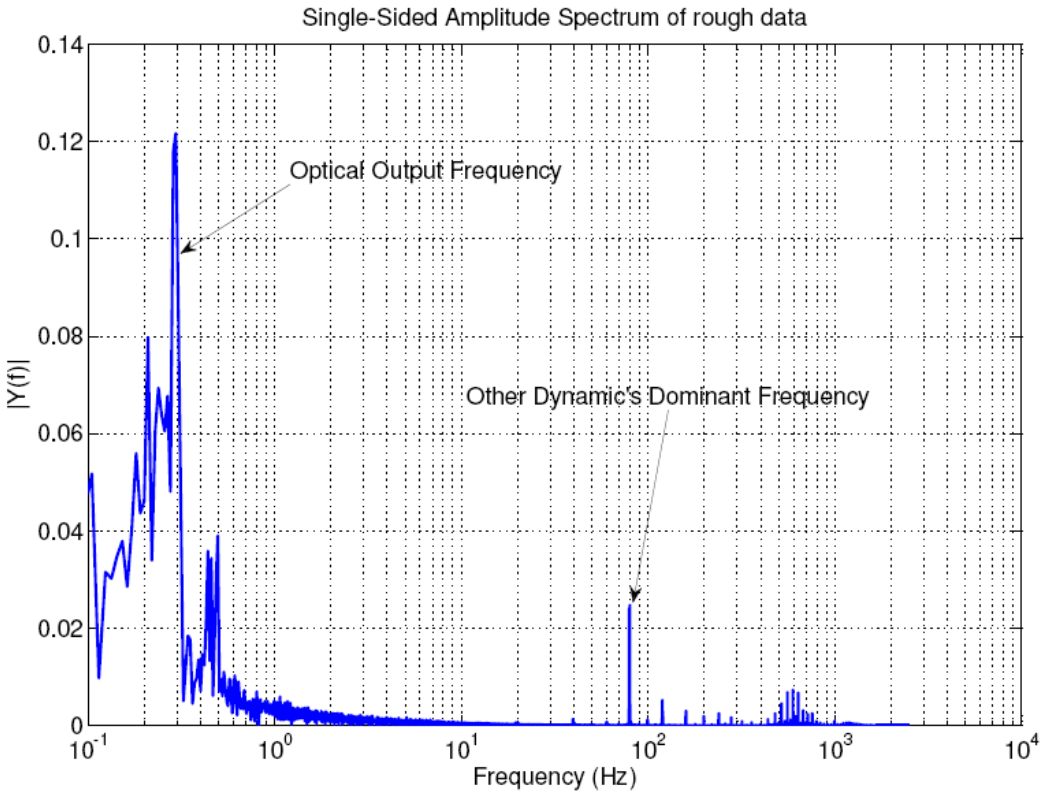

Figure 5.2. Fourier transform of rough data

It is seen from Figure 5.2 that the dominant frequency in the experimental setup occurs at 0.3 Hz. It can be seen from the Figure 5.1 that the period of the rough data is approximately 15000 data. Since the sampling rate of the experiment is 5000 samples / second, the period of the experiments is equal to 3 seconds. Therefore, the optical output frequency is approximately equal to 1/3 = 0.3 Hz. Therefore, the dominant frequency in the Figure 5.2 is due to the optical output frequency. The other dominant frequency occurs at the frequency of 80 Hz in Figure 5.2. Since the frequency of the step motor can be controlled by the interface code and the frequency is equal to 1 kHz, the concentration should take place around 1 kHz frequency. The Fourier transform of the rough data around 1 kHz frequency is shown in Figure 5.3.

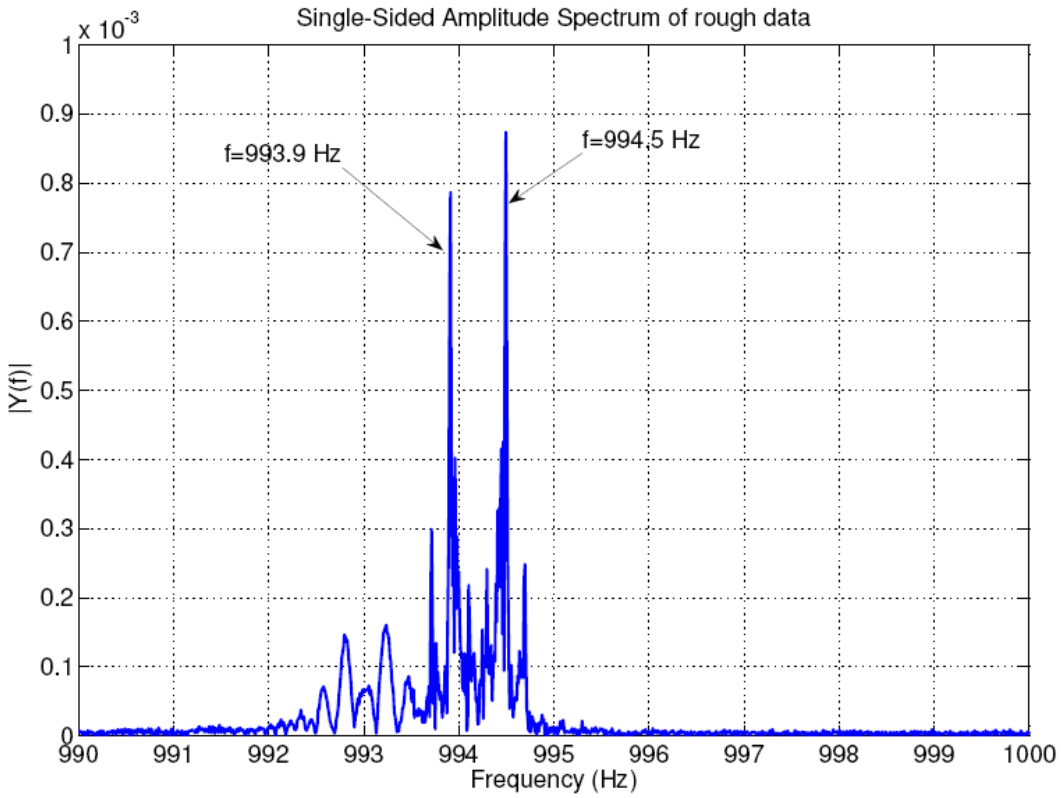

Figure 5.3. Fourier transform of rough data around 1 kHz

The frequency of the step motor can be determined at the two frequencies of 999.3 Hz and 994.5 Hz in Figure 5.3. After interpreting the different noise levels and the optical output frequency, filtering operation is performed to the rough data to filter the different noise levels to obtain smoother optical output data.

The filtering operation can be performed in frequency domain or time domain. Low pass filtering operation can be used to filter the rough data in frequency domain. However, the use of low pass filter adds different dynamics to the rough data and the rough data become different after filtering operation is performed. Therefore, this choice is not preferred. “Moving average” method can be used to filter the rough data in time domain. In this method, the rough data is filtered by replacing each data point with the average of the neighborhood data points defined within the span. The method of moving average is explained in Appendix G in detail. Therefore, the moving average method is chosen to filter the rough data. Different

span size values are tried to determine the optimum value of span size. The result of different span size filtering operation is shown in Figure 5.4.

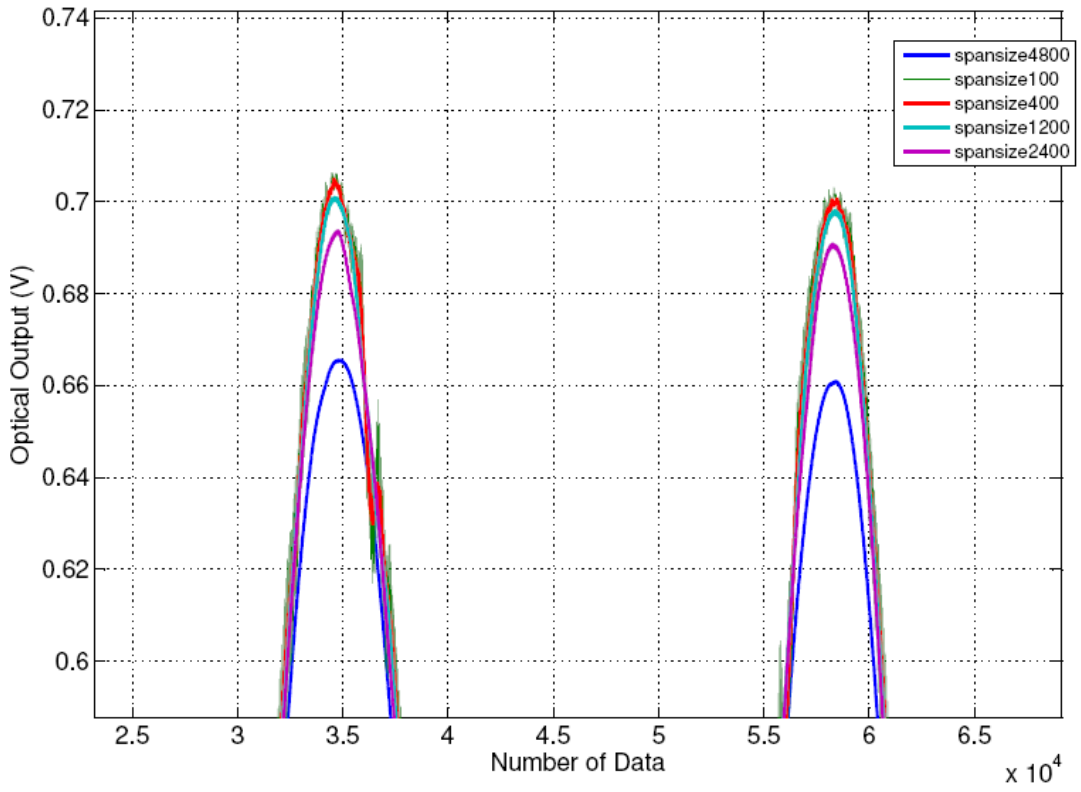

Figure 5.4. Different span size filtering operation

According to the results of different span size filtering operations, the span size is selected as 400. Since the sampling rate of the experiments is 5000 samples per second, this filtering operation should filter the frequencies larger than 5000/400=12.5 Hz. The filtered data and Fourier transform of the filtered data is shown in Figure 5.4.a and 5.4.b, respectively.

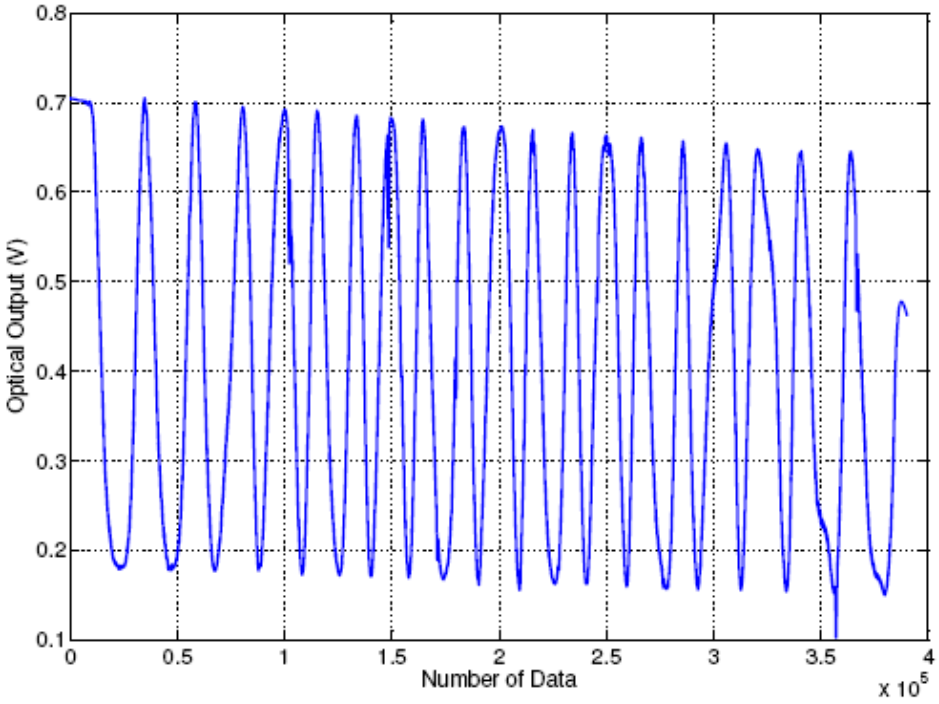

(a)

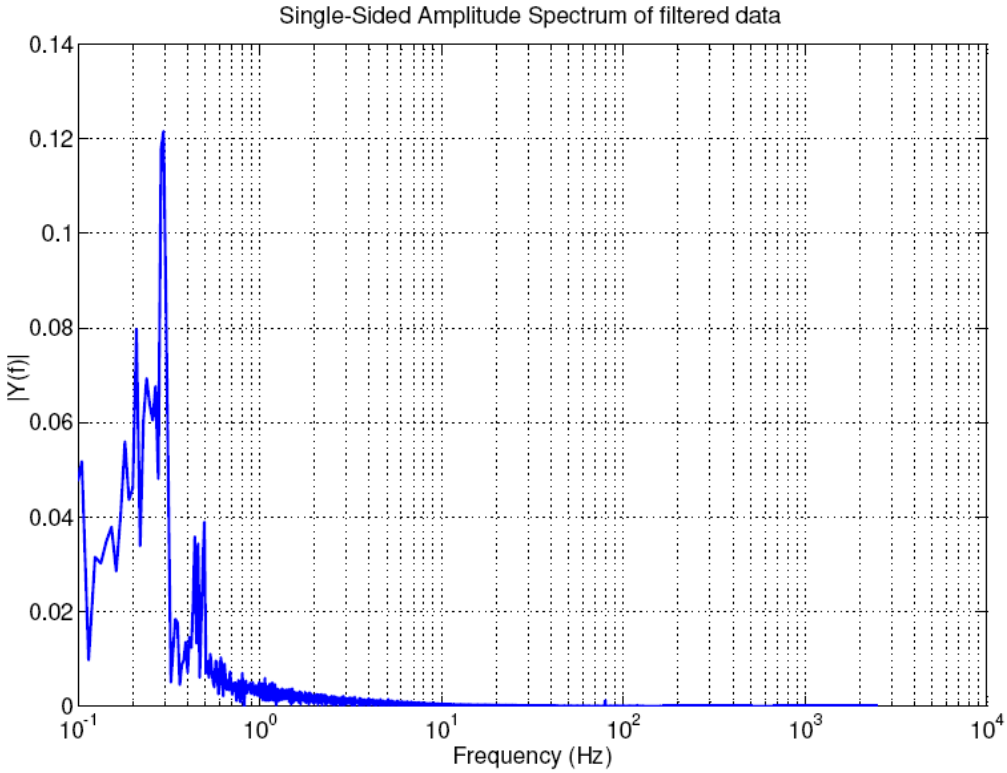

(b)

Figure 5.5. (a) Filtered data, (b) Fourier transform of the filtered data

It is observed that the frequency levels higher than 12.5 Hz are filtered with the moving average method with comparing the Figure 5.2 and Figure 5.5.b. After filtering the optical data, the optical data should be converted into the vertical distance. Furthermore, the optical output of probe 1 should be converted to horizontal distance. The optical output of probe is shown in Figure 5.6.

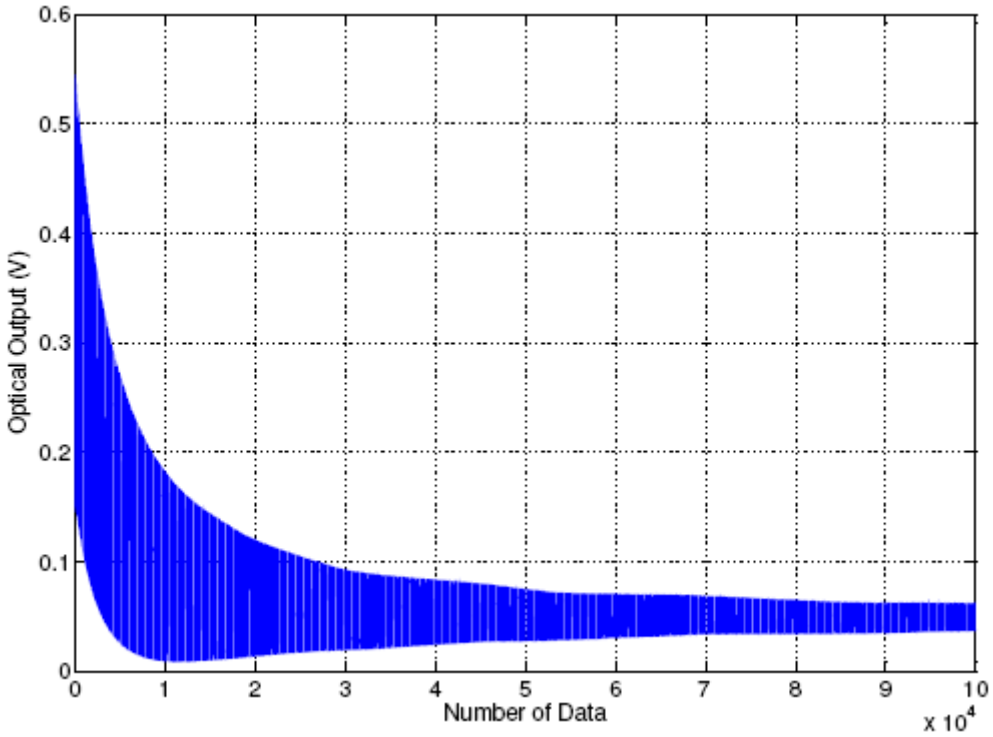

Figure 5.6. Probe 1 optical output data

5.2 Numerical Code Algorithm

A numerical code is written in Matlab and in Excel to convert the optical output data of probes 1, 3 and 5 to horizontal and vertical distances. The numerical code algorithm is explained in the following steps:

1. The first step to convert the optical output into the distance is to determine maximum and minimum initial limits to find the local maximum and

minimum points' x and y axis locations. The local maximum and minimum first two points of optical output when $\Delta h = 15\ \mu$m with air in the forward direction for fiber optic probe 3 is shown in Figure 5.7.

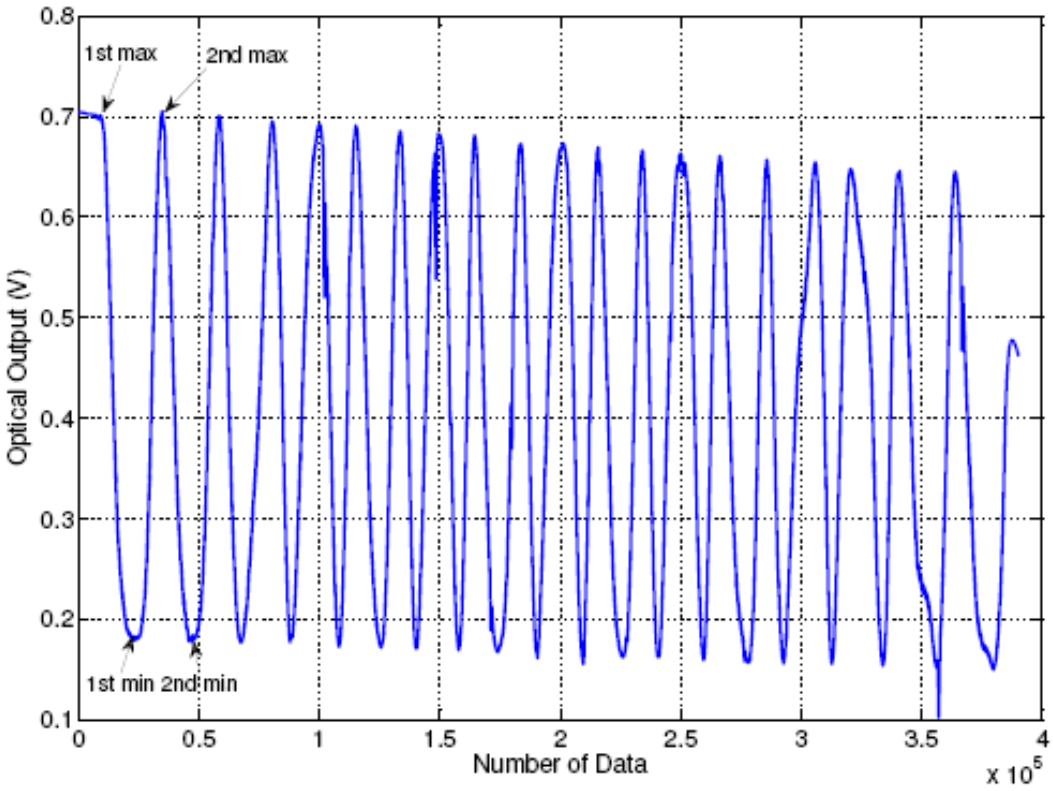

Figure 5.7. Local maximum and minimum first two points

Two initial limits are needed to determine the local maximum and minimum points in Figure 5.7. These limits are called initial maximum and initial minimum limits. The filtered data, maximum initial limit and minimum initial limit for the same data is shown in Figure 5.8.

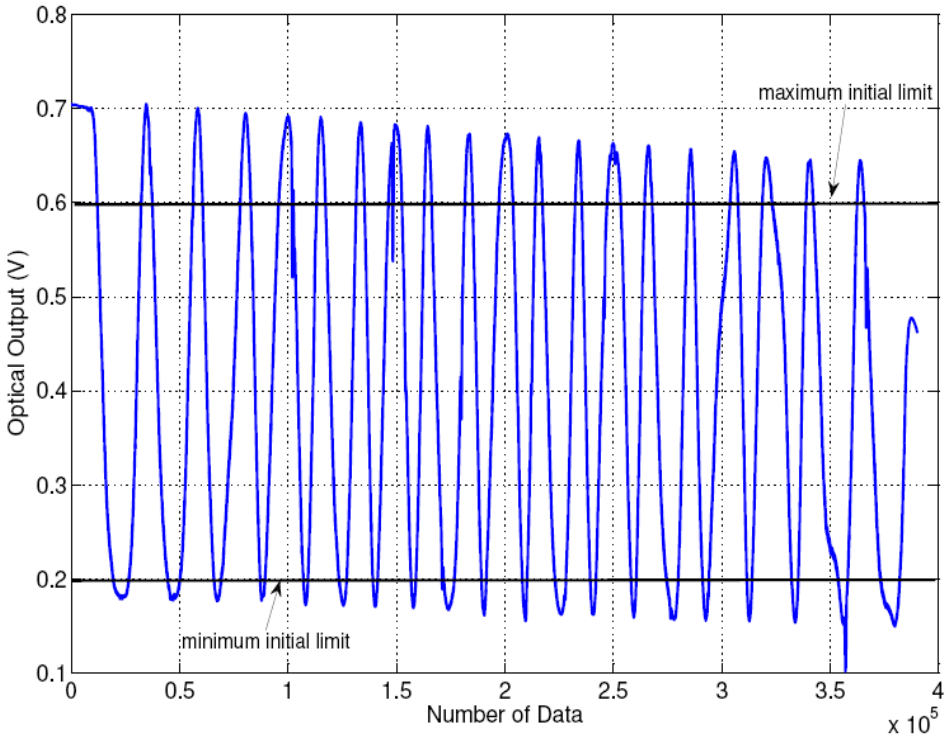

Figure 5.8. Filtered data, maximum and minimum initial limits

The maximum and minimum initial limits for the data in Figure 5.8 are 0.6 V (Volts) and 0.2 V respectively. The method for determining the maximum and minimum initial limits explained above can be applied to the optical data of probe 3 and probe 5 easily. However, this method can not be applied to determine the maximum and minimum initial limits for the optical data of probe 1 which is shown in Figure 5.6 because the local maximum and minimum points' intensities are too different from each other. In order to obtain maximum and minimum initial limits for analyzing the optical data of probe 1, another numerical code is written in Excel. In this code, the formulae [10] used to get the optical output versus displacement curve using different inputs. The formula is shown in Eq. 5.1.

$$I = I_0 \times (R_1 + (1-R_1)^2 \times R + 2 \times (1-R_1) \times \sqrt{R \times R_1} \times \frac{\sin(\varepsilon)}{\varepsilon} \times \cos(4 \times \pi \times \frac{x_0}{\lambda})) \quad (5.1)$$

By using Equation 5.1, the detected optical intensity by photo-detectors, maximum and minimum initial limits can be easily achieved. The detailed explanation of the Excel code is given in Appendix H. The optical output, maximum and minimum initial limits for the probe 1 are shown in Figure 5.9.

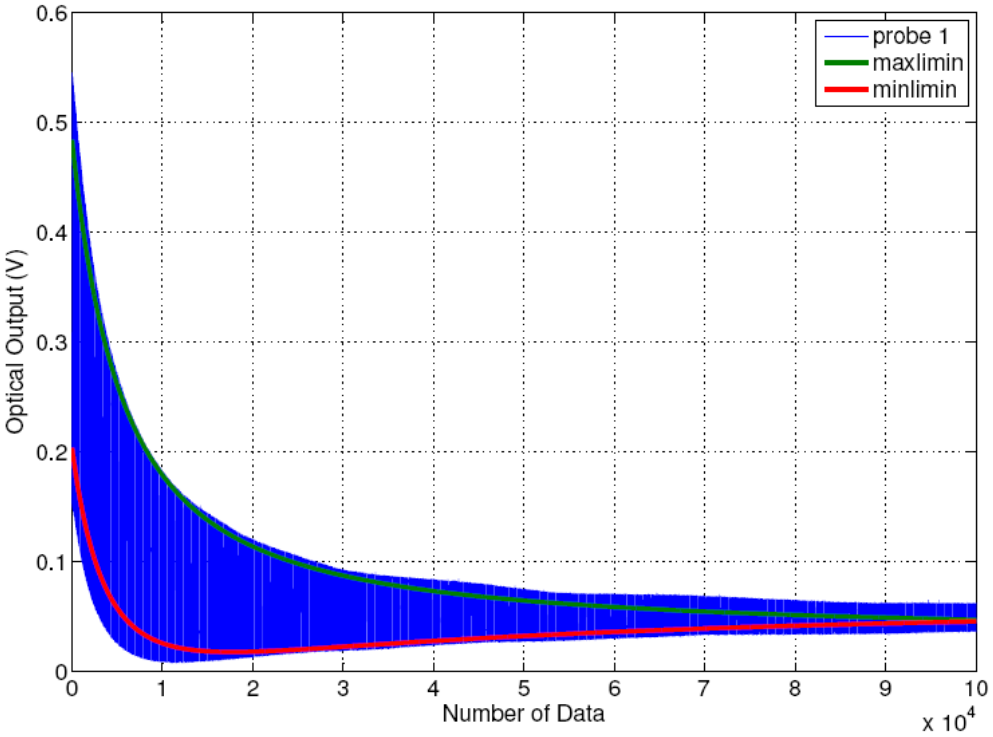

Figure 5.9. Filtered data, maximum and minimum initial limits for probe 1

2. Second step is to find the first points' locations whose intensities are larger than maximum initial limit or smaller than minimum initial limit. The numerical code starts to seek a point whose intensity is larger than the maximum initial limit or smaller than the minimum initial limit. If the code finds a point which satisfies the condition explained above, then it records this points' *x* and *y* axis locations. Then, it starts to find a point which satisfies the inverse condition of the previous statement. For example, if the code finds a point whose intensity is larger than maximum initial limit, after that point the code starts to seek a point whose intensity is smaller than the minimum initial limit. The x locations of these points are recorded into so called "maxi" and "mini" arrays.

3. The next step is to determine the *x* and *y* axis locations of local maximum and minimum points. The code takes the first elements of "maxi" and "mini" arrays and starts to compare them. The aim of this comparison is to determine the element which has the smallest *x* location. After this comparison, the code is decided the sequence of the local maximum and minimum points. Then, it starts to seek the local maximum or local minimum points between *x* locations of the "maxi" and "mini" array elements. For example, if the first local point is a maximum point, the code seeks a maximum point between the *x* locations of the first elements of the "maxi" and "mini" arrays or vice-versa. This process continues up to the determination of the last local maximum and minimum points' *x* location. This procedure is shown in Figure 5.10.

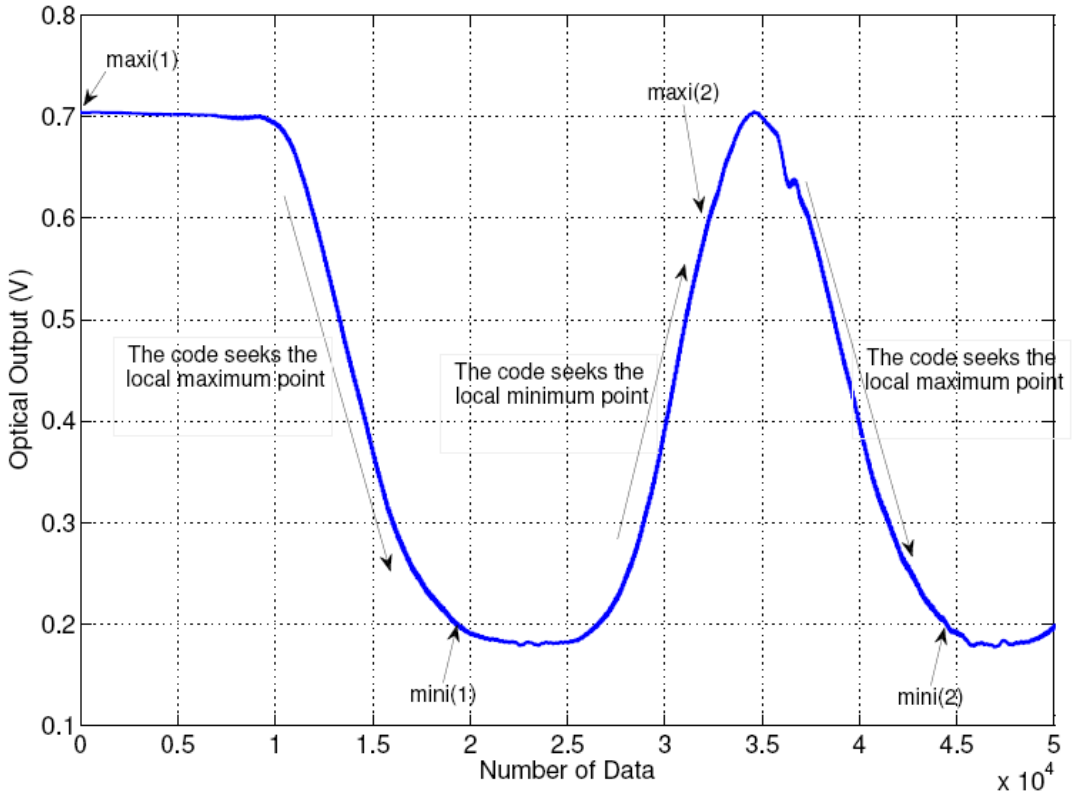

Figure 5.10. Determination of the locations of local maximum and minimum points

4. The last step is to convert the optical output into the vertical distance. The local maximum and minimum points' x locations are recorded into the so-called "xmax" and "xmin" arrays. The code compares the first elements of "xmax" and "xmin" arrays. According to the result of that comparison, the code increases the number of elements of "xmax" or "xmin" array by one and makes the first and second elements equal. For example, in the data shown in Figure 5.10, the first element of "xmax" array is smaller than the first element of "xmin" array. Therefore, the code increases the number of elements of "xmin" array by one, and in this new array the first and the second elements are equal to each other. This new array is called "xminnew" or vice-versa. Then, the code starts to calculate each data point's vertical distance with reference to the first element intensity of "xminnew" array or vice-versa. To perform this task, the code calculates the phase of each point. In the Eq. 5.2, the interference equation is ;

$$I = I_1 + I_2 + 2*\sqrt{I_1 * I_2} * \cos(\Delta\phi) \tag{5.2}$$

In Eq. 5.2, if the phase difference equals to 0, then the maximum intensity occurs and if it equals to π then minimum intensity occurs at the photo-detector. These results are shown in Eqs. 5.3.a and 5.3.b.

$$I_{\max} = I_1 + I_2 + 2*\sqrt{I_1 * I_2} \tag{5.3.a}$$

$$I_{\min} = I_1 + I_2 - 2*\sqrt{I_1 * I_2} \tag{5.3.b}$$

In Eqs. 5.3.a and 5.3.b the two terms which are $I_1 + I_2$ and $2\times\sqrt{I_1 \times I_2}$ are common. They can be written in terms of $I_{\max}$ and $I_{\min}$. If the Equations 5.3.a and 5.3.b are added to each other and divided by two, $I_1 + I_2$ can be obtained. If the Eqs. 5.3.a and 5.3.b are subtracted from to each other and

divided by two, $2\times\sqrt{I_1\times I_2}$ can be obtained. The results are shown in Equations 5.4.a and 5.4.b.

$$I_1 + I_2 = \frac{I_{\max} + I_{\min}}{2} \tag{5.4.a}$$

$$2\times I_1 \times I_2 = \frac{I_{\max} - I_{\min}}{2} \tag{5.4.b}$$

Therefore, the Equation 5.2 can be rewritten in terms of $I_{\max}$ and $I_{\min}$ with using Equations 5.4.a and 5.4.b in the Equation 5.5.

$$I = (\frac{I_{\max} + I_{\min}}{2}) + (\frac{I_{\max} - I_{\min}}{2}) \times \cos(\Delta\phi) \tag{5.5}$$

Therefore, the phase difference of any point with respect to the local maximum or minimum points can be calculated by using Equation 5.5 and it is shown in Equation 5.6.

$$\Delta\phi = arc\cos(\frac{I - (\frac{I_{\max} + I_{\min}}{2})}{(\frac{I_{\max} - I_{\min}}{2})}) \tag{5.6}$$

In the numerical code $\frac{I_{\max} + I_{\min}}{2}$ is denoted by A, and $\frac{I_{\max} - I_{\min}}{2}$ is denoted by B. Therefore, Equation 5.6 reduces to Equation 5.7 in the numerical code.

$$\Delta\phi = arc\cos(\frac{I - A}{B}) \tag{5.7}$$

After calculating the phase difference of each point, the code multiplies the phase difference by $\frac{\lambda}{4\times\pi}$ to convert the phase difference into distance. Then, the code adds this distance value to the reference distance value assigned each local maximum or minimum point. These reference values are the positive integer multiples of $\frac{\lambda}{4}$. This process continues up to the last point of the data. This process is shown in Figure 5.11.

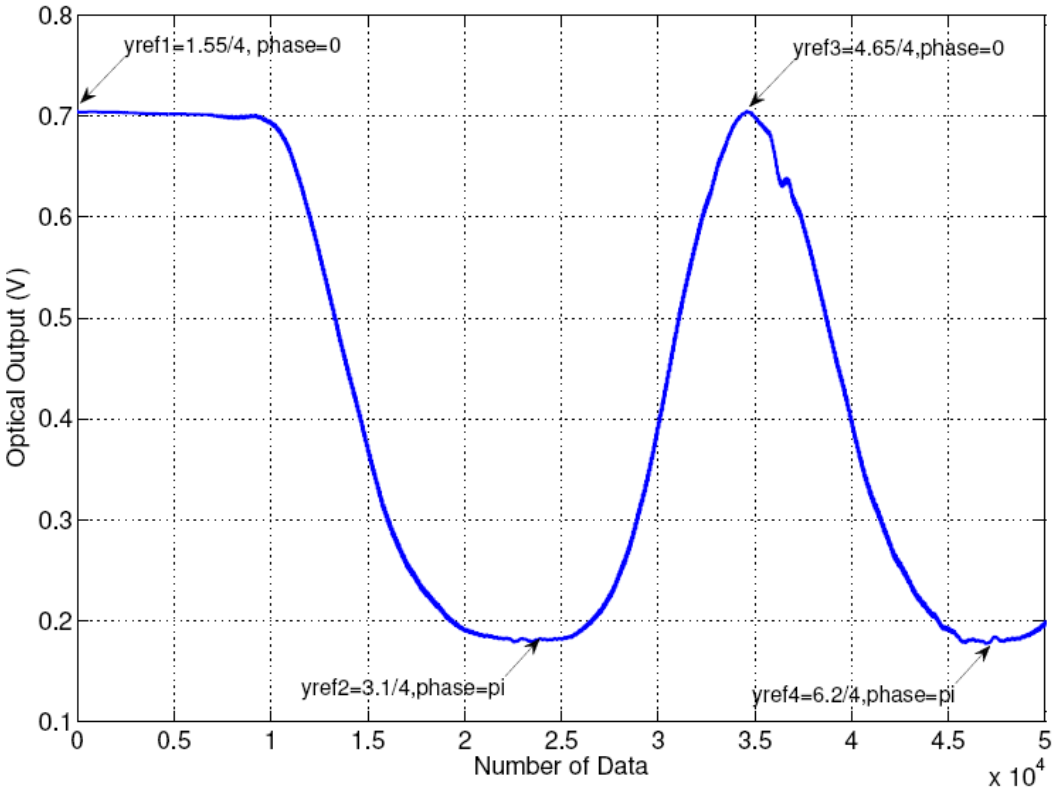

Figure 5.11. Determination of the vertical distances from the optical output

Two different functions are used to test the numerical code before applying it to the experimental data. The types and the coefficient of the two functions are presented in Table 5.1.

Function Type	Function	Coefficients
Pure cosines function	$a \times \cos(b \times x)$	a=2, b=1/3
Pure cosines and exponential decaying function	$a \times \cos(b \times x) * e^{-c \times x}$	a=2, b=1/3, c=10

Table 5.1. Type and the coefficients of the functions used to test the numerical code

The two generated functions and their numerical code results are shown in Figure 5.12 and 5.13.

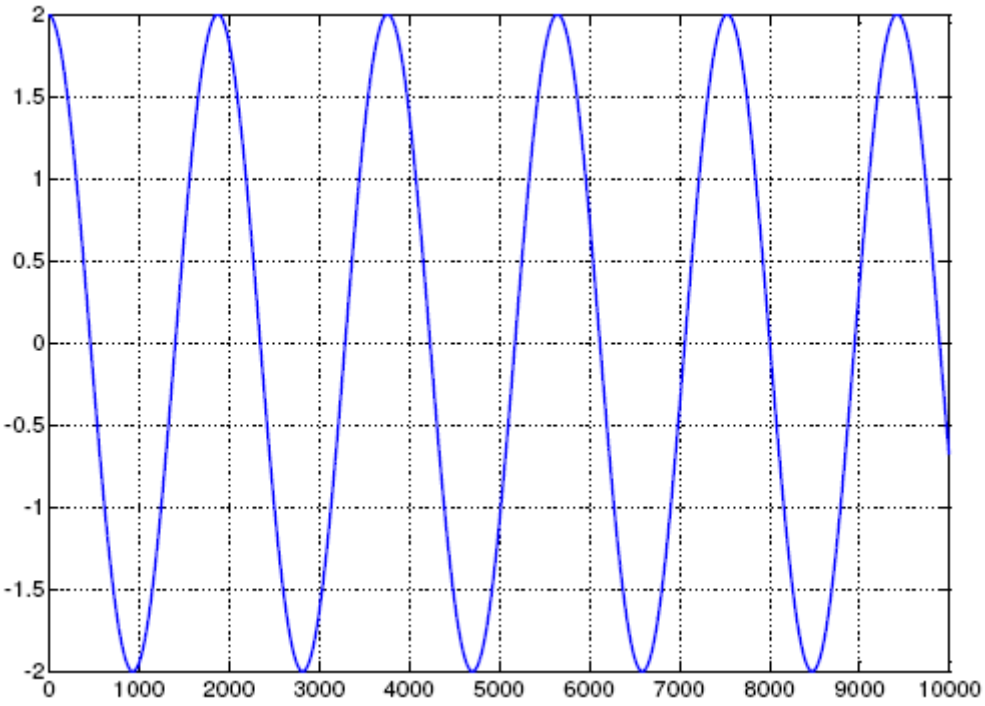

(a)

Figure 5.12. (a) Generated pure cosines function, (b) Measured distance

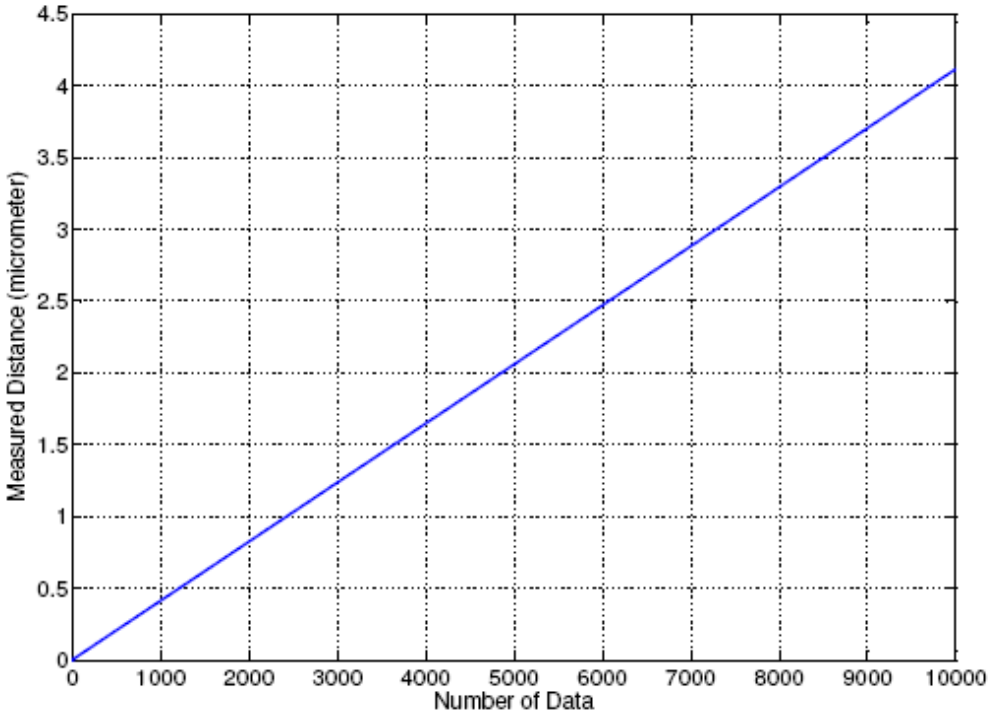

(b)

Figure 5.12. (a) Generated pure cosines function, (b) Measured distance (continued)

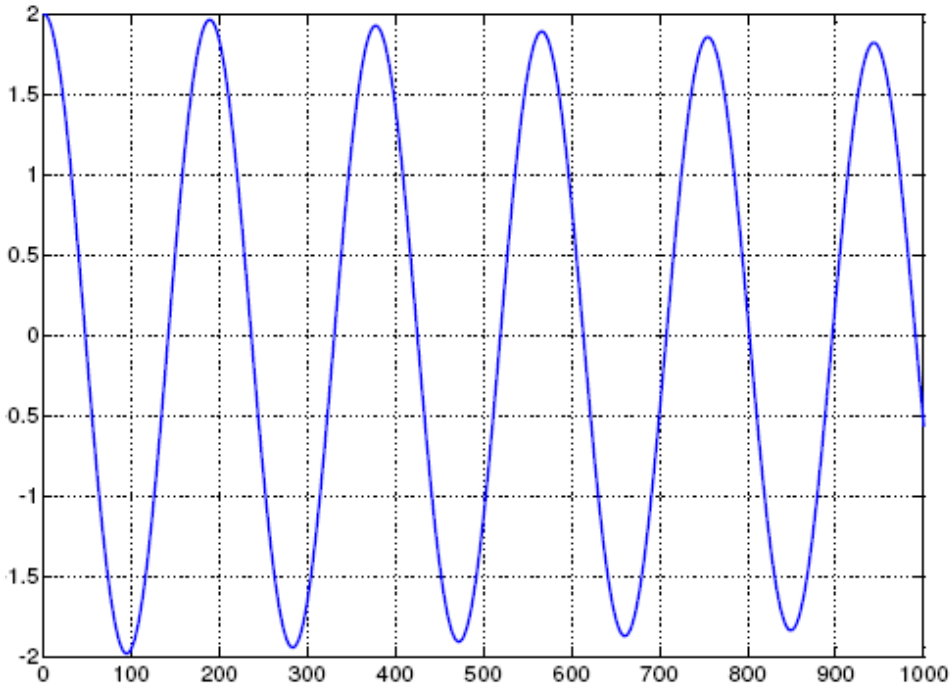

(a)

Figure 5.13. (a) Generated pure cosines and exponential decaying function, (b) Measured distance

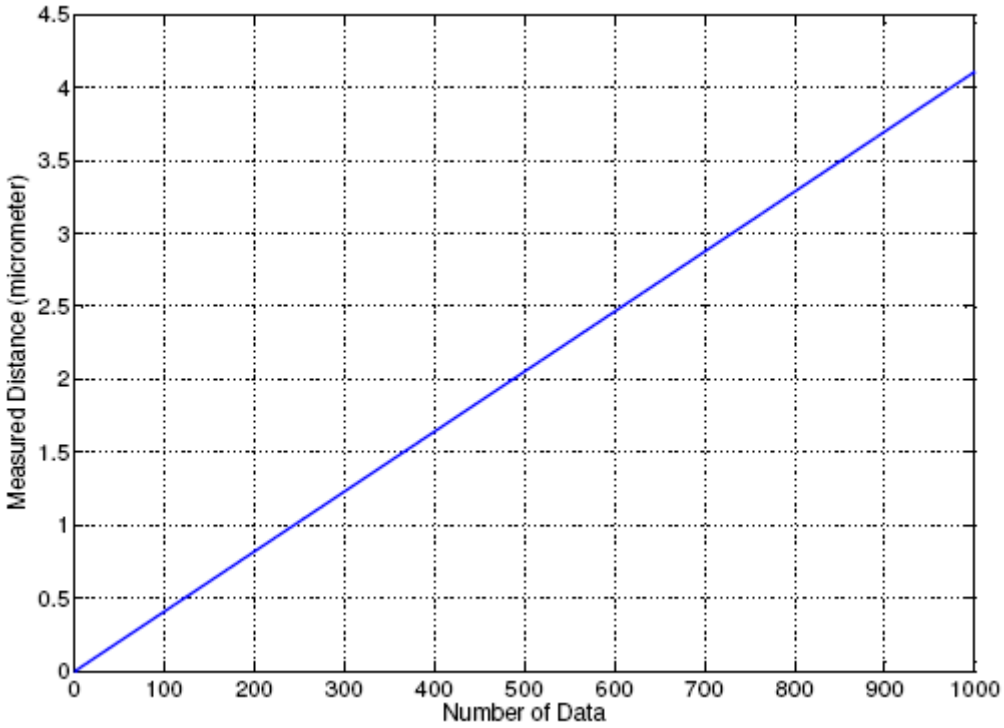

(b)

Figure 5.13. (a) Generated pure cosines and exponential decaying function, (b) Measured distance (continued)

The two different generated functions are executed with the numerical code and since the pure cosines function coefficients are the same in these two generated functions, measured distance values are the same for them. Therefore, the numerical procedure is applied to the filtered experimental data. First, the experimental data for probe 1 is executed. Since this probe detects the horizontal displacement of third plate, the result of this data gives the relative horizontal displacement during the experiments. The result of applying the numerical code to the probe 1 data is shown in Figure 5.14.

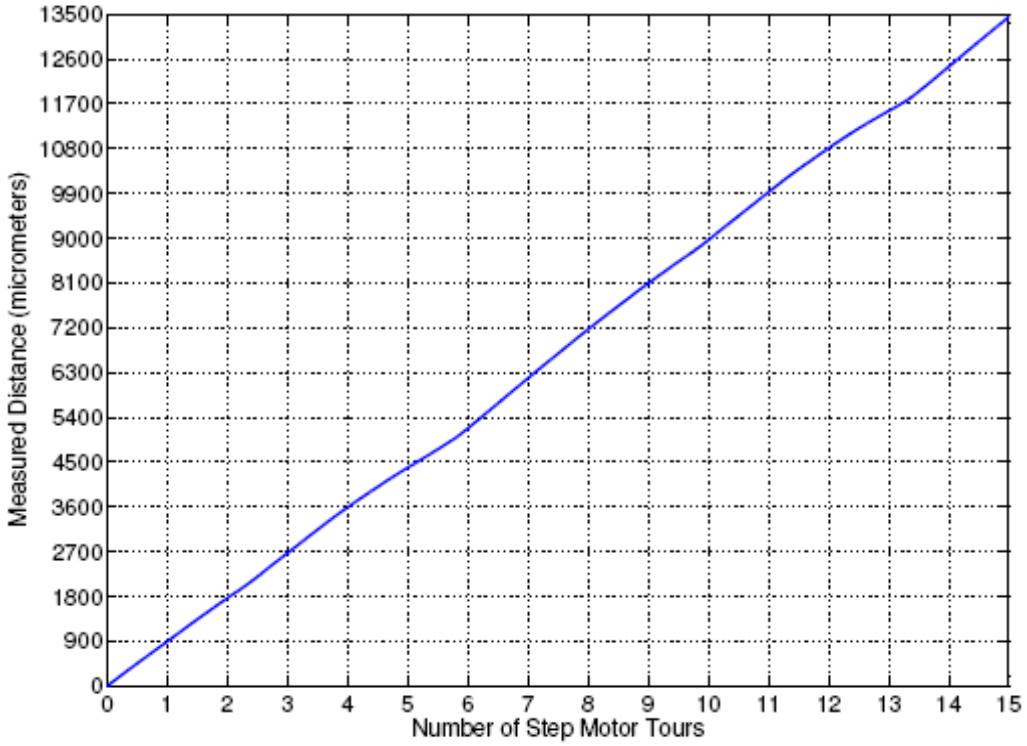

Figure 5.14. Measured distance of probe 1 data

From Figure 5.14, it is clearly seen that the relative horizontal displacement of the third plate is equal to 13500 μm during the 15 revolutions of step motor. After calculating the relative horizontal displacement of the third plate, the numerical code is applied to the experimental data of probe 3 shown in Figure 5.5.a. The result is shown in Figure 5.15.

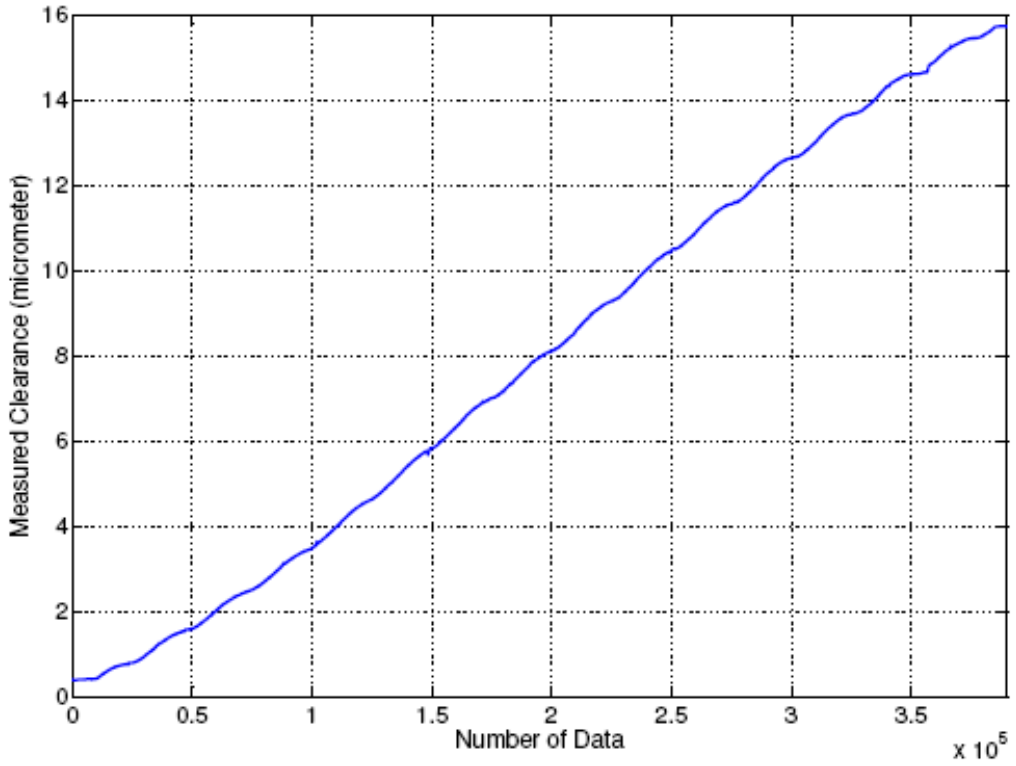

Figure 5.15. Measured clearance of filtered data

Since the filtered data includes some noisy parts at the beginning and the end of the experiments, these noisy parts should be excluded. The duration of the experiments should be determined to exclude the noisy parts at the beginning and at the end of the experiments. Since the horizontal motion is generated by the step motor, the frequency of the step motor gives the information about the duration of the experiments. From Figure 5.3, the average frequency of the step motor is 994.2 Hz. It means that 994.2 pulses are sent from the step motor driver in each second. Furthermore, the step motor driver sends 5000 pulses in each revolution of the step motor. Therefore, the duration of the step motor can be calculated as;

$$\text{Duration of the one revolution of the step motor} = \frac{5000}{994.2} = 5.0292\ \text{s}$$

Since the step turns 15 revolution during the experiments, the duration of the experiments is equal to:

$$\text{Duration of the experiments} = 5.0292 * 15 = 75.438 \text{ s}$$

Finally, the sampling rate of the data acquisition is equal to 5000 samples / second and the total data belong to the experiments is equal to:

$$\text{Total number of experimental data} = 75.438 * 5000 = 377190 \text{ samples}$$

In order to exclude the noisy part at the beginning, zooming action is performed in the rough data. Then, the end of the noisy part at the beginning is determined manually. This process is shown in Figure 5.16.

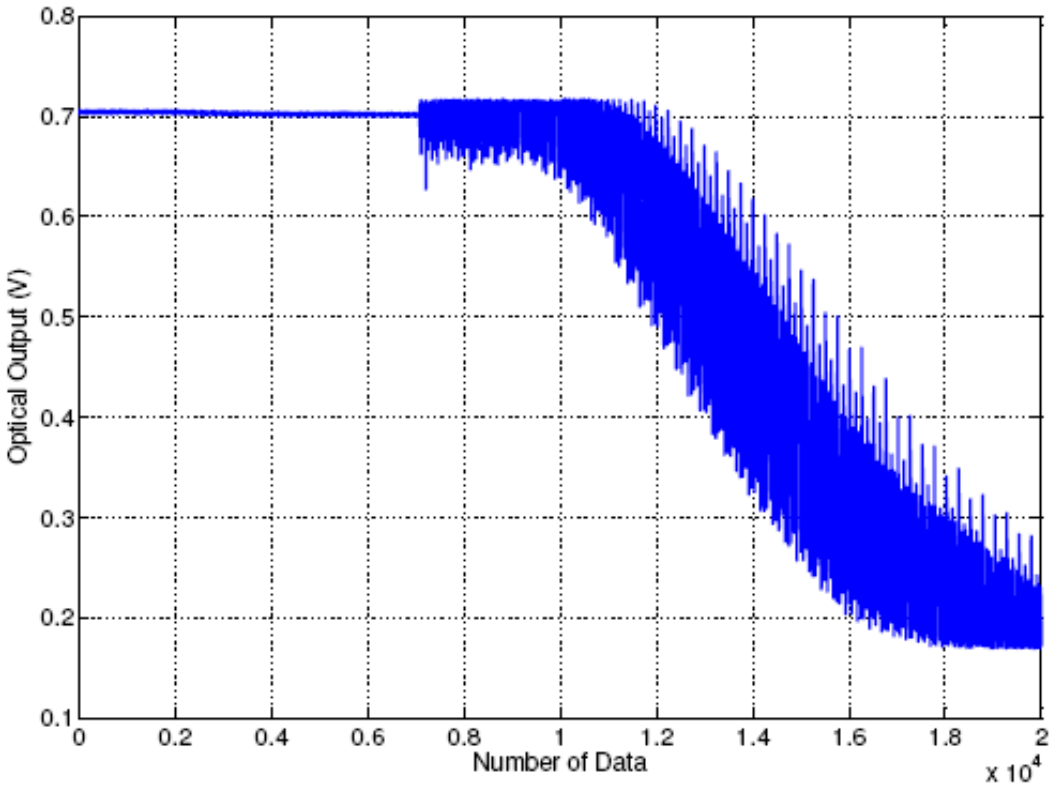

Figure 5.16. Noisy part exclusion at the beginning of rough data

The number of the data points is found as 7075. Then, the total number of the data points is added to that number and the last data number is found as 384265. Therefore, the noisy part is excluded from the measured clearance and the data in the range of 7075 and 384265 is taken to the further calculations. Since the horizontal displacement in each experiment is calculated by the probe 1 data analysis, the new measured clearance versus relative horizontal displacement curve can be plotted and it is shown in Figure 5.17.

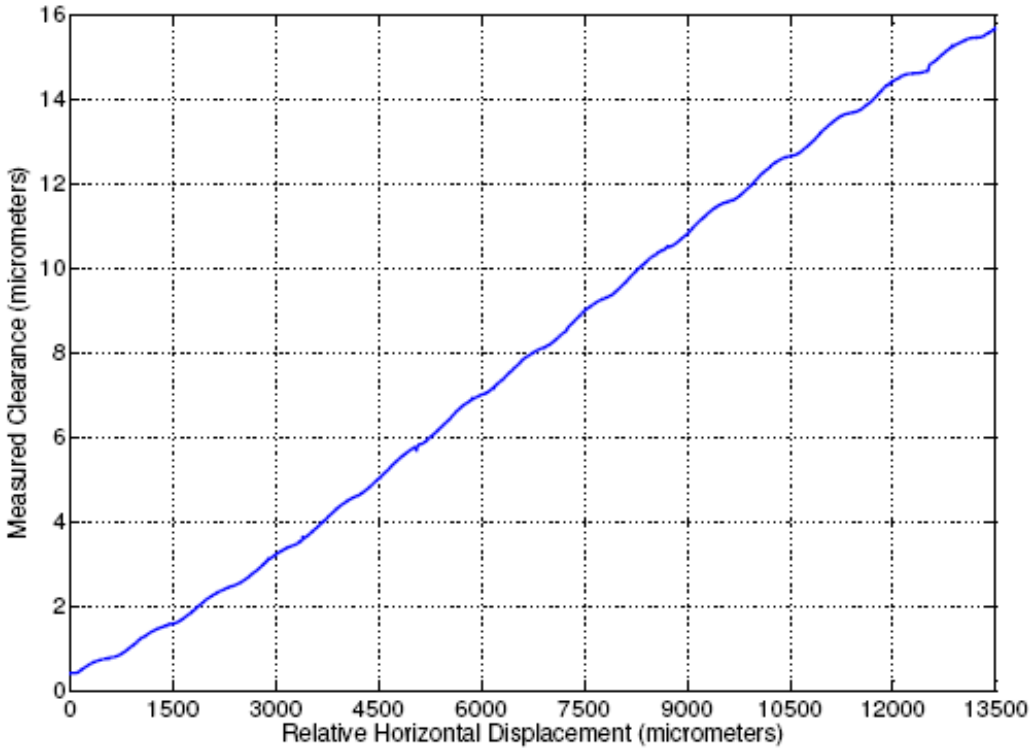

Figure 5.17. New measured clearance vs. relative horizontal displacement plot

After obtaining the new measured clearance vs. relative horizontal displacement curve, the Fourier transform of the new measured clearance is taken to see the effect of the conversion of the optical output into the measured clearance in frequency domain. The Fourier transform of the new measured clearance is shown in Figure 5.18.

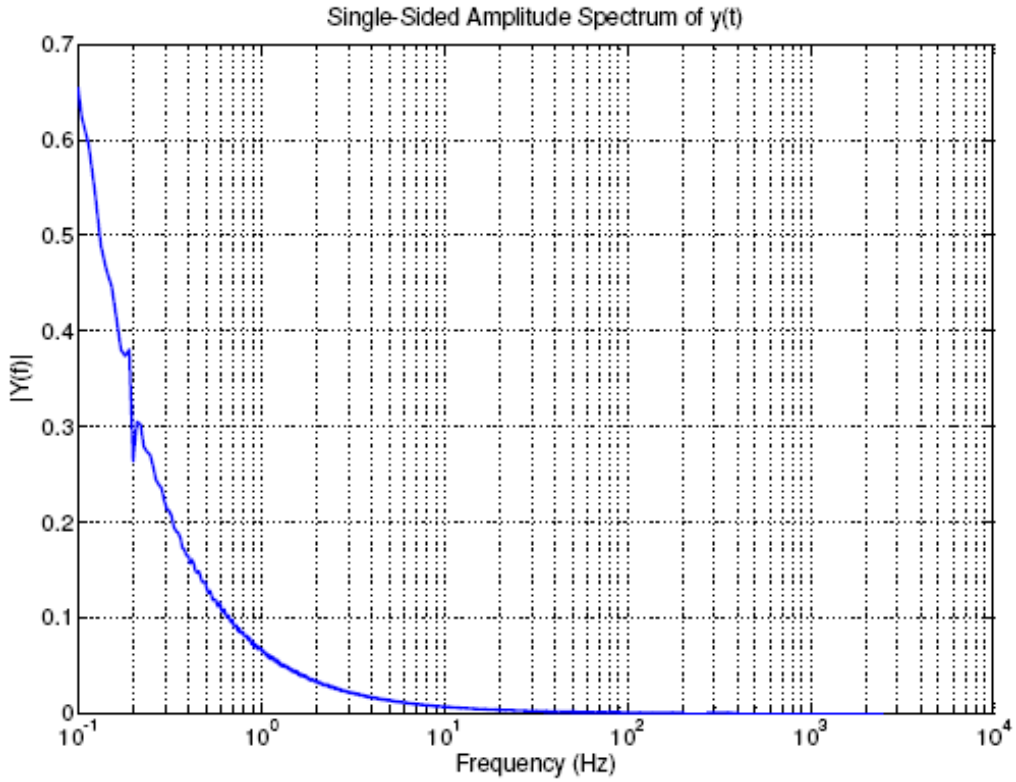

Figure 5.18. FFT of new measured clearance

It is seen from Figure 5.18 that the optical frequency of the data is diminished after the numerical code is applied to the optical output. It shows that the conversion of the optical output to the measured clearance is successful.

5.3 Linear Curve Fit

Although the measured clearance is expected to be a straight line, it is obvious that there is a deviation of measured clearance from the straight line and it can be seen in Figure 5.17. In order to observe the deviation from the straight line, a linear curve fit is applied to the measured clearance. The linear curve fit is shown in Figure 5.19.

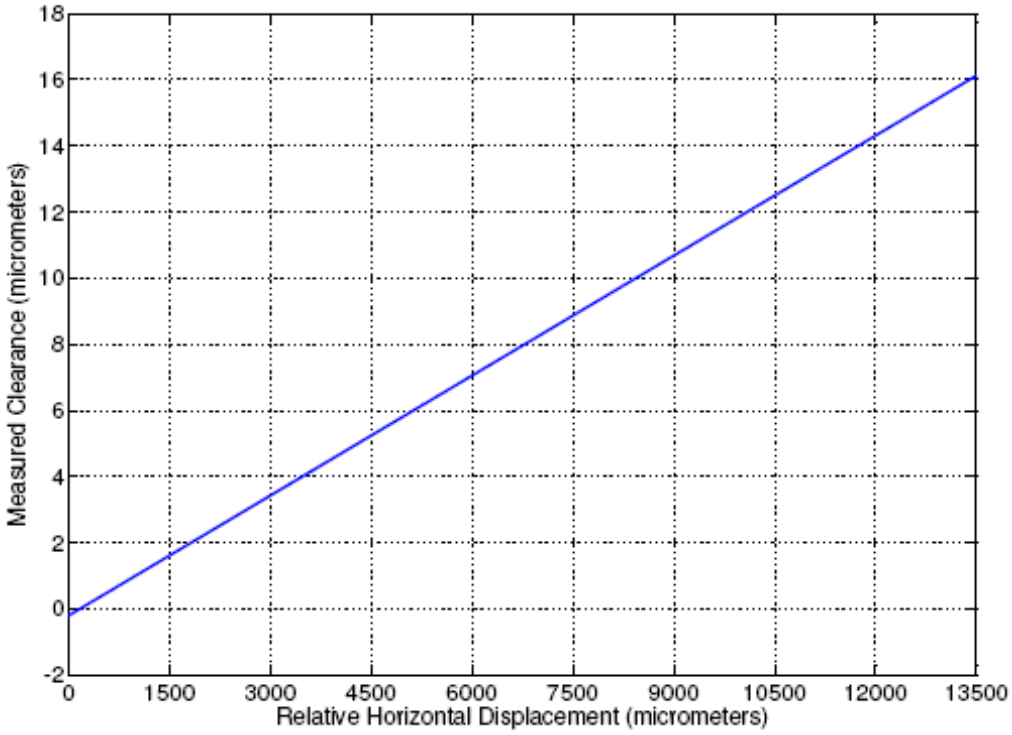

Figure 5.19. Linear curve fit to the new measure clearance

After obtaining the linear curve fit of the new measured clearance, new clearance is subtracted from the linear curve fit to obtain the deviation curve. The deviation curve is shown in Figure 5.20.

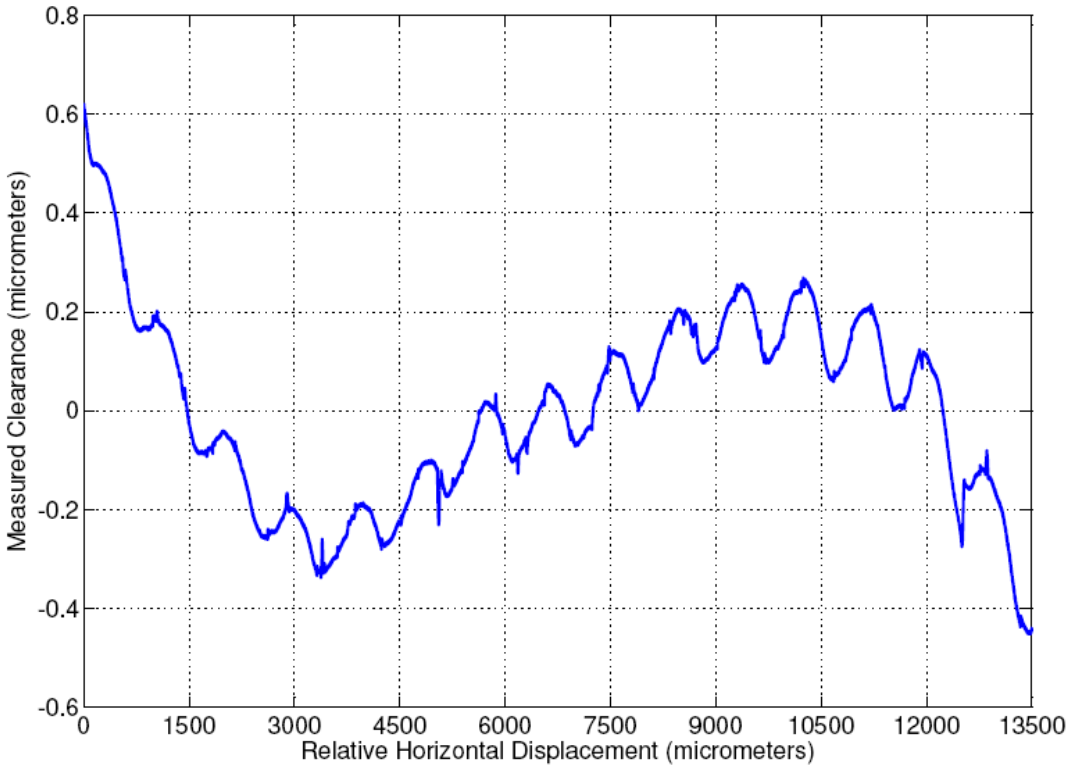

Figure 5.20. Deviation of new measured clearance from the linear curve fit

In the Figure 5.20, there are basically two different trends. One trend is the non-periodic trend and it firstly has a decreasing trend and then it starts to increase and finally it starts to decrease. Second trend is a periodic trend and the number of cycles of this trend is 15 during the whole experiment. In other words, the frequency of this trend should be approximately 0.2 Hz. In order to interpret Figure 5.20, Fourier transform of the deviation is taken and it is shown in Figure 5.21.

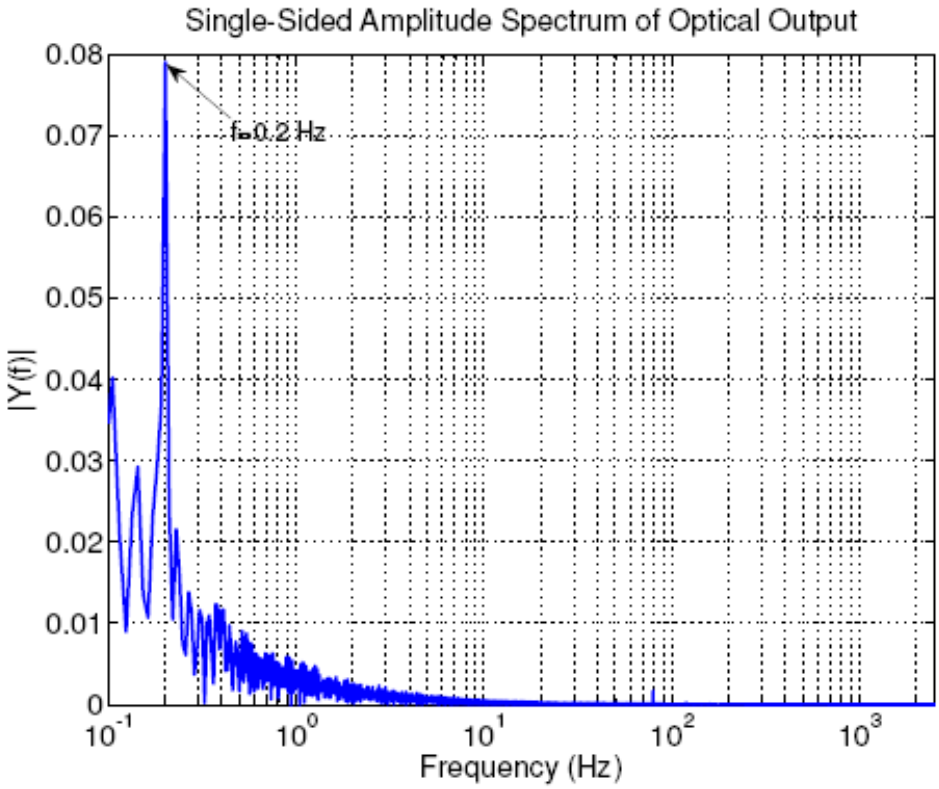

Figure 5.21. Fourier transform of the deviation

5.4. 9th Order Polynomial and Sinusoidal Curve Fits

After taking the Fourier transform of the deviation of new measured clearance to the linear curve fit, it can be seen that there is periodic trend whose frequency is 0.2 Hz. This frequency belongs to a trend whose period is 5 seconds. In other words, this period is equal to the one revolution of the step motor. In order to investigate these two trends, two different curve fits are applied to the deviation curve. First curve fit is the 9th order polynomial curve fit to model the first trend. Second curve fit is a sinusoidal curve fit to model the second trend. 9th order polynomial curve fit is shown in Figure 5.22.

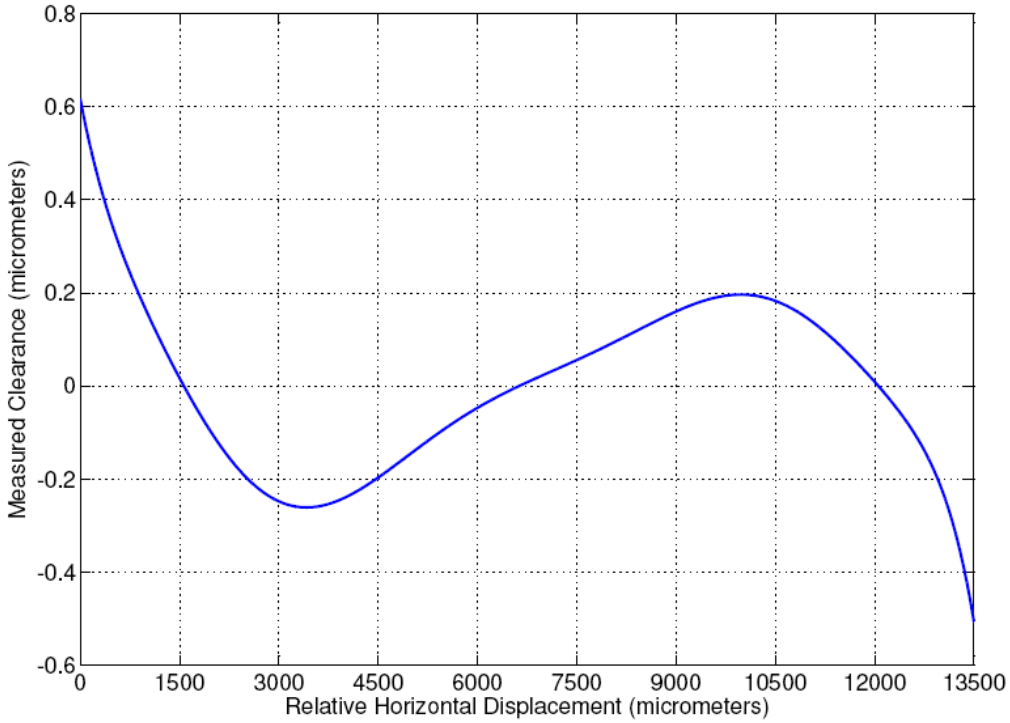

Figure 5.22. 9th order polynomial curve fit

After applying the 9th order polynomial curve fit to the deviation curve, sinusoidal curve fit is applied to the residuals. The sinusoidal curve fit is shown in Figure 5.23.

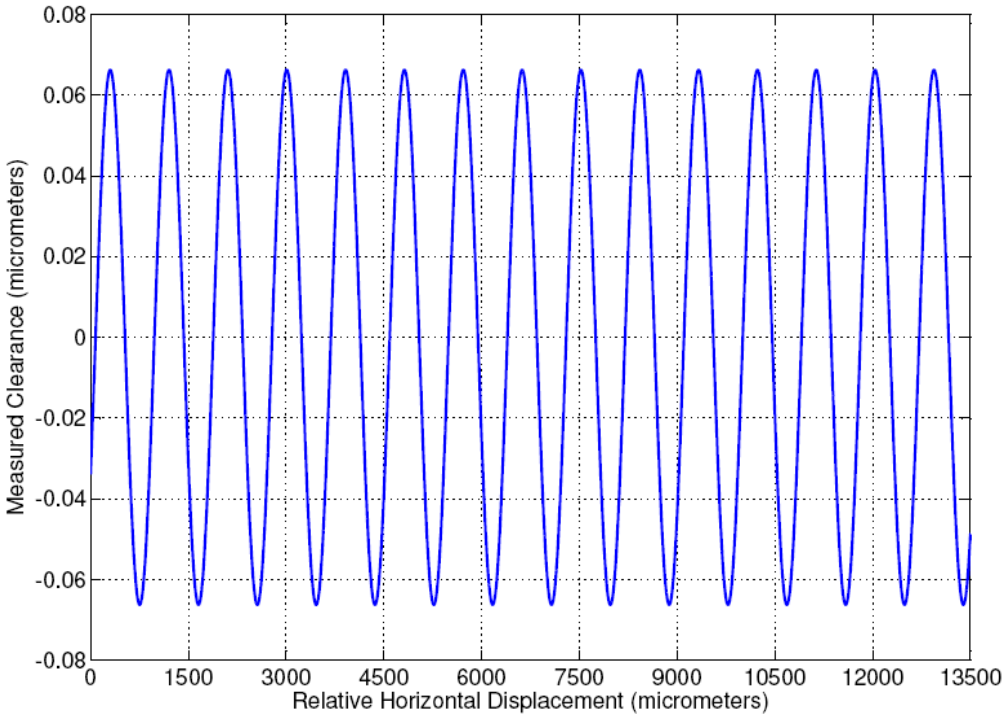

Figure 5.23. Sinusoidal curve fit

The summation of these two curve fits is performed and the result is shown in Figure 5.24.

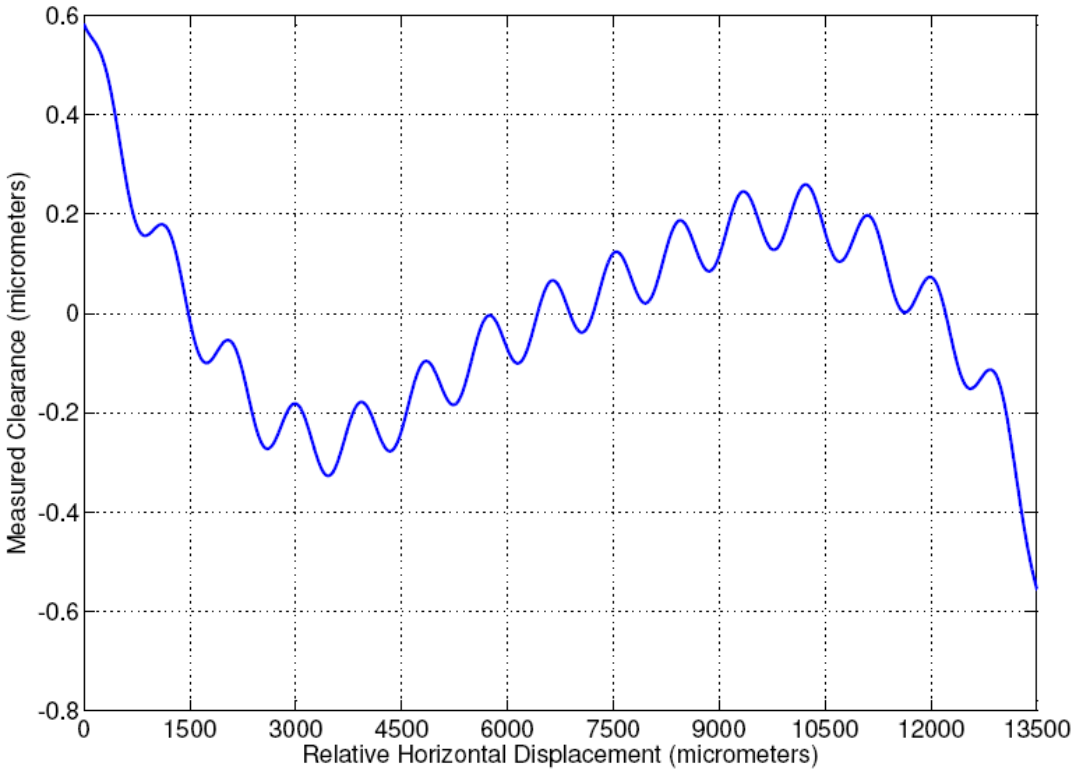

Figure 5.24. Summation of 9th order polynomial curve fit and sinusoidal curve fit

After obtaining the summation of the 9th order polynomial curve fit and sinusoidal curve fit, this summation curve is subtracted from the deviation curve to see effect of other dynamics in the experimental setup. The result is shown in Figure 5.25.

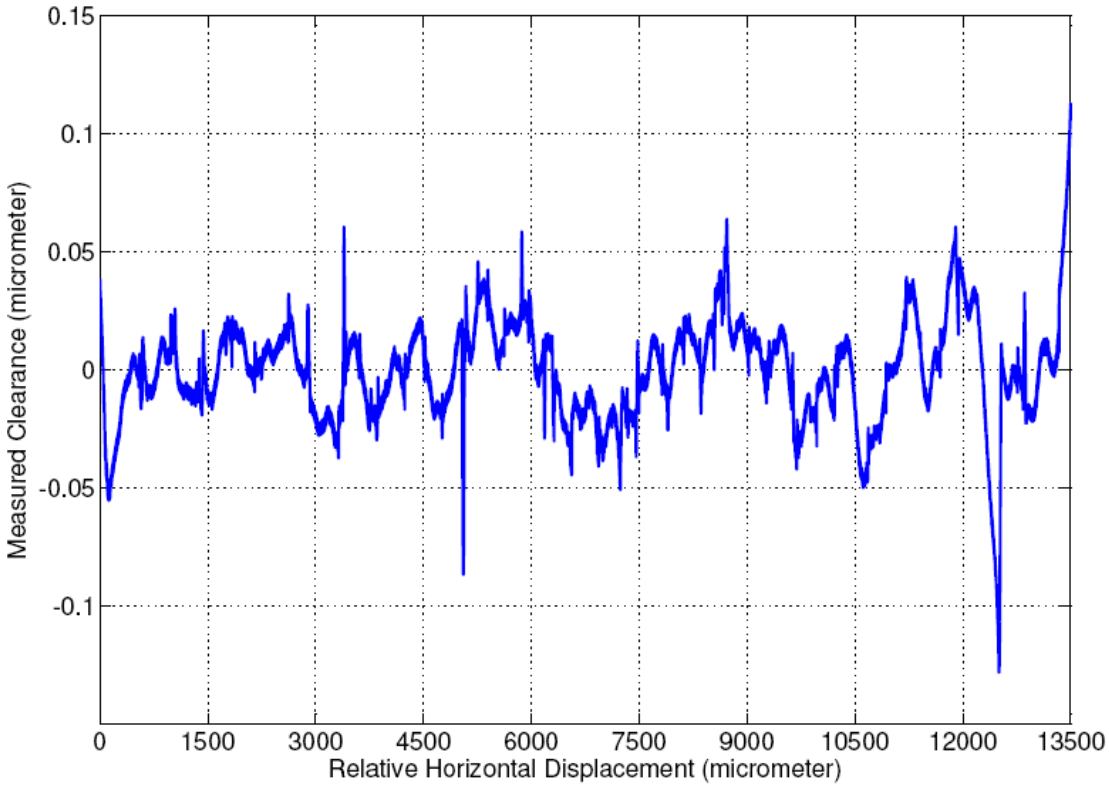

Figure 5.25. Residuals of the deviation curve

After obtaining the residuals curve, the R_a value of this curve is calculated in each experiment. Furthermore, the surface profile of the small cross section of the gold coated mirror is analyzed by the Atomic Force Microscope in Central Lab located at METU.

CHAPTER 6

UNCERTAINTY ANALYSIS

In this chapter, uncertainty analysis is explained. Since the experimental instrumentations have different levels of sensitivities, the uncertainties of the results obtained from the experiments should be determined.

Firstly, the equation used in the numerical code to determine the vertical distance of each data is shown in Equation 6.1.

$$I = A + B * \cos(\Delta\phi) \tag{6.1}$$

where $\Delta\phi = \frac{4*\pi}{\lambda} * x$ represents the phase difference of each data with respect to the nearest local maximum or minimum point. Therefore, Equation 6.1 can be rewritten with the definition of phase difference and it is shown in Equation 6.2.

$$I = A + B * \cos(\frac{4*\pi}{\lambda} * x) \tag{6.2}$$

In order to determine the uncertainty level in calculating the distance values, partial derivative of the photo-detector intensity, I, with respect to the distance values, x, should be determined. The resultant function of this partial derivative is shown in Equation 6.3.

$$\frac{\partial I}{\partial x} = -B * \frac{4*\pi}{\lambda} * \sin(\frac{4*\pi}{\lambda} * x) \tag{6.3}$$

From Equation 6.3, it is obvious that the partial derivative of the intensity with respect to the distance values depends on constant term $-B*\frac{4*\pi}{\lambda}$ and sinusoidal function $\sin(\frac{4*\pi}{\lambda}*x)$. However, the uncertainty level can be determined by leaving the ∂x term alone and this equation is shown in Equation 6.4.

$$\partial x = -\frac{\lambda}{4*\pi*B}*\frac{\partial I}{\sin(\frac{4*\pi}{\lambda}*x)} \tag{6.4}$$

This uncertainty equation is installed to the numerical code for the experimental data when Δh = 15 μm with air in the forward direction for fiber optic probe 3. The result is shown in Figure 6.1.

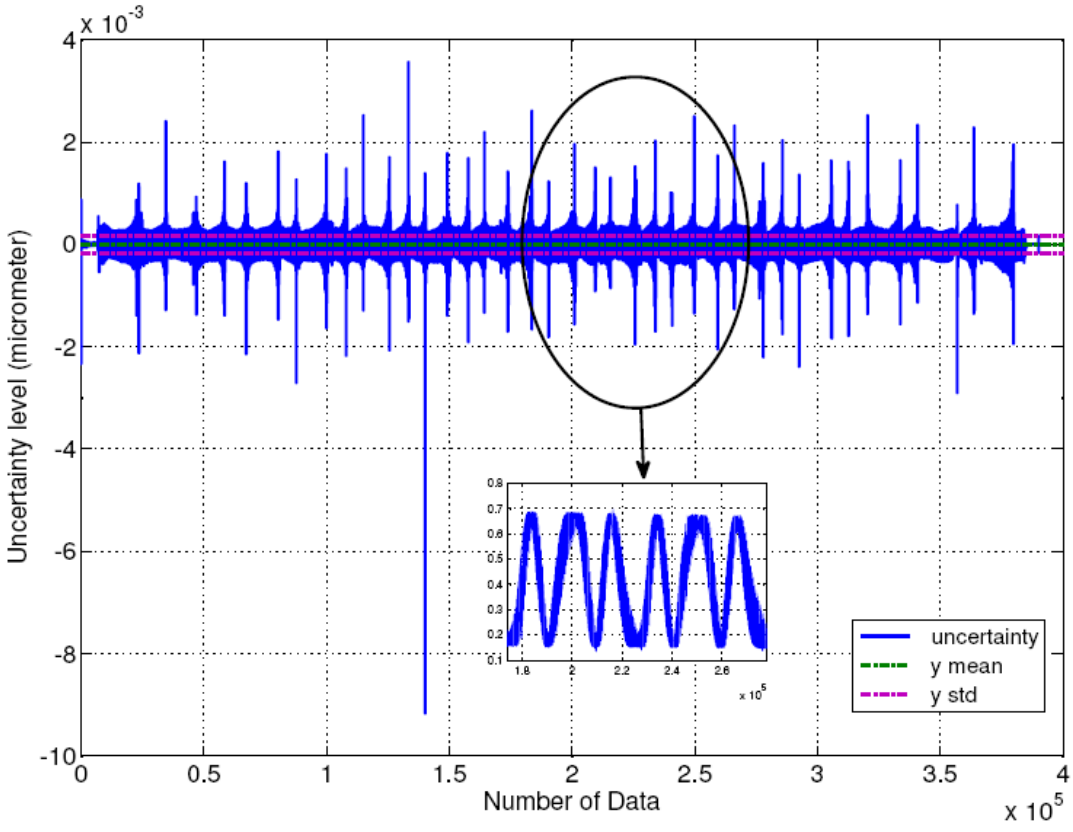

Figure 6.1. Uncertainty level

Statistical parameters regarding with the uncertainty level is shown in Table 6.1.

Minimum Value	-0.0091634 μm
Maximum Value	0.003559 μm
Mean Value	$4.2426*10^{-7}$ μm
Median Value	$1.0491*10^{-6}$ μm
Standard Deviation	0.00017761 μm
Range	0.012722 μm

Table 6.1. Statistical parameters of uncertainty

From Table 6.1, it can be seen that maximum uncertainty is 9 nm and the mean value is practically zero and standard deviation is equal to 0.18 nm. In Figure 6.1, there are some locations at which uncertainty values are maximum. In order to show the locations of these points, the rough data related with these points shown with a ellipse is also shown in Figure 6.1 with a smaller scale. As it can be seen from Figure 6.1 that maximum uncertainty values occurs at the neighborhood of the local maximum and the minimum points. This is due to the discontinuous behavior of the sinusoidal function exists in the denominator of the uncertainty level function in Eq. 6.4.

CHAPTER 7

RESULTS AND DISCUSSIONS

Set of experiments are conducted with different Δh values in the range of 1-50 μm. These experiments are performed within two different mediums which are air and lubricant in the forward and backward directions. The measured clearance versus relative horizontal displacement curves in the forward and backward directions for probe 3 in the air are shown in Figure 7.1.a and 7.1.b, respectively.

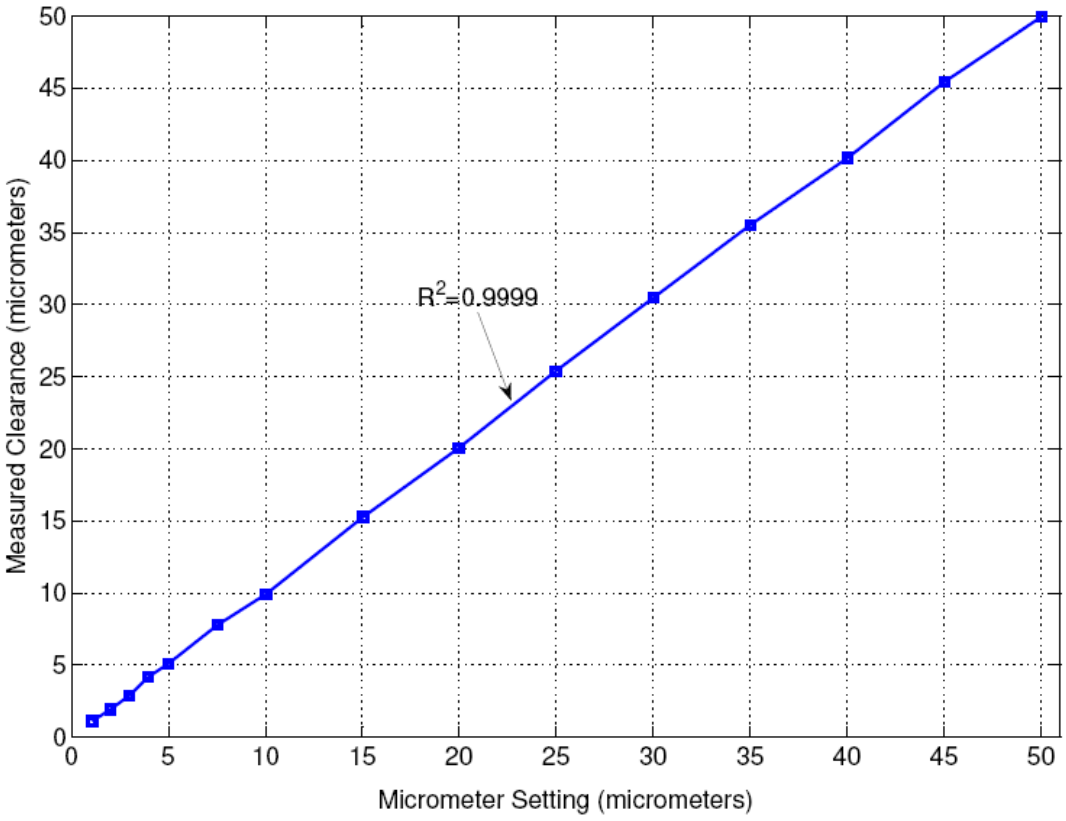

(a)

Figure 7.1. Measured distance vs. micrometer setting plot for probe 3 in air, (a) forward direction, (b) backward direction

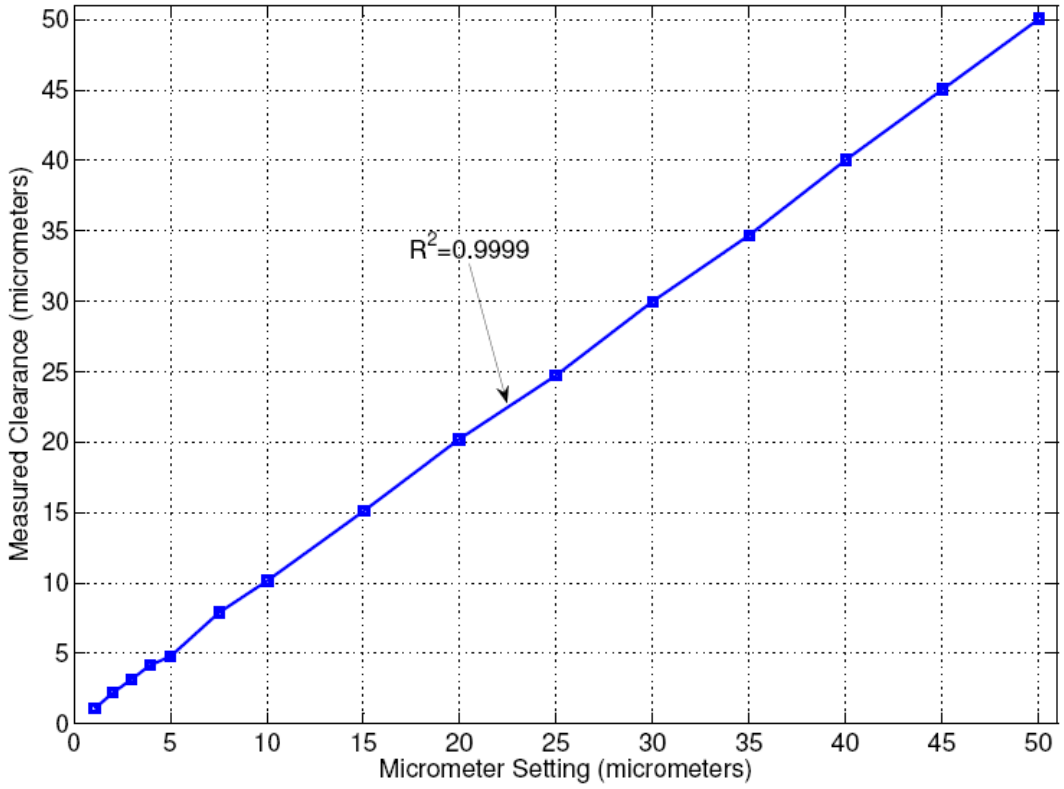

(b)

Figure 7.1. Measured distance vs. micrometer setting plot for probe 3 in air, (a) forward direction, (b) backward direction (continued)

The average deviation of the measured clearance values from the micrometer settings in the forward direction is 0.166 μm. The maximum deviation is 0.5 μm and this deviation occurs when $\Delta h = 35$ μm. The minimum deviation is 0.057 μm and occurs when $\Delta h = 1$ μm. The average deviation of the measured clearance values from the micrometer settings in the backward direction is 0.038 μm. The maximum deviation is 0.371 μm and this deviation occurs when $\Delta h = 7.5$ μm. The minimum deviation is 0.004 μm and occurs when $\Delta h = 35$ μm.

The measured clearance versus relative horizontal displacement curves in the forward and backward directions for probe 5 in the air are shown in Figure 7.2.a and 7.2.b, respectively.

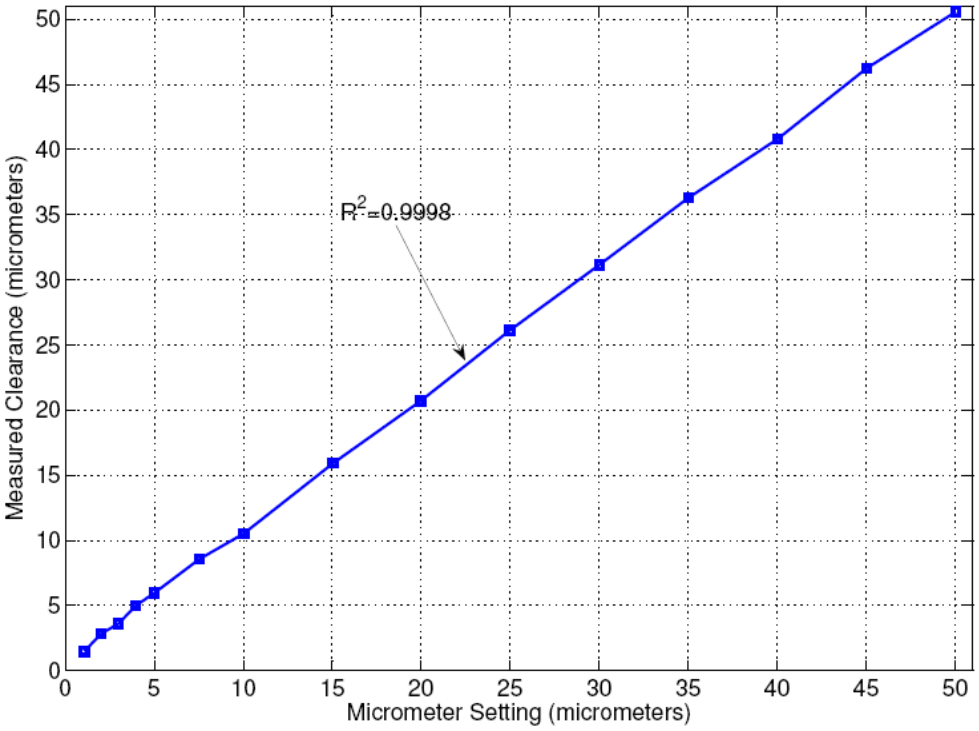

(a)

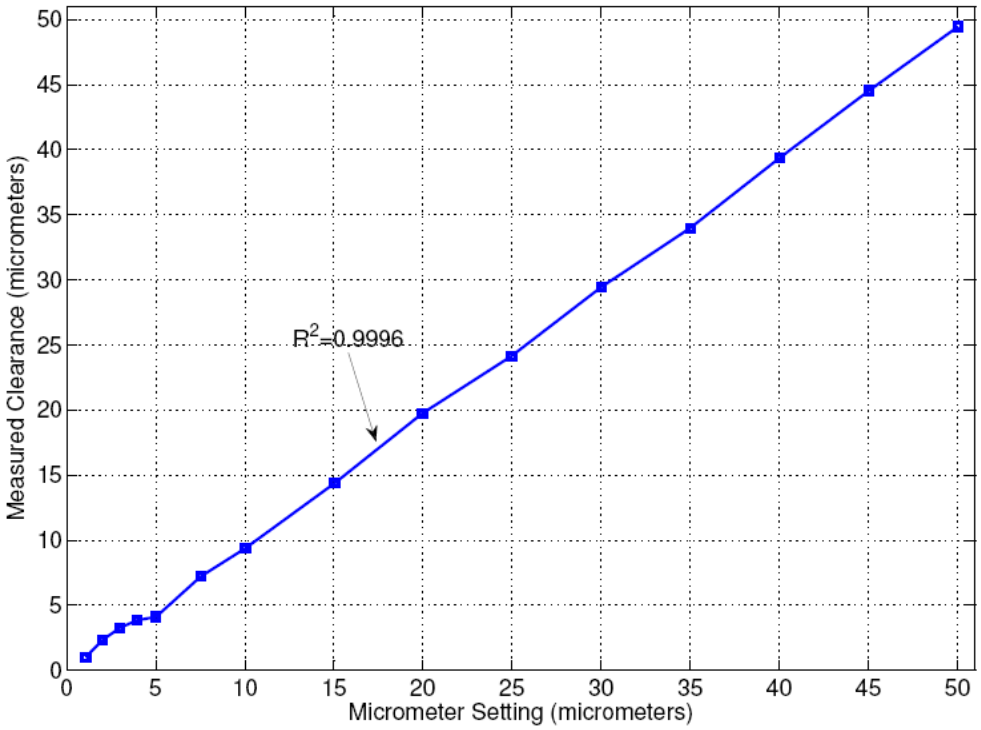

(b)

Figure 7.2. (a) Measured distance vs. micrometer setting plot for probe 5 in air, (a) forward direction, (b) backward direction

The average deviation of the measured clearance values from the micrometer settings in the forward direction is 0.872 μm. The maximum deviation is 1.2 μm and this deviation occurs when $\Delta h = 45$ μm. The minimum deviation is 0.2 μm and occurs when $\Delta h = 1$ μm. The average deviation of the measured clearance values from the micrometer settings in the backward direction is 0.461 μm. The maximum deviation is 1.021 μm and this deviation occurs when $\Delta h = 35$ μm. The minimum deviation is 0.059 μm and occurs when $\Delta h = 1$ μm.

The measured clearance versus relative horizontal displacement curves in the forward and backward directions for probe 3 in the lubricant are shown in Figure 7.3.a and 7.3.b, respectively.

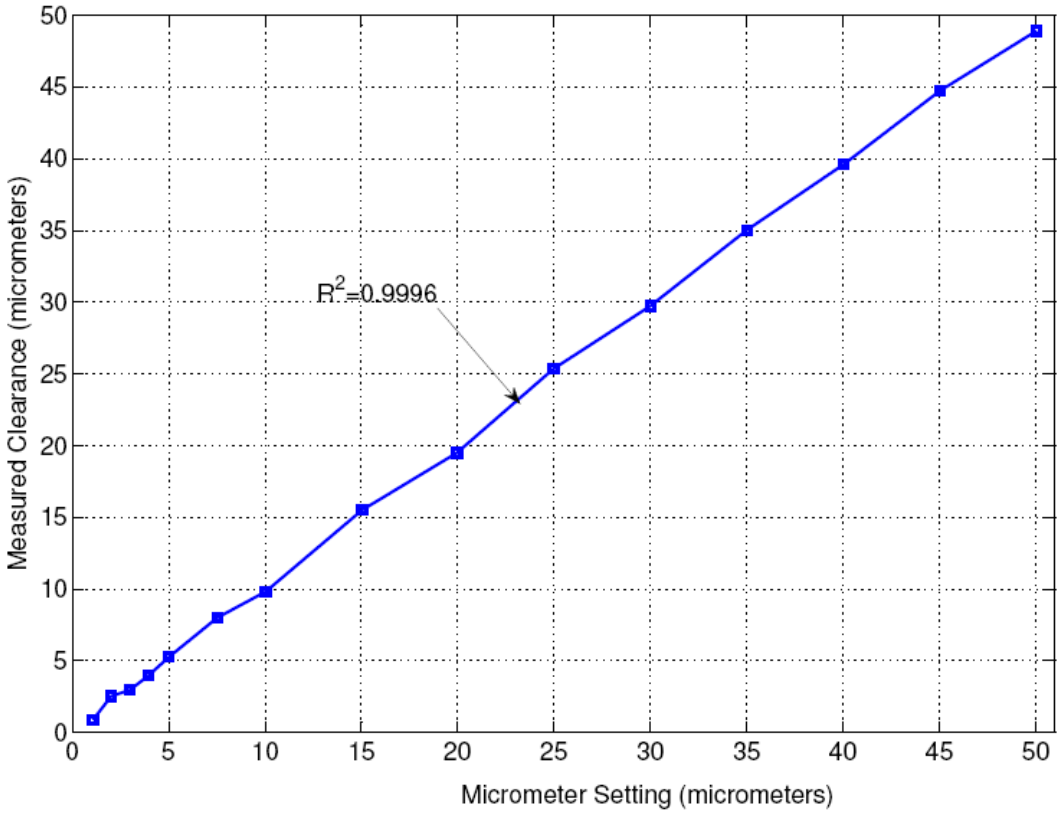

(a)

Figure 7.3. . Measured distance vs. micrometer setting plot for probe 3 in lubricant, (a) forward direction, (b) backward direction

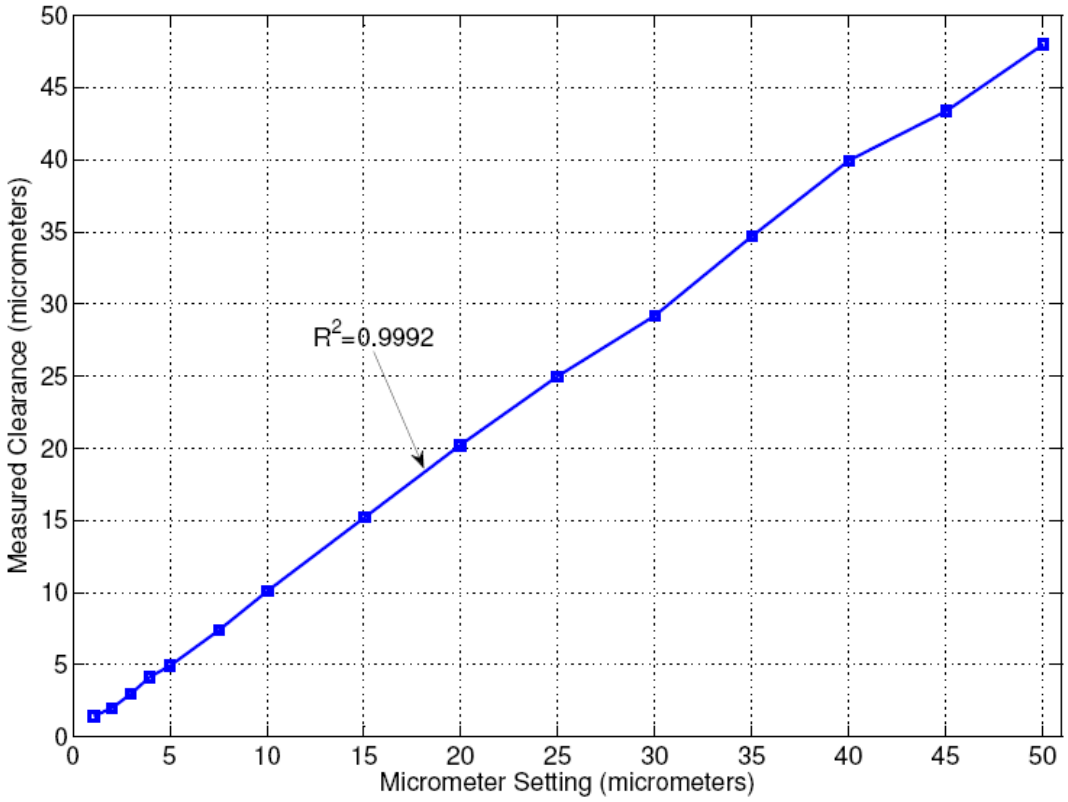

(b)

Figure 7.3. . Measured distance vs. micrometer setting plot for probe 3 in lubricant, (a) forward direction, (b) backward direction (continued)

The average deviation of the measured clearance values from the micrometer settings in the forward direction is 0.087 μm. The maximum deviation is 1.137 μm and this deviation occurs when $\Delta h = 50$ μm. The minimum deviation is 0.015 μm and occurs when $\Delta h = 35$ μm. The average deviation of the measured clearance values from the micrometer settings in the backward direction is 0.275 μm. The maximum deviation is 2.051 μm and this deviation occurs when $\Delta h = 50$ μm. The minimum deviation is 0.008 μm and occurs when $\Delta h = 25$ μm.

The measured clearance versus relative horizontal displacement curves in the forward and backward directions for probe 5 in the lubricant are shown in Figure 7.4.a and 7.4.b, respectively.

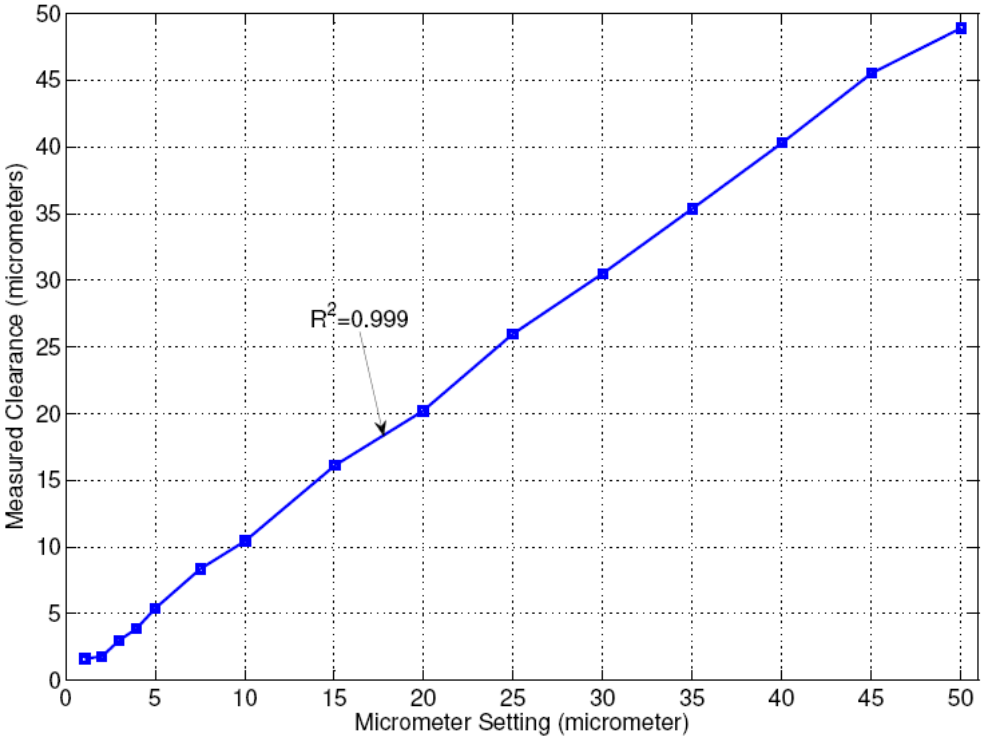

(a)

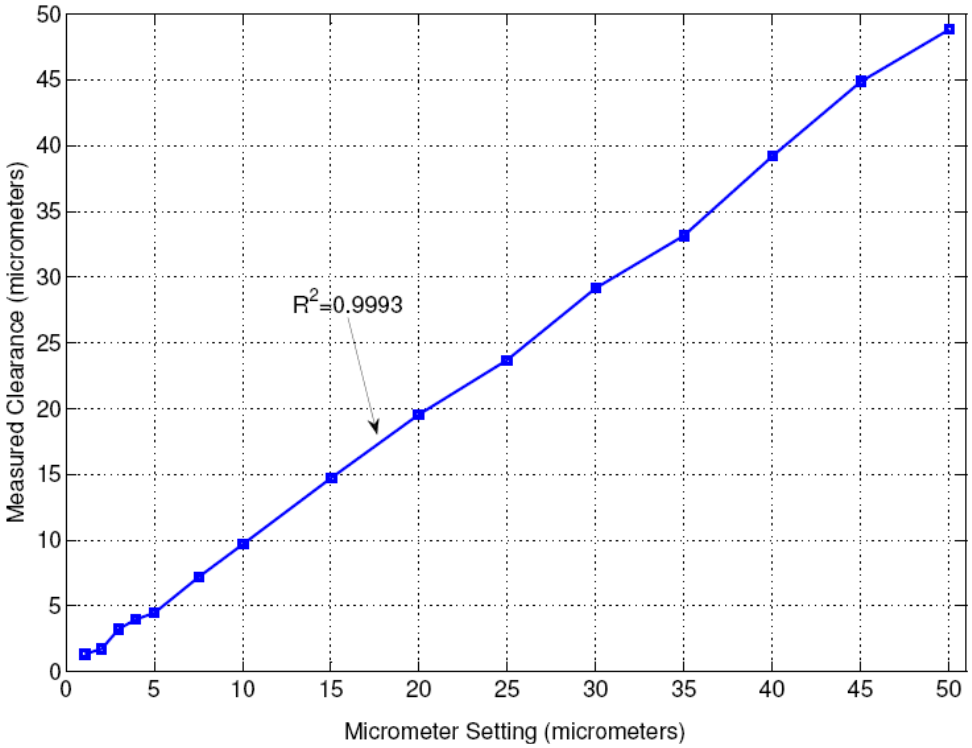

(b)

Figure 7.4. Measured distance vs. micrometer setting plot for probe 5 in lubricant, (a) forward direction, (b) backward direction

The average deviation of the measured clearance values from the micrometer settings in the forward direction is 0.383 μm. The maximum deviation is 1.137 μm and this deviation occurs when $\Delta h = 50$ μm. The minimum deviation is 0.010 μm and occurs when $\Delta h = 3$ μm. The average deviation of the measured clearance values from the micrometer settings in the backward direction is 0.590 μm. The maximum deviation is 1.285 μm and this deviation occurs when $\Delta h = 25$ μm. The minimum deviation is 0.012 μm and occurs when $\Delta h = 4$ μm.

From Figures 7.1, 7.2, 7.3 and 7.4, it is concluded that the accuracy of the measured clearance values is better in the experiments with air than the experiments with lubricant. The reason of that difference in accuracy is the visibility value differences in the experiments with air and lubricant. Optical outputs with air and with the lubricant for the probe 3 in the forward direction when $\Delta h = 15$ μm are shown in Figure 7.5.a and 7.5.b, respectively.

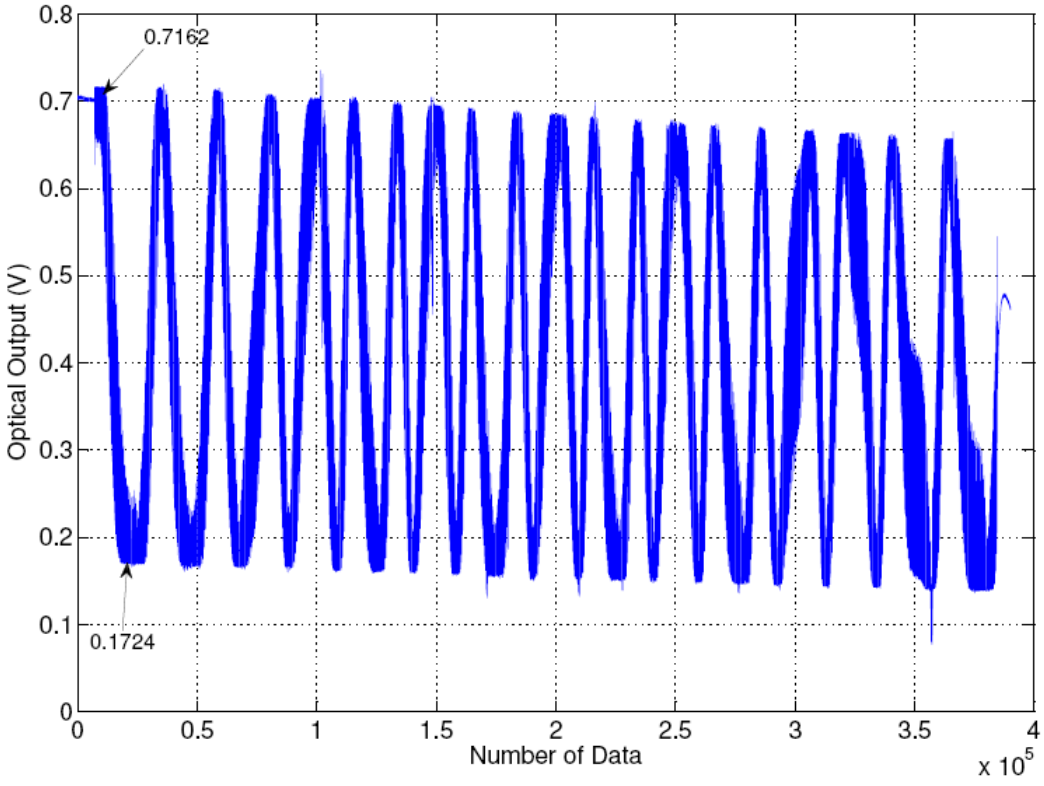

(a)

Figure 7.5. Optical output, (a) Air, (b) Lubricant

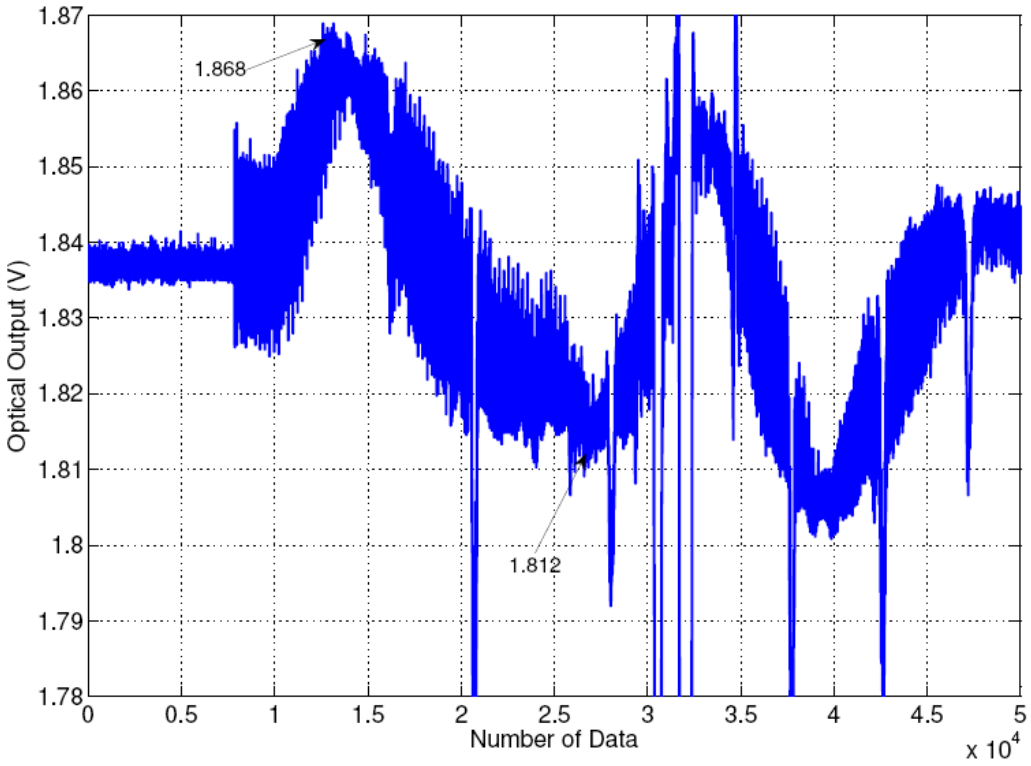

(b)

Figure 7.5. Optical output, (a) Air, (b) Lubricant (continued)

It is seen from Figure 7.5 that the visibility of the experimental data with air is 0.612, the visibility of the experimental data with lubricant is 0.015 with using the first local maximum and minimum intensities of the optical output. In other words, the visibility with air is 40 times of the visibility with lubricant. Therefore, the data analysis procedure of the experimental data with lubricant needs more attention than the one with air.

Another important result in this study is the deviation of the measured clearance values from the linear curve fit curves which is explained in the Chapter 5. This deviation curve includes the step motor and the lateral motion carriage induced vertical motion. In order to verify this claim, the deviation curves in each experiment in the forward and backward directions and for air and lubricant are obtained and compared with each other. Since 15 experiments are conducted in one direction for each probe, the average of these 15 deviation curves is obtained and then the standard deviations of each experimental deviation curve from this average

curve are calculated. The average deviation curve and the differences of each experiment from this average for the probe 3 in the forward direction with air are shown in Figure 7.6.a and 7.6.b.

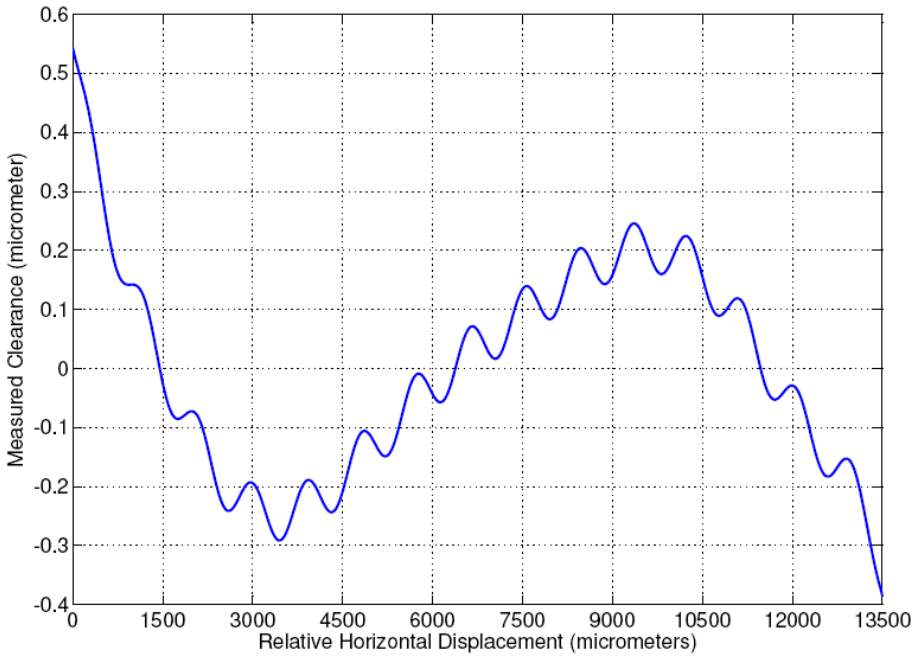

(a)

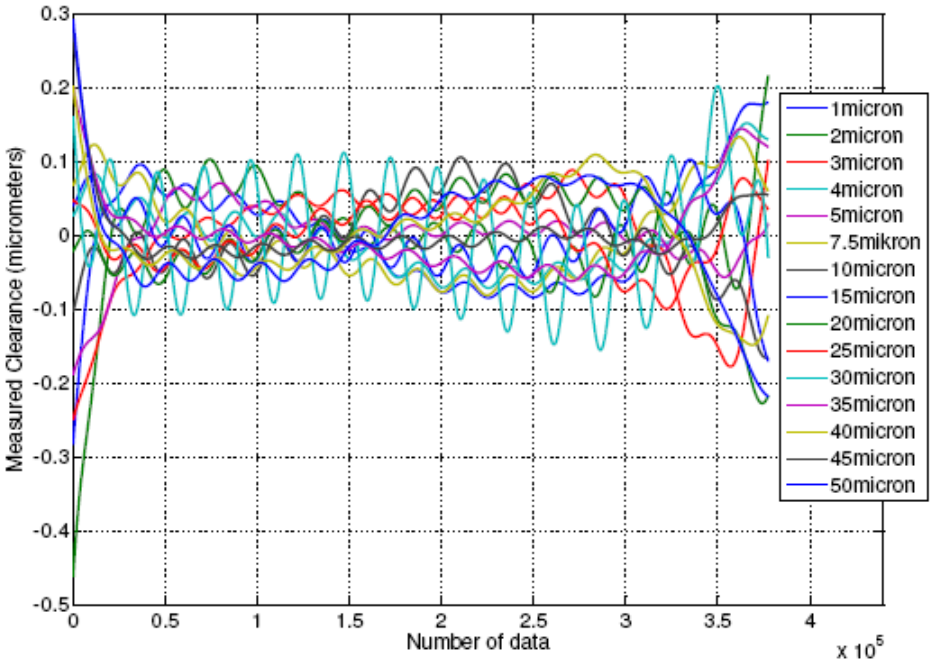

(b)

Figure 7.6. (a) Average step motor and lateral motion carriage effect, (b) the differences from average effect for probe 3 in the forward direction in air

The standard deviations of the difference between each experiment and the average one are tabulated in Table 7.1.

Table 7.1. Standard deviations of the differences from the average deviation curve for probe 3 in the forward direction with air

Δh (μm)	Standard deviation of the difference (μm)
1	0.07311
2	0.07564
3	0.07414
4	0.05305
5	0.04273
7.5	0.06115
10	0.05489
15	0.04274
20	0.06342
25	0.04026
30	0.07737
35	0.05329
40	0.06313
45	0.03663
50	0.07234

It is statistically found from Table 7.1 that the average deviation curve of probe 3 represents all experiments in the forward direction in the air with error of 58.93 ± 13.96 nanometers.

Then, average deviation curve is used to correct the measured clearance versus values calculated in each experiment to obtain more precise measured clearance values. To prove this statement, the average deviation curve is subtracted from each experiment's measured clearance values and then the linearity of the new and

previous measured clearance values. The results of the linearity of the new and previous measured clearance values for the data of probe 3 in the forward direction with air is shown in Table 7.2.

Table 7.2 Comparison of the linearity of the measured clearance previous and new values for probe 3 in the forward direction in air

Δh (μm)	R^2 (previous)	R^2 (new)
1	0.9169	0.9719
2	0.9615	0.9848
3	0.9675	0.9936
4	0.9865	0.9983
5	0.9912	0.9990
7.5	0.9947	0.9994
10	0.9956	0.9996
15	0.9983	0.9999
20	0.9987	0.9999
25	0.9994	1
30	0.9996	1
35	0.9997	1
40	0.9996	1
45	0.9998	1
50	0.9997	1

It is seen that maximum increase in the linearity occurs at $\Delta h = 1$ μm and the R^2 values are equal to one in whole experiments after $\Delta h = 20$ μm. Therefore, the measured clearance values can be corrected by determining effects of the step motor and the lateral motion carriage.

The same procedure is applied to the experimental data of probe 5 in the forward direction in air. The average deviation curve and the differences of each experiment

from this average for the probe 5 in the forward direction with air are shown in Figure 7.7.a and 7.7.b.

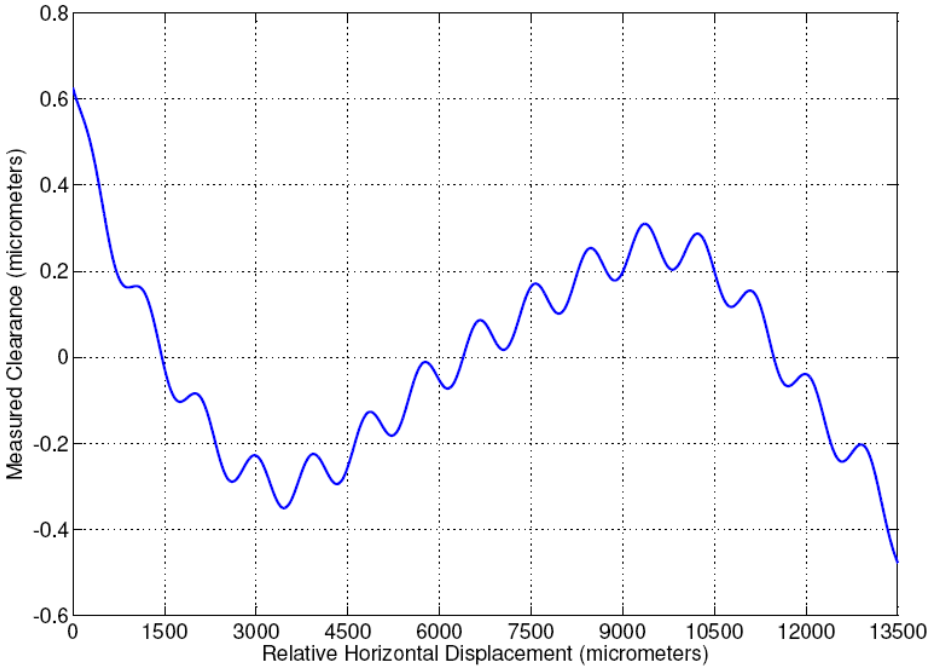

(a)

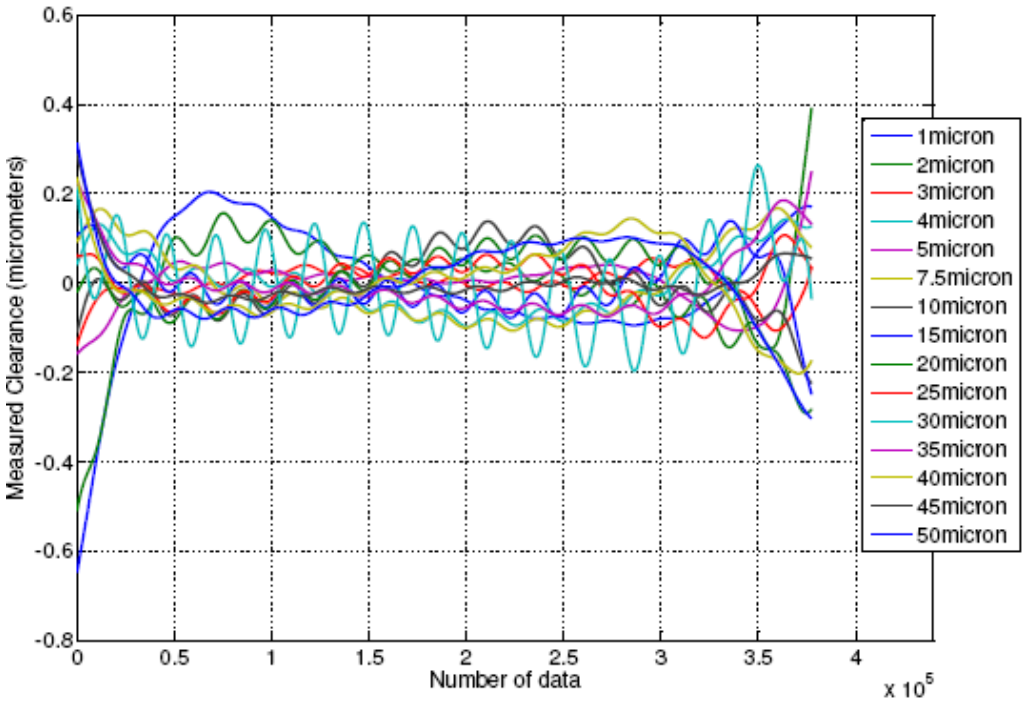

(b)

Figure 7.7. (a) Average step motor and lateral motion carriage effect, (b) the differences from average effect for probe 5 in the forward direction in air

The standard deviations of the difference between each experiment and the average one are tabulated in Table 7.3.

Table 7.3. Standard deviations of the differences from the average deviation curve for probe 5 in the forward direction with air

Δh (μm)	Standard deviation of the difference (μm)
1	0.1386
2	0.1162
3	0.03377
4	0.06733
5	0.05264
7.5	0.08235
10	0.06772
15	0.05984
20	0.07978
25	0.05134
30	0.09908
35	0.06806
40	0.08279
45	0.04391
50	0.09275

It is statistically found from Table 7.3 that the average deviation curve of probe 5 represents all experiments in the forward direction in the air with error of 75.74 ± 27.88 nanometers.

The results of the linearity of the new and previous measured clearance values for the data of probe 5 in the forward direction with air is shown in Table 7.4.

Table 7.4 Comparison of the linearity of the measured clearance previous and new values for probe 5 in the forward direction in air

Δh (μm)	R^2 (previous)	R^2 (new)
1	0.9777	0.9663
2	0.9654	0.9816
3	0.9721	0.9984
4	0.9846	0.9982
5	0.9888	0.9987
7.5	0.9934	0.9990
10	0.9941	0.9995
15	0.9977	0.9998
20	0.9981	0.9998
25	0.9992	0.9999
30	0.9995	1
35	0.9996	1
40	0.9994	1
45	0.9997	1
50	0.9996	1

It is seen that maximum increase in the linearity occurs at $\Delta h = 1$ μm and the R^2 values are equal to one in whole experiments after $\Delta h = 20$ μm. Therefore, the measured clearance values can be corrected by determining effects of the step motor and the lateral motion carriage.

Since the probes 3 and 5 are fixed to the third plate and third plate is moving in the lateral direction, the step motor and lateral motion carriage effects should be the same within deviation curves of these probes. If the surface profile effect is more dominant than the other effects, the deviation curves of these probes should be different from each other. The step motor and lateral motion carriage effect curves are plotted on the same graph and it is shown in Figure 7.8.

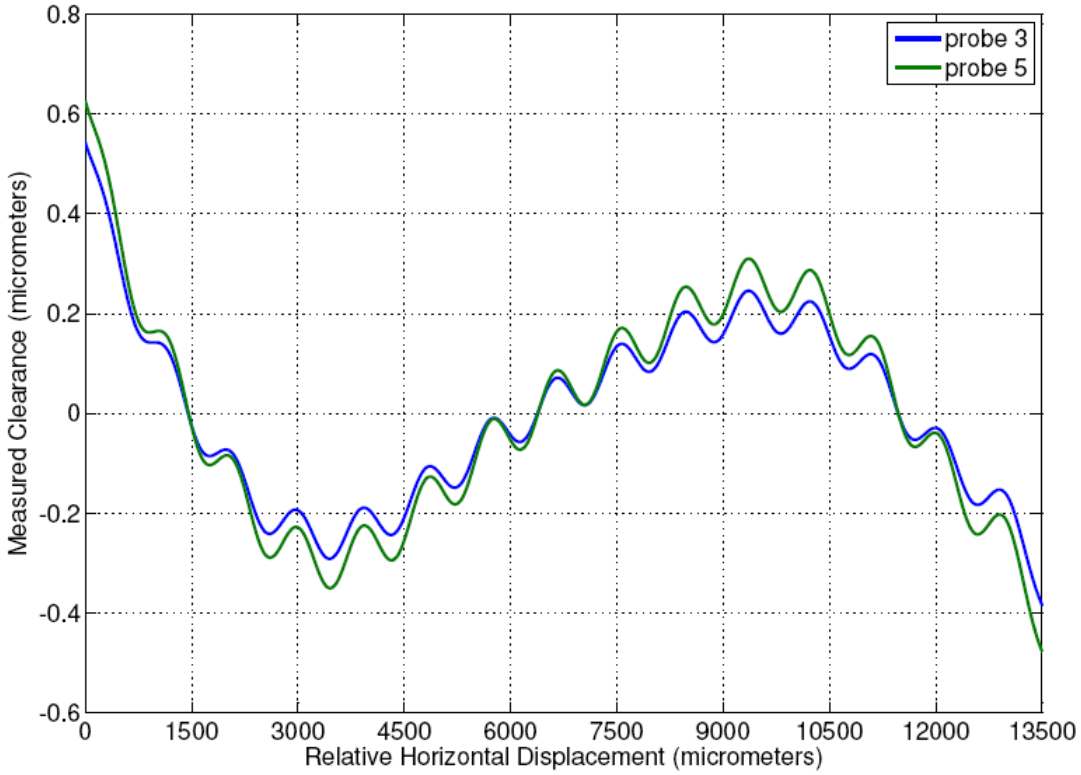

Figure 7.8. Step motor and lateral motion carriage effect for probe 3 and probe 5 in the forward direction with air

It can be seen from Figure 7.8 that the step motor and lateral motion carriage effects are similar in both probes 3 and 5. The difference between the probe 3 and probe 5 results has a standard deviation of 39.75 nanometers. Therefore, it is concluded that the deviation of the measured clearance values from linear curve fit arises from the step motor and the lateral carriage motion.

The average deviation curve and the differences of each experiment from this average for the probe 3 in the backward direction with air are shown in Figure 7.9.a and 7.9.b.

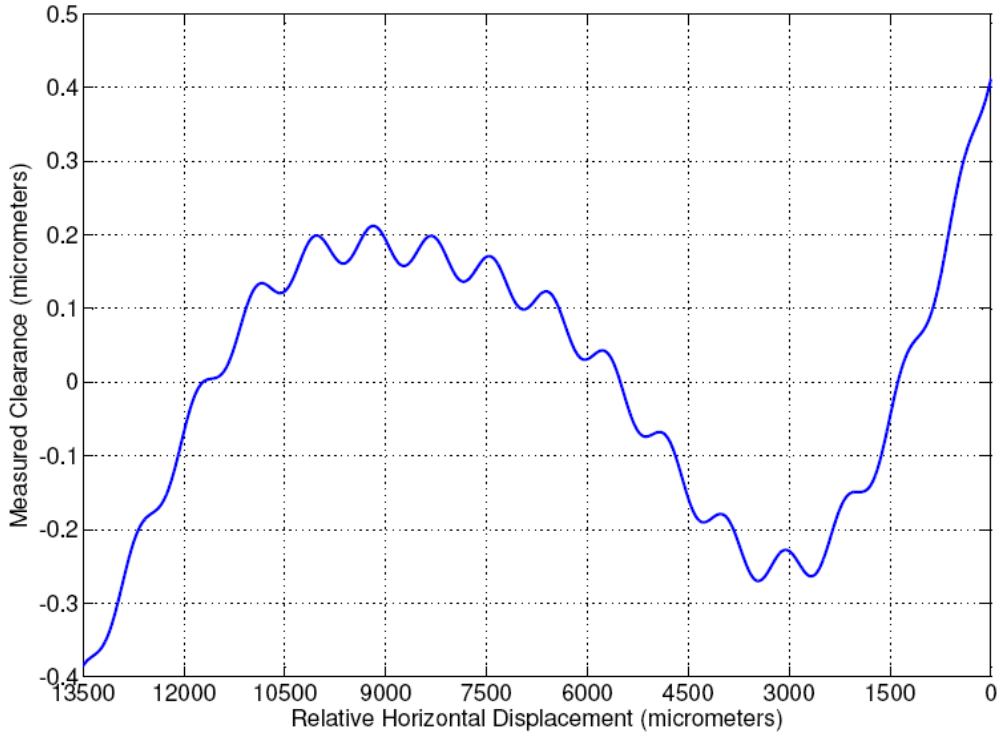

(a)

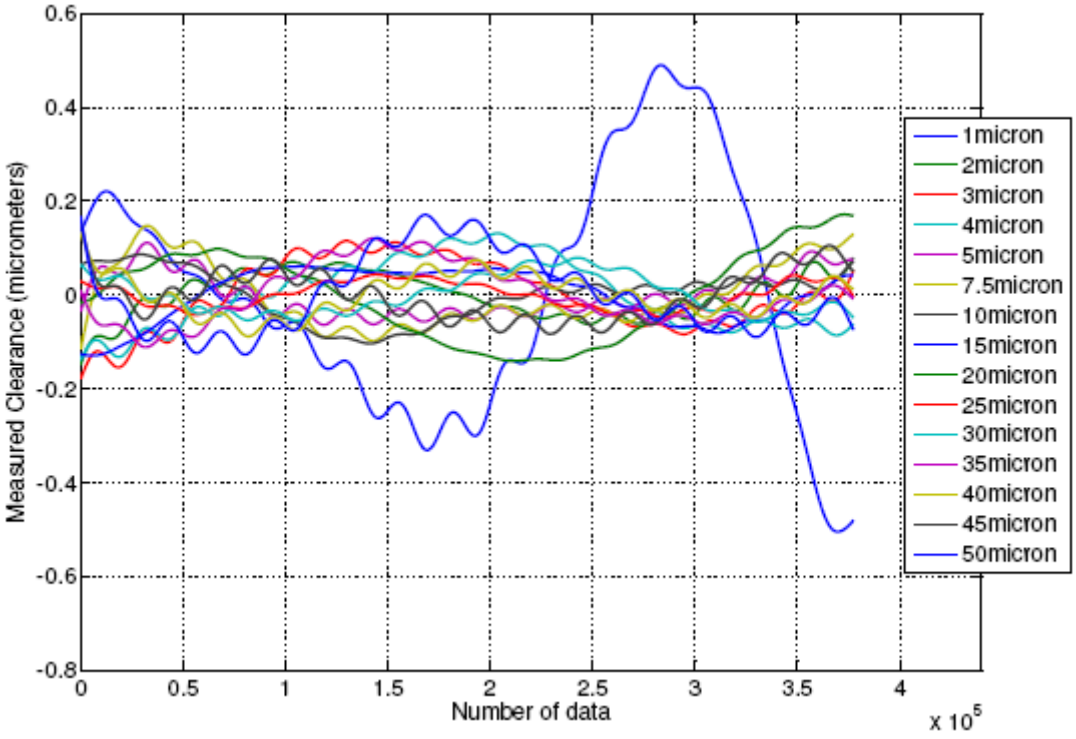

(b)

Figure 7.9. (a) Average step motor and lateral motion carriage effect, (b) the differences from average effect for probe 3 in the backward direction in air

The standard deviations of the difference between each experiment and the average one are tabulated in Table 7.5.

Table 7.5. Standard deviations of the differences from the average deviation curve for probe 3 in the backward direction with air

Δh (μm)	Standard deviation of the difference (μm)
1	0.2552
2	0.04673
3	0.07326
4	0.04216
5	0.04517
7.5	0.06753
10	0.05218
15	0.05623
20	0.09396
25	0.02764
30	0.04051
35	0.06198
40	0.07495
45	0.05113
50	0.08142

It is statistically found from Table 7.5 that the average deviation curve of probe 3 represents all experiments in the forward direction in the air with error of 71.34 ± 53.81 nanometers.

The results of the linearity of the new and previous measured clearance values for the data of probe 3 in the backward direction with air is shown in Table 7.6.

Table 7.6 Comparison of the linearity of the measured clearance previous and new values for probe 3 in the backward direction in air

Δh (μm)	R^2 (previous)	R^2 (new)
1	0.8218	0.5343
2	0.6859	0.9745
3	0.8716	0.9861
4	0.9474	0.9935
5	0.9769	0.9983
7.5	0.9914	0.9988
10	0.9967	0.9996
15	0.9969	0.9998
20	0.9985	0.9997
25	0.9992	1
30	0.9996	1
35	0.9995	1
40	0.9997	1
45	0.9998	1
50	0.9998	1

It is seen that maximum increase in the linearity occurs at $\Delta h = 2$ μm and the R^2 values are equal to one in whole experiments after $\Delta h = 20$ μm. Therefore, the measured clearance values can be corrected by determining effects of the step motor and the lateral motion carriage.

The average deviation curve and the differences of each experiment from this average for the probe 5 in the backward direction with air are shown in Figure 7.10.a and 7.10.b.

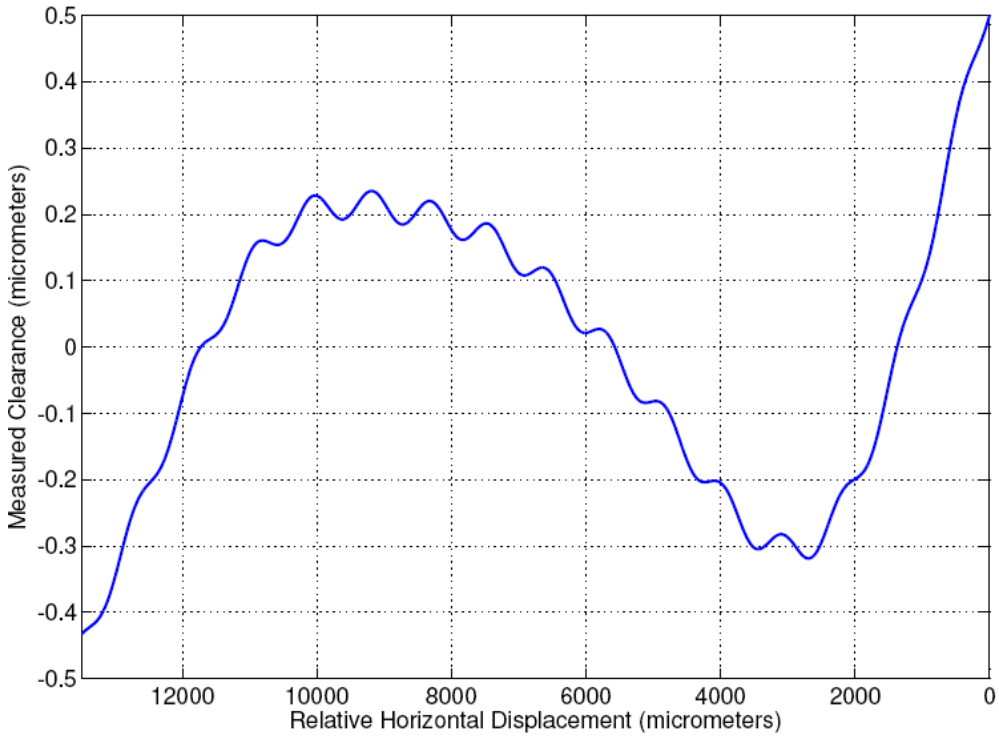

(a)

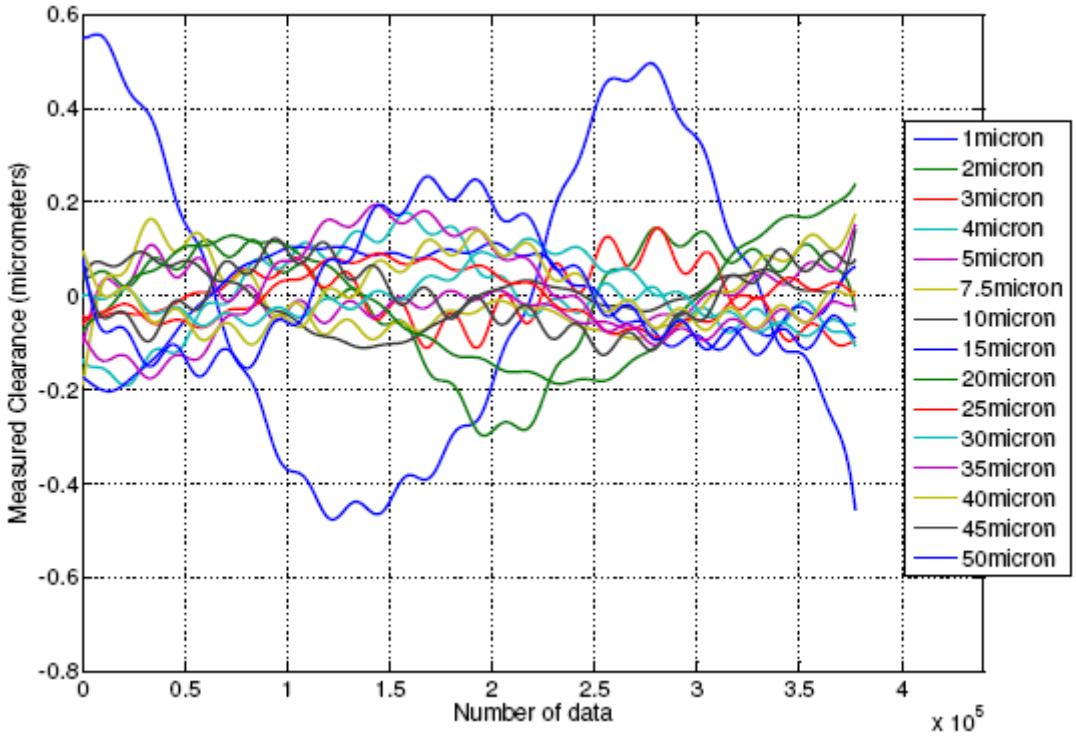

(b)

Figure 7.10. (a) Average step motor and lateral motion carriage effect, (b) the differences from average effect for probe 5 in the backward direction in air

The standard deviations of the difference between each experiment and the average one are tabulated in Table 7.7.

Table 7.7. Standard deviations of the differences from the average deviation curve for probe 5 in the backward direction with air

Δh (μm)	Standard deviation of the difference (μm)
1	0.3308
2	0.1249
3	0.06219
4	0.08979
5	0.04423
7.5	0.07389
10	0.05504
15	0.09342
20	0.1207
25	0.05195
30	0.05522
35	0.1062
40	0.06254
45	0.06582
50	0.1254

It is statistically found from Table 7.7 that the average deviation curve of probe 5 represents all experiments in the forward direction in the air with error of 95.48 ± 72.51 nanometers.

The results of the linearity of the new and previous measured clearance values for the data of probe 5 in the backward direction with air is shown in Table 7.8.

Table 7.8 Comparison of the linearity of the measured clearance previous and new values for probe 5 in the backward direction in air

Δh (μm)	R^2 (previous)	R^2 (new)
1	0.9047	0.7031
2	0.7425	0.889
3	0.9235	0.9907
4	0.8623	0.9812
5	0.9344	0.9967
7.5	0.9821	0.998
10	0.9935	0.9993
15	0.9943	0.9994
20	0.9973	0.9995
25	0.9986	0.9999
30	0.9994	0.9999
35	0.9991	0.9999
40	0.9996	1
45	0.9996	1
50	0.9996	0.9999

It is seen that maximum increase in the linearity occurs at $\Delta h = 2$ μm and the R^2 values are equal to one in whole experiments after $\Delta h = 20$ μm. Therefore, the measured clearance values can be corrected by determining effects of the step motor and the lateral motion carriage.

The step motor and lateral motion carriage effect curves are plotted on the same graph and it is shown in Figure 7.11.

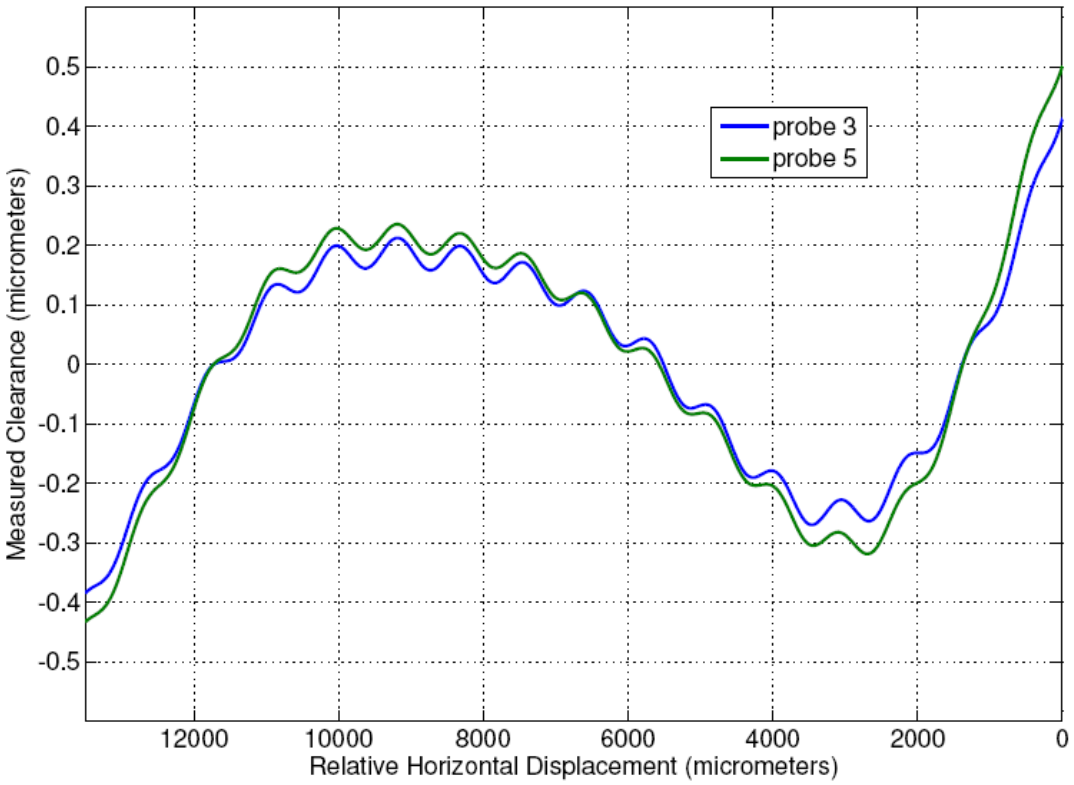

Figure 7.11. Step motor and lateral motion carriage effect for probe 3 and probe 5 in the backward direction with air

It can be seen from Figure 7.11 that the step motor and lateral motion carriage effects are similar in both probes 3 and 5. The difference between the probe 3 and probe 5 results has a standard deviation of 34.65 nanometers. Therefore, it is concluded that the deviation of the measured clearance values from linear curve fit arises from the step motor and the lateral carriage motion.

The average deviation curve and the differences of each experiment from this average for the probe 3 in the forward direction with lubricant are shown in Figure 7.12.a and 7.12.b.

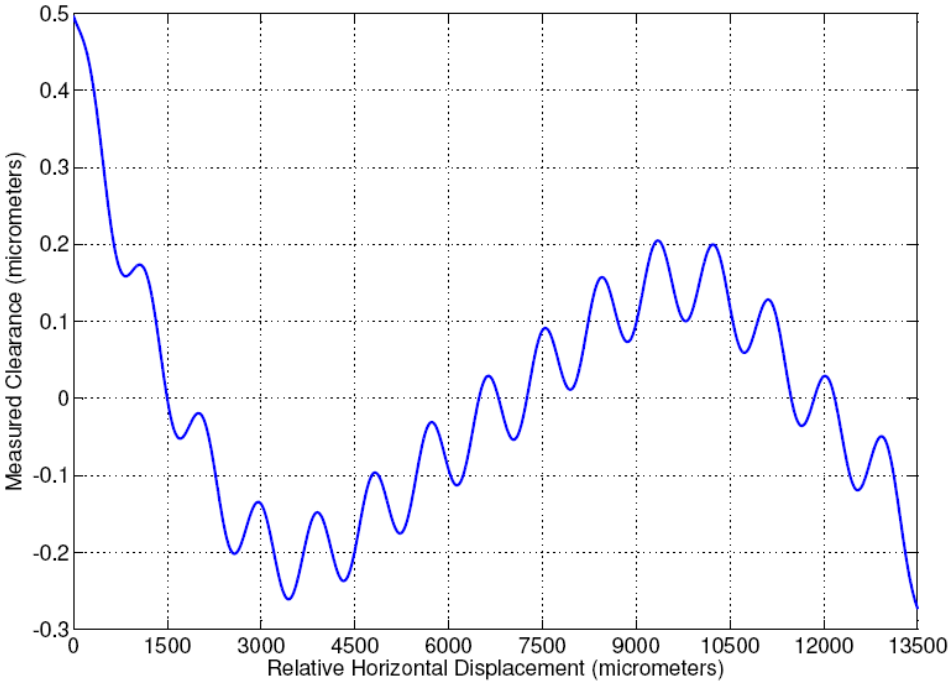

(a)

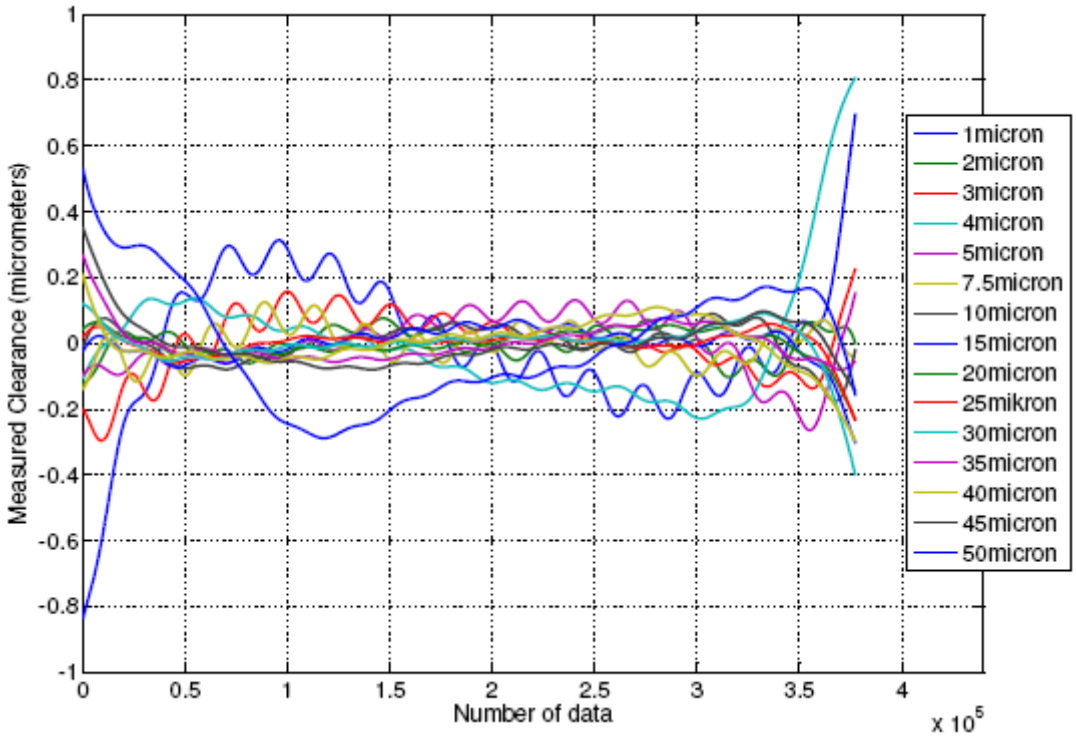

(b)

Figure 7.12. (a) Average step motor and lateral motion carriage effect, (b) the differences from average effect for probe 3 in the forward direction in lubricant

The standard deviations of the difference between each experiment and the average one are tabulated in Table 7.9.

Table 7.9. Standard deviations of the differences from the average deviation curve for probe 3 in the forward direction in the lubricant

Δh (μm)	Standard deviation of the difference (μm)
1	0.2151
2	0.04407
3	0.09635
4	0.1911
5	0.09001
7.5	0.05235
10	0.05507
15	0.05216
20	0.04211
25	0.03664
30	0.06103
35	0.0534
40	0.07089
45	0.06983
50	0.1811

It is statistically found from Table 7.9 that the average deviation curve of probe 3 represents all experiments in the forward direction in the air with error of 80.72 ± 54.76 nanometers.

The results of the linearity of the new and previous measured clearance values for the data of probe 3 in the forward direction with lubricant is shown in Table 7.10.

Table 7.10 Comparison of the linearity of the measured clearance previous and new values for probe 3 in the forward direction in lubricant

Δh (μm)	R^2 (previous)	R^2 (new)
1	0.3901	0.1027
2	0.9712	0.9935
3	0.9825	0.9849
4	0.9852	0.9838
5	0.9877	0.9963
7.5	0.9967	0.9991
10	0.9961	0.9992
15	0.9985	0.9998
20	0.9990	0.9999
25	0.9995	0.9999
30	0.9996	0.9999
35	0.9996	1
40	0.9997	1
45	0.9998	1
50	0.9996	0.9998

It is seen that maximum increase in the linearity occurs at $\Delta h = 2$ μm and the R^2 values are equal to one in whole experiments after $\Delta h = 30$ μm. Therefore, the measured clearance values can be corrected by determining effects of the step motor and the lateral motion carriage.

The average deviation curve and the differences of each experiment from this average for the probe 5 in the forward direction with lubricant are shown in Figure 7.13.a and 7.13.b.

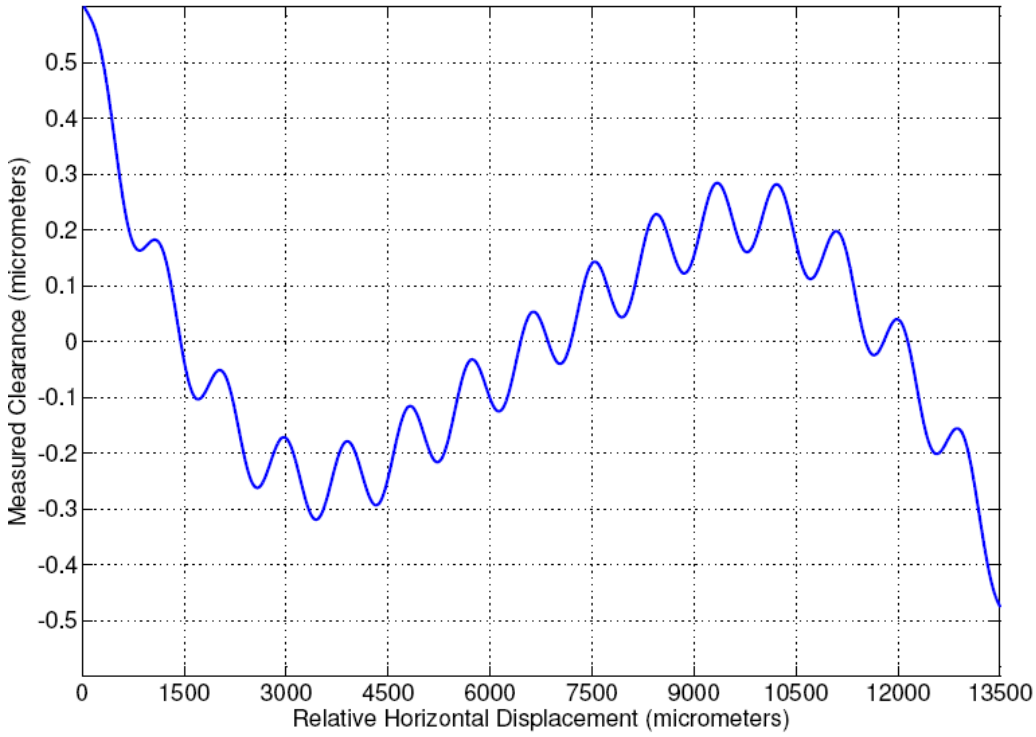

(a)

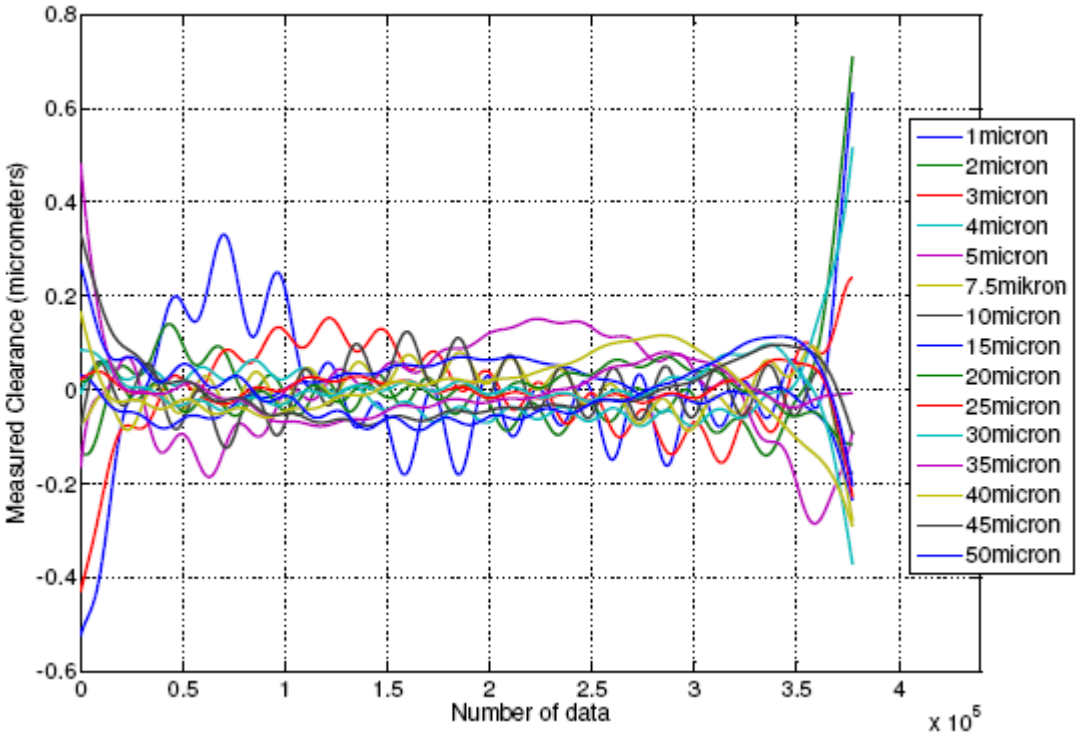

(b)

Figure 7.13. (a) Average step motor and lateral motion carriage effect, (b) the differences from average effect for probe 5 in the forward direction in lubricant

The standard deviations of the difference between each experiment and the average one are tabulated in Table 7.11.

Table 7.11. Standard deviations of the differences from the average deviation curve for probe 5 in the forward direction in the lubricant

Δh (μm)	Standard deviation of the difference (μm)
1	0.154
2	0.1054
3	0.1033
4	0.08067
5	0.1093
7.5	0.05084
10	0.05508
15	0.05032
20	0.0375
25	0.03208
30	0.05449
35	0.06489
40	0.07247
45	0.06881
50	0.06752

It is statistically found from Table 7.11 that the average deviation curve of probe 5 represents all experiments in the forward direction in the air with error of 73.78 ± 32.31 nanometers.

The results of the linearity of the new and previous measured clearance values for the data of probe 5 in the forward direction with lubricant is shown in Table 7.12.

Table 7.12 Comparison of the linearity of the measured clearance previous and new values for probe 5 in the forward direction in lubricant

Δh (μm)	R^2 (previous)	R^2 (new)
1	0.9061	0.892
2	0.9778	0.9905
3	0.987	0.9877
4	0.9892	0.9971
5	0.9793	0.9958
7.5	0.9950	0.9996
10	0.9956	0.9996
15	0.9998	0.9998
20	0.9986	0.9999
25	0.9993	1
30	0.9994	1
35	0.9994	1
40	0.9995	1
45	0.9997	1
50	0.9997	0.9998

It is seen that maximum increase in the linearity occurs at $\Delta h = 2$ μm and the R^2 values are equal to one in whole experiments after $\Delta h = 20$ μm. Therefore, the measured clearance values can be corrected by determining effects of the step motor and the lateral motion carriage.

The step motor and lateral motion carriage effect curves are plotted on the same graph and it is shown in Figure 7.14.

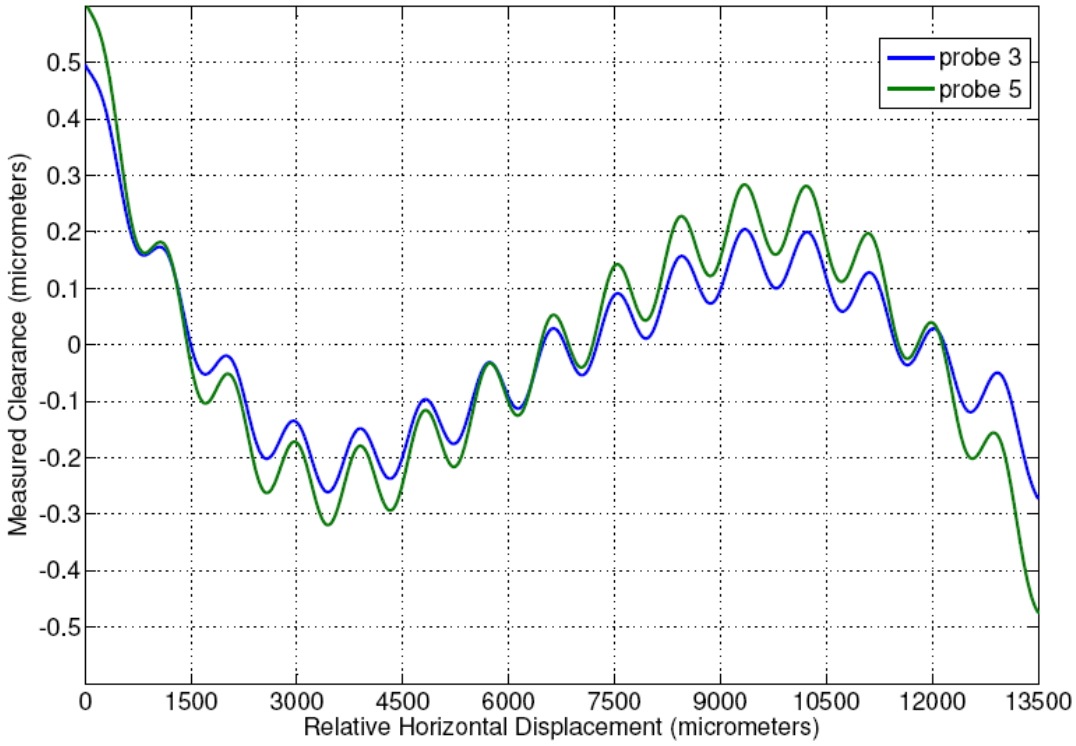

Figure 7.14. Step motor and lateral motion carriage effect for probe 3 and probe 5 in the forward direction with lubricant

It can be seen from Figure 7.14 that the step motor and lateral motion carriage effects are similar in both probes 3 and 5. The difference between the probe 3 and probe 5 results has a standard deviation of 60.33 nanometers. Therefore, it is concluded that the deviation of the measured clearance values from linear curve fit arises from the step motor and the lateral carriage motion.

The average deviation curve and the differences of each experiment from this average for the probe 3 in the backward direction with lubricant are shown in Figure 7.15.a and 7.15.b.

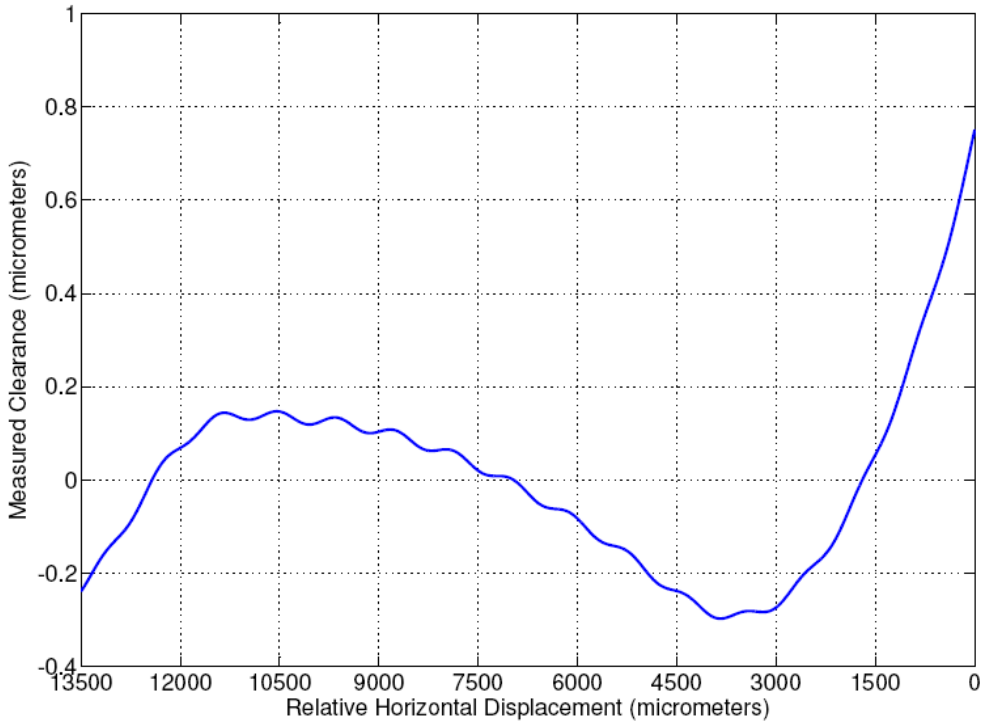

(a)

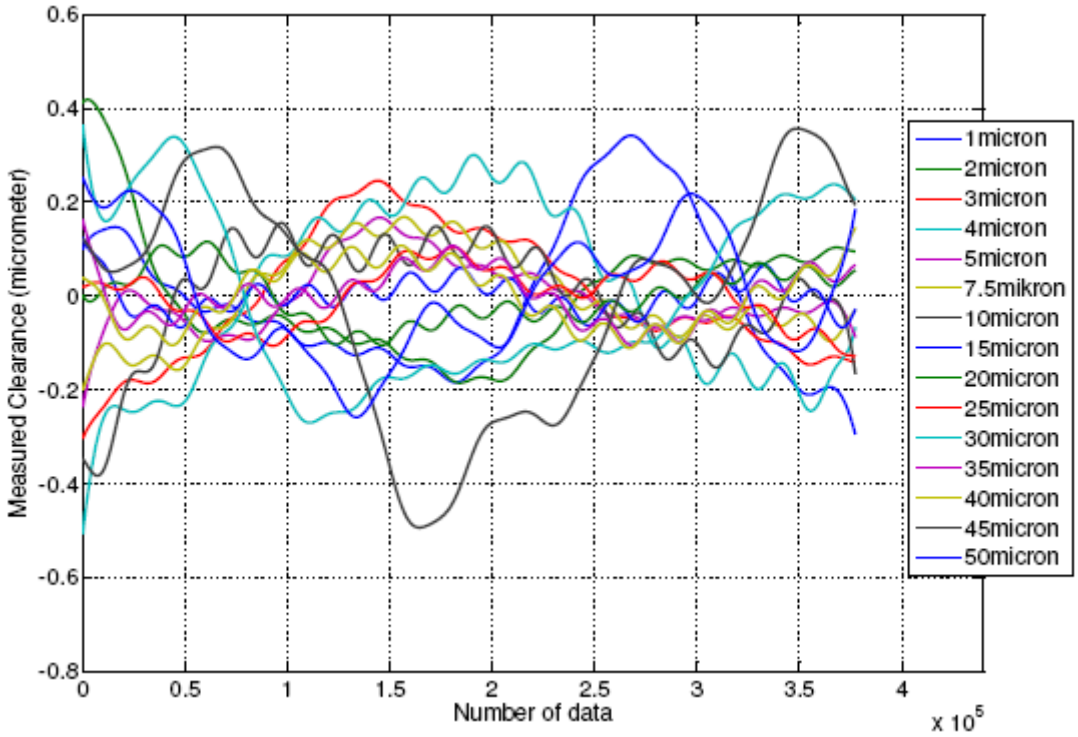

(b)

Figure 7.15. (a) Average step motor and lateral motion carriage effect, (b) the differences from average effect for probe 3 in the backward direction in lubricant

The standard deviations of the difference between each experiment and the average one are tabulated in Table 7.13.

Table 7.13. Standard deviations of the differences from the average deviation curve for probe 3 in the backward direction in the lubricant

Δh (μm)	Standard deviation of the difference (μm)
1	0.1613
2	0.1299
3	0.1363
4	0.1888
5	0.07273
7.5	0.09725
10	0.1213
15	0.03503
20	0.05597
25	0.06049
30	0.1839
35	0.05359
40	0.0652
45	0.2426
50	0.1319

It is statistically found from Table 7.13 that the average deviation curve of probe 3 represents all experiments in the forward direction in the air with error of 114.6 ± 62.35 nanometers.

The results of the linearity of the new and previous measured clearance values for the data of probe 3 in the backward direction with lubricant is shown in Table 7.14.

Table 7.14 Comparison of the linearity of the measured clearance previous and new values for probe 3 in the backward direction in lubricant

Δh (μm)	R^2 (previous)	R^2 (new)
1	0.7337	0.6192
2	0.7147	0.867
3	0.818	0.9302
4	0.9011	0.9438
5	0.9609	0.9937
7.5	0.9837	0.9966
10	0.9893	0.9975
15	0.9975	0.9997
20	0.9984	0.9998
25	0.9994	0.9999
30	0.9985	0.9994
35	0.9994	1
40	0.9995	1
45	0.999	0.9995
50	0.9998	0.9999

It is seen that maximum increase in the linearity occurs at $\Delta h = 2$ μm and the R^2 values are equal to one in whole experiments after $\Delta h = 30$ μm. Therefore, the measured clearance values can be corrected by determining effects of the step motor and the lateral motion carriage.

The average deviation curve and the differences of each experiment from this average for the probe 5 in the backward direction with lubricant are shown in Figure 7.16.a and 7.16.b.

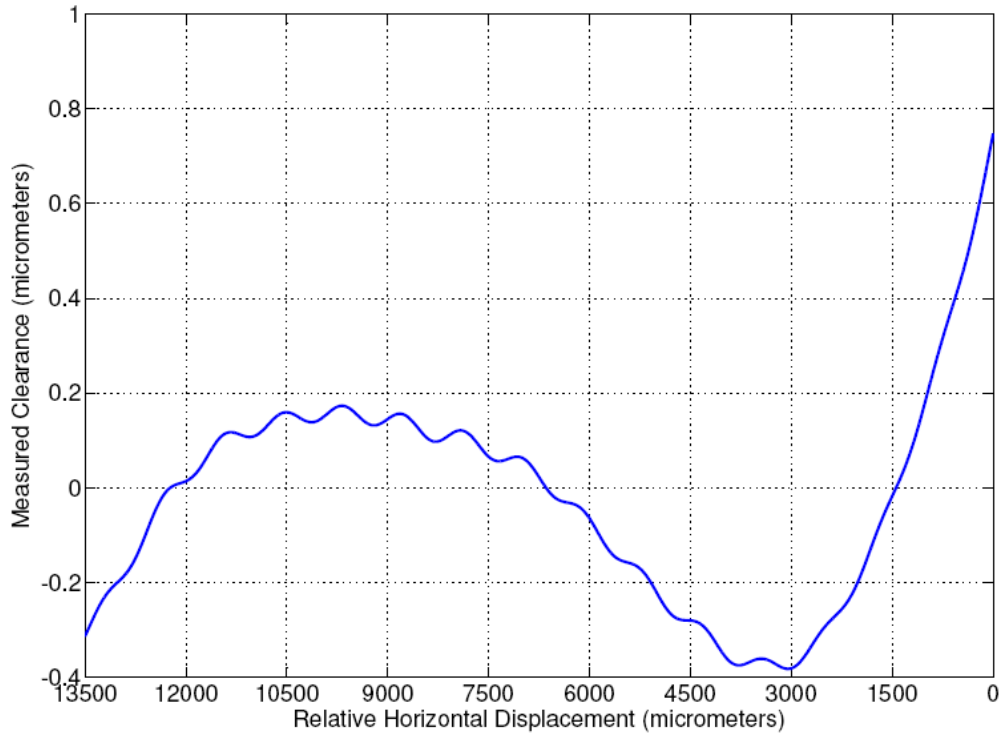

(a)

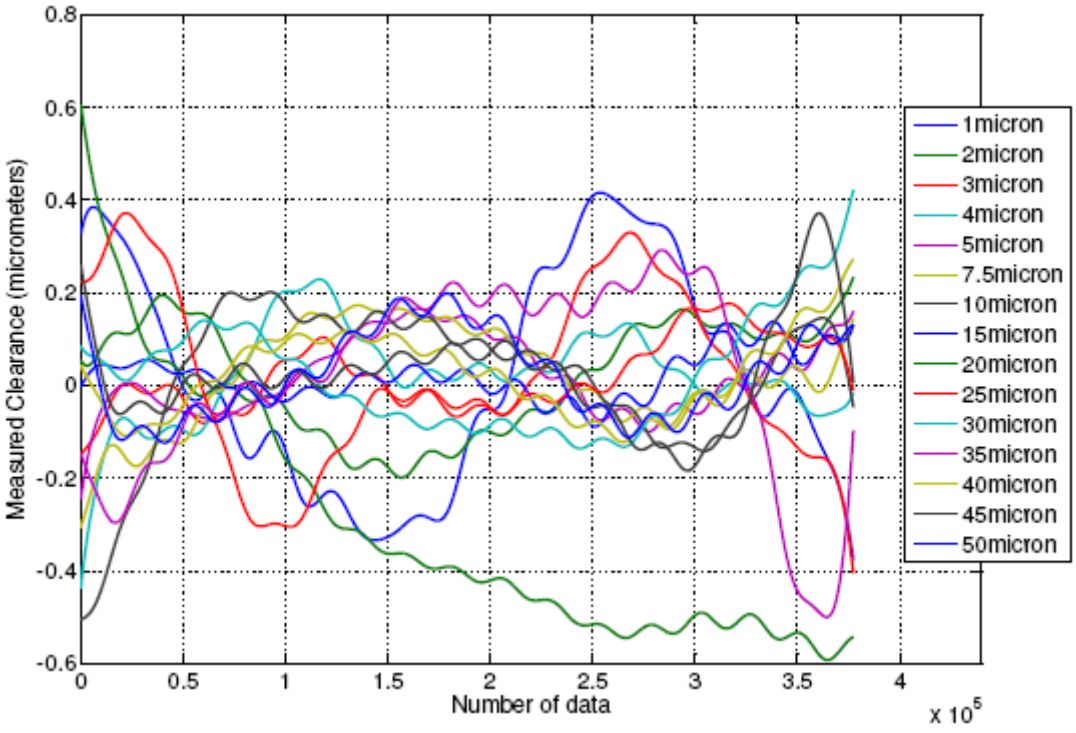

(b)

Figure 7.16. (a) Average step motor and lateral motion carriage effect, (b) the differences from average effect for probe 5 in the backward direction in lubricant

The standard deviations of the difference between each experiment and the average one are tabulated in Table 7.15.

Table 7.15. Standard deviations of the differences from the average deviation curve for probe 5 in the backward direction in the lubricant

Δh (μm)	Standard deviation of the difference (μm)
1	0.2365
2	0.1432
3	0.129
4	0.1001
5	0.08115
7.5	0.1051
10	0.1539
15	0.04989
20	0.2542
25	0.163
30	0.1192
35	0.2084
40	0.08647
45	0.1086
50	0.09263

It is statistically found from Table 7.15 that the average deviation curve of probe 5 represents all experiments in the forward direction in the air with error of 135.4 ± 58.85 nanometers.

The results of the linearity of the new and previous measured clearance values for the data of probe 5 in the backward direction with lubricant is shown in Table 7.16.

Table 7.16 Comparison of the linearity of the measured clearance previous and new values for probe 5 in the backward direction in lubricant

Δh (μm)	R^2 (previous)	R^2 (new)
1	0.9521	0.8952
2	0.6487	0.8299
3	0.9456	0.9647
4	0.8944	0.979
5	0.904	0.9898
7.5	0.9654	0.9951
10	0.9787	0.9956
15	0.9961	0.9998
20	0.9975	0.9996
25	0.9988	0.9994
30	0.9985	0.9998
35	0.9995	0.9995
40	0.9992	0.9999
45	0.9994	0.9999
50	0.9996	1

It is seen that maximum increase in the linearity occurs at $\Delta h = 2$ μm and the R^2 values are equal to one at $\Delta h = 50$ μm. Therefore, the measured clearance values can be corrected by determining effects of the step motor and the lateral motion carriage.

The step motor and lateral motion carriage effect curves are plotted on the same graph and it is shown in Figure 7.17.

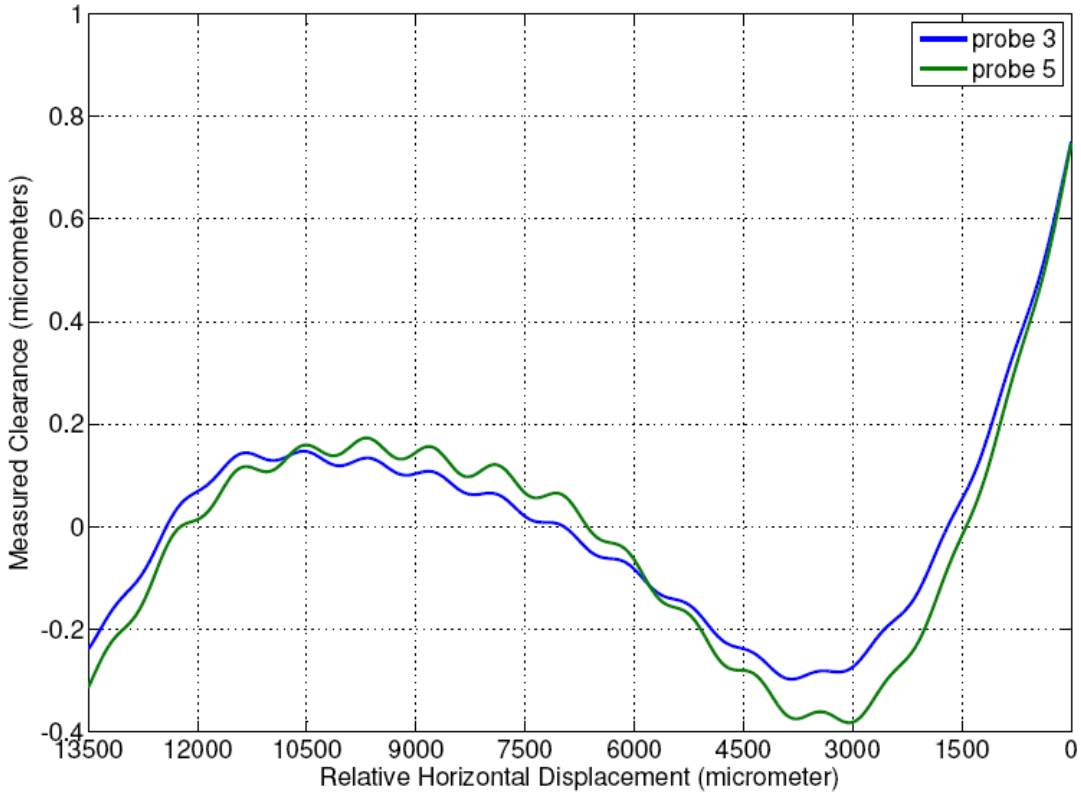

Figure 7.17. Step motor and lateral motion carriage effect for probe 3 and probe 5 in the backward direction with lubricant

It can be seen from Figure 7.16 that the step motor and lateral motion carriage effects are similar in both probes 3 and 5. The difference between the probe 3 and probe 5 results has a mean value of 21.59 nanometers and standard deviation of 50.35 nanometers. Therefore, it is concluded that the deviation of the measured clearance values from linear curve fit arises from the step motor and the lateral carriage motion.

The surface profile of the small cross section of the gold coated mirror is investigated by the Atomic Force Microscope (AFM). Since the AFM can be used to scan limited cross-sections, the R_a values obtained in the experiments can not be compared with the results obtained by AFM. The maximum cross-section scanned by AFM has a cross section of 20×20 μm. The topography, section view and

surface profile of the selected section of the gold coated mirror is shown in Figure 7.18.a , 7.18.b, and 7.18.c, respectively.

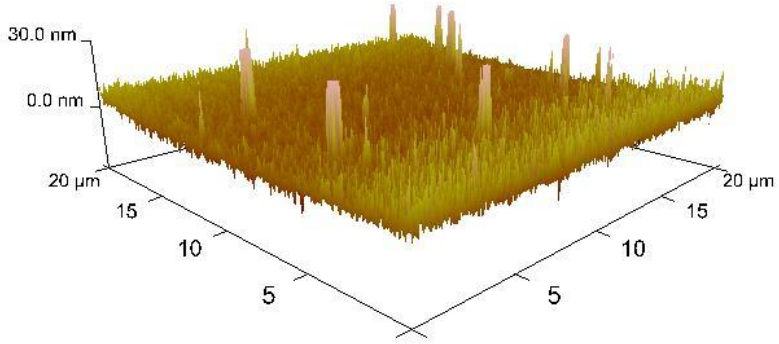

(a)

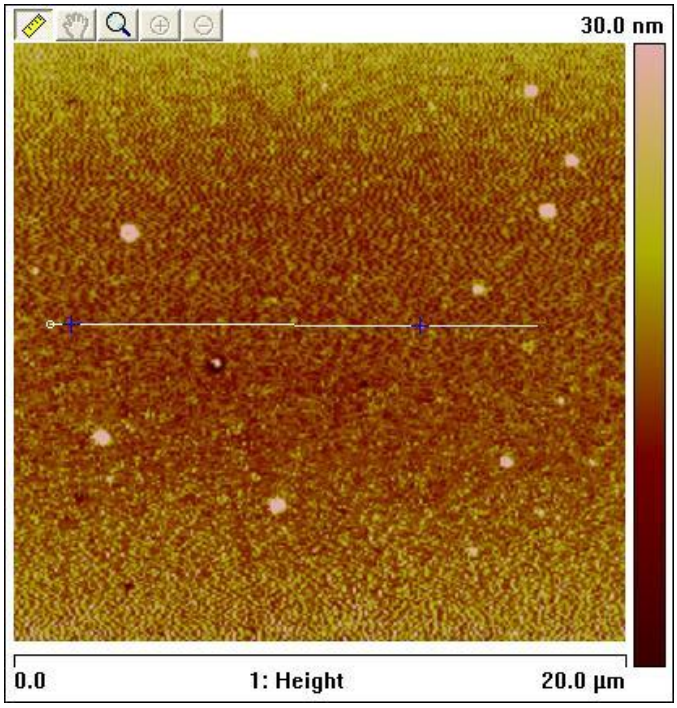

(b)

Figure 7.18. Gold coated mirror surface (a) Topography, (b) Section, (c) Surface profile of the cross section of 20*20 μm

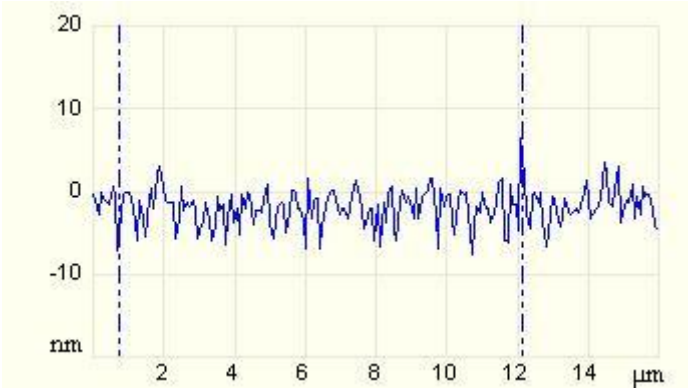

(c)

Figure 7.18. Gold coated mirror surface (a) Topography, (b) Section, (c) Surface profile of the cross section of 20*20 μm (continued)

The average surface roughness value of the section is 0.98 nm.

CHAPTER 8

CONCLUSION

In this study, there are two probes detecting the vertical distance between the probe ends and the gold coated mirror surface. A third probe detects the distance between the probe end and small gold coated mirror attached to the third plate. The experimental data of the two probes are used to determine the vertical distances at any lateral location of the gold coated mirror. In each direction 15 experiments are conducted. Since there are two directions and two different media, each probe has 60 different experimental data. In the experiments;

1. The “V” curve is obtained at the beginning of the experiments. It enhances the smoothness of the optical output in each experimental data. The required inclination can be easily generated by taking “V” curve as a reference. If “V” curve experiments are not performed, then the decision on the direction of the motion and maximum and minimum point locations can not be easily made because the experimental data may intersect with the reference line and then there is an adverse trend before and after this intersection point. This is illustrated in Figure 8.1.

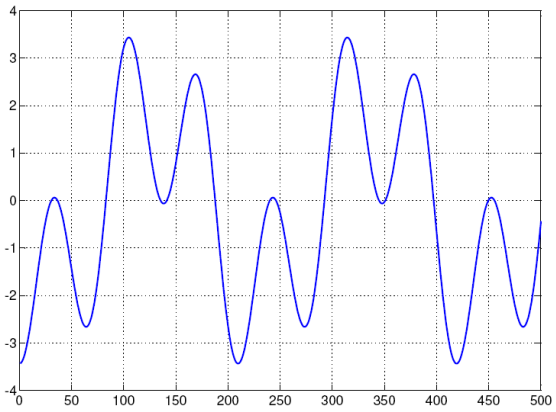

Figure 8.1 The mixed region “V” curve

From Figure 8.1, it can be easily seen that the direction of the motion can not be determined. Also, the locations of the local maximum and minimum points can not be determined either. Therefore, obtaining "V" curve in this study prevents the possibility of uninterpretable experimental data such as in Figure 8.1.

2. The clearances in the Cartesian model can be accurately measured in the range of 0-50 μm with fiber optic interferometry. However, the results of the experiments conducted with air are more accurate than those with lubricant. The reason of this difference can be explained with the refractive index difference of lubricant and air. The index of refraction of the lubricant is measured with a refractrometer and it is equal to 1.484764 and index of refraction of air is taken as 1. Since the fiber optic cables are made from glass and their index of refraction is approximately 1.5, the visibility of the fringes with air is better than the visibility with lubricant. The visibility of experiments with air is approximately 60 times of the experiments with lubricant.

3. From the measured clearance curves, it is clearly seen that measured values deviate from the set values of the micrometers. In order to investigate the reasons of that deviation, linear curve fit of the measured clearance curves are taken and subtracted from the measured clearance values. The remaining part is the source of that deviation. In all of the experiments, this procedure is applied and it is found that there is a one common deviation curve with a maximum deviation of 95 ± 70 nm. It is also important that the deviation curves for both probe 3 and probe 5 confirm each other and the difference of these two curves is 40 nm maximum. After taking Fourier transform of this deviation curves, it is concluded that in each deviation curve there is a peak frequency located at the 0.2 Hz, which is the period of one revolution of the step motor. This effect result in a sinusoidal form in the deviation curves. In order obtain this effect; a sinusoidal curve fit is applied to the deviation curve. It is described as the gear motion characteristics of the lateral motion carriage. This characteristic is exemplified in Figure 8.2.

Figure 8.2. Schematic of the characteristics of the lateral motion carriage gear

Moreover, there is another effect, the intensity dominant effect, which has no periodicity but has a down-up-down trend in the forward direction and the inverse trend in the backward direction. This trend has a maximum difference of 1 μm during the 13.5 mm lateral motion. A 9^{th} degree polynomial curve fit is applied to obtain this trend. This effect is described as the change in the motion of the lateral motion carriage shaft in the vertical direction.

4. After obtaining the common deviation curve in all experiments, the average of this deviation curve for each probe in each direction and in each medium is taken and then subtracted from the measured clearance values. The R^2 values of the previous and new measured clearance values are compared and the R^2 values in the new measured clearance values are generally much higher than the previous ones. Especially, the R^2 values increase in the range of 0-10 μm which is the actual radial clearance range of piston cylinder system in the hermetically sealed compressors. However, the R^2 values of the experiments with lubricant have some inverse characteristics at some values with respect to that of with air. This result is due to the different optical characteristics of air and lubricant. The reason is not only the index of refraction difference but also the simultaneous discontinuities occurring in the experiments with lubricant. The experimental data of probe 3 and probe 5 with lubricant when $\Delta h = 15$ μm in the forward direction is shown Figure 8.3.a and 8.3.b, respectively.

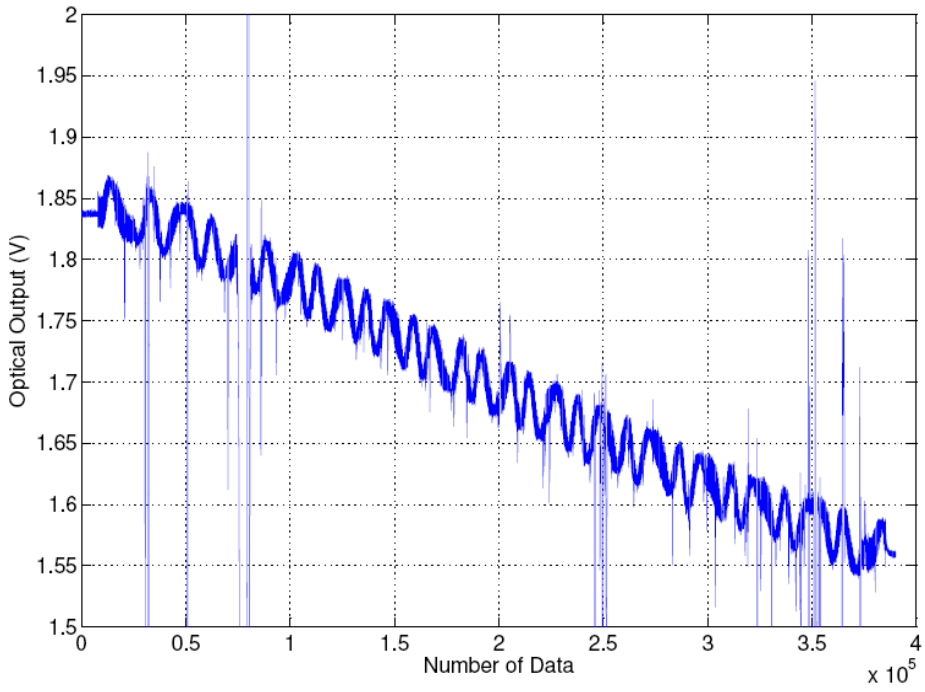

(a)

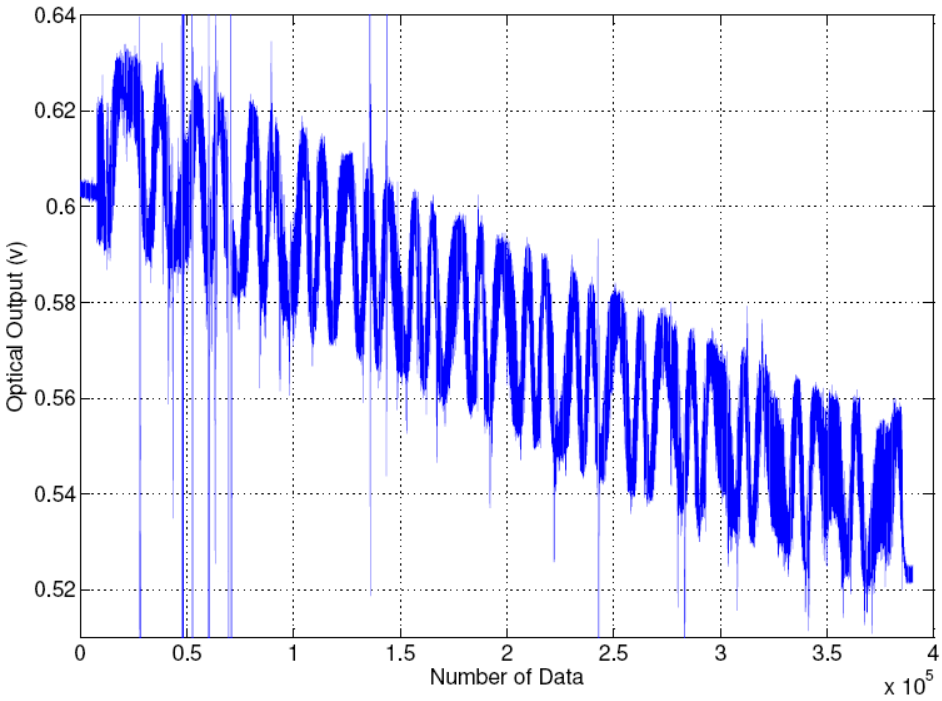

(b)

Figure 8.2. Optical output, (a) probe 3, (b) probe 5 with lubricant

As it can be seen from Figure 8.2, the simultaneous discontinuities occur more frequently in the probe 3 data than probe 5 data. The reason of this is the vertical distance difference of probe 3 and probe 5 with respect to the gold coated mirror. Since probe 3 is closer to the gold coated mirror, the intensity detected by the photo-detector is higher than that of probe 5. The idea of using a probe closer to the gold coated mirror is to perform characterization of the dynamics occurring in the Cartesian model of the piston cylinder system. However, results show that the closer probe can result in worse results than the remote one.

REFERENCES

[1]Encyclopedia,http://wpcontent.answers.com/wikipedia/commons/5/5d/Refrigeration.png, 14 April 2009.

[2] J.E.Shigley and C.R.Mischke. Mechanical Engineering Design. 6th Edition. 2003.

[3] Y.Z. Hou and S. Granick. Microscopic study of thin film lubrication and its contribution to macroscopic tribology. Tribology Letters 5, 1998, pp.81-88.

[4] C. Zhang. Research on thin film lubrication: State of the art. Tribology International 38, 2005, pp.443-448.

[5] Cann PM, Spikes HA. The development of a spacer layer imaging method (SLIM) for mapping elastohydrodynamic contacts. Tribology Trans., 1996, 39(4):915-21.

[6] Johnston GJ, Wayte R, Spikes HA. The measurement and study of very thin film lubricant films in concentrated contacts. Tribology Trans, 1991, 34(2): 187-94.

[7] Luo JB, Wen SZ, Huang P. Study on mechanism of thin film lubrication. J Tsinghua University, 1994, 34(s3): 1-9.

[8] Hartl M, Krupka I, Poliscuk R, et al. An automatic system for real time evaluation of EHD film thickness and shape based on the colorimetric interferometry. Trib Trans, 1999, 42(2): 303-9.

[9] Guo F, Wong PL. A multi-beam intensity-based approach for lubricant film measurements in non-conformal contacts. Proc Instn Mech Engrs, Part J Eng Tribology, 2002, 216(J5):281-91.

[10] H.A.Spikes. Thin films in elastohydrodynamic lubrication: the contribution of experiment. Proc Instn Mech Engrs, Part J Eng Tribology, 1999, 213, pp.335-352.

[11] I.Krupka, M.Hartl, R.Poliscuk, J.Cermac, M.Liska. Experimental evaluation of EHD film shape and its comparison with numerical solution. J.of Tribology, 2000, 122, pp.689-696.

[12] R.P.Glovnea, A.K.Forrest, A.V.Oliver, H.A.Spikes. Measurement of sub-nanometer lubricant films using ultra-thin film interferometry. Trib. Letters, 2003, 15(3), pp. 217-230.

[13] F.Guo and P.L.Wong. A wide range measuring system for thin lubricating film: From nano to micro thickness. Trib.Letters., 2004, 17, pp.521-531.

[14] J.R.Cho, S.J.Moon. A numerical analysis of the interaction between the piston oil film and the component deformation in a reciprocating compressor. Trib.Int., 2005, 38, pp.459-468.

[15] A.T.Prata, J.R.S. Fernandes and F.Fagotti. Dynamic analysis of piston secondary motion for small reciprocating compressors. Trans.ASME, 2000, 122, pp.752-760.

[16] N.Sathitanon, S.Pullteap. A fiber optic interferometric sensor for dynamic measurement. Int.J.Comp.Sci.Eng., 2007, 2(2), pp.63-66.

[17] Y.Nagaike, Y.Wu and H.Ikeda. Sub-micron position sensor with a fiber-optic interferometer. IEEE, 1999, pp.1751-1753.

[18] M.A.V.Zeeland, T.Deterly and D.K.Finkenthal. Fiber optic two-color vibration compensated interferometer for plasma density measurements. Rev.Sci.Inst., 2006,10F325,1-3.

[19] D.Iannuzzi, S.Deladi and J.W.Berenschot, S.de Man and K.Heeck and M.C.Elwenspoek. Fiber-top atomic force microscope. Rev.Sci.Inst., 2006, 77, 106105, 1-3.

[20] P.Hlubina, D.Ciprian, J.Lunacek and M.Lesnak. Thickness of SiO_2 thin film on silicon wafer measured by dispersive white-light spectral interferometry. Apply.Phys., 2006, B84, pp. 511-516.

[21] T.S.Francis, X.Y.Yu. Introduction to Optical Engineering. 1997, Cambridge Press.

[22] Introduction to Optics. F.L.Pedrotti and L.S.Pedrotti. Prentice Hall. 1993.

[23] Furnace company, www.tvu.com/PNextGenTFWeb.htm, 15 April 2009.

[24] Physics animations, http://physics-animations.com/sensors/English/interf.htm, 12 January 2009

APPENDIX A

THEORY OF INTERFERENCE

In the interference phenomena there are two waves, represented by $\overrightarrow{E_1}$ and $\overrightarrow{E_2}$ which are the vectors of the electric fields. In cases of interference, both waves originate from a single light source and reunite after travelling along different paths. The direction of the waves need not be the same when they come together, however, so that whereas they maintain the same frequency, they do not have the same propagation vector $\vec{k}$. The wave equations of the waves are presented in Equation A.1.a and A.1.b.

$$\overrightarrow{E_1} = \overrightarrow{E_{01}} \times \cos(\overrightarrow{k_1} \bullet \vec{r} - \omega \times t + \varepsilon_1) \qquad \text{(A.1.a)}$$

$$\overrightarrow{E_2} = \overrightarrow{E_{02}} \times \cos(\overrightarrow{k_2} \bullet \vec{r} - \omega \times t + \varepsilon_2) \qquad \text{(A.1.b)}$$

At some general point P, defined by position vector $\vec{r}$, the waves intersect to produce a disturbance whose electric field $\overrightarrow{E_p}$ is given by the principle of superposition,

$$\overrightarrow{E_p} = \overrightarrow{E_1} + \overrightarrow{E_2}$$

The radiant power density, or irradiance measures the time average of the square of the wave amplitude and denoted by I and it is equal to;

$$I = \varepsilon_0 \times c \times < \overrightarrow{E^2} > \qquad \text{(A.2)}$$

Then, the resultant intensity at point P is given by

$$I = \varepsilon_0 \times c \times < \overrightarrow{E_p}^2 >= \varepsilon_0 \times c \times < \overrightarrow{E_p} \bullet \overrightarrow{E_p} >= \varepsilon_0 \times c \times < (\overrightarrow{E_1} + \overrightarrow{E_2}) \bullet (\overrightarrow{E_1} + \overrightarrow{E_2}) >$$

Or

$$I = \varepsilon_0 \times c \times < \overrightarrow{E_1}^2 + \overrightarrow{E_2}^2 + 2 \times \overrightarrow{E_1} \bullet \overrightarrow{E_2} > \quad \text{(A.3)}$$

In the equation A.3, the first two terms in the bracket belong to the irradiances of the individual waves, I_1 and I_2. The last term depends on an interaction of the two waves and is called the interference term, I_{12}. Then, Equation A.3 can be rewritten in Equation A.4.

$$I = I_1 + I_2 + I_{12} \quad \text{(A.4)}$$

If the light behaved without interference, then $I = I_1 + I_2$. The presence of the third term I_{12} is the indicative of the wave nature of light, which can produce enhancement or diminution of the irradiance through interference. Since $\overrightarrow{E_1}$ and $\overrightarrow{E_2}$ are orthogonal, so that their dot product vanishes, no interference results. When the electric fields are parallel, on the other hand, the interference term makes its maximum contribution. Two beams of unpolarized light produce interference because each can be resolved into orthogonal components of $\vec{E}$ that can be paired off with similar components of the other beam. Each component produces an interference term with $\overrightarrow{E_1} \parallel \overrightarrow{E_2}$. The interference term is given in Equation A.5.

$$I_{12} = 2 \times \varepsilon_0 \times c \times < \overrightarrow{E_1} \bullet \overrightarrow{E_2} > \quad \text{(A.5)}$$

where $\overrightarrow{E_1}$ and $\overrightarrow{E_2}$ are given by Equations A.1.a and A.1.b, respectively. Their dot product is shown in Equation A.6.

$$\overrightarrow{E_1} \bullet \overrightarrow{E_2} = \overrightarrow{E_{01}} \bullet \overrightarrow{E_{02}} \times \cos(\vec{k}_1 \bullet \vec{r} - \omega \times t + \varepsilon_1) \times \cos(\vec{k}_2 \bullet \vec{r} - \omega \times t + \varepsilon_2) \quad \text{(A.6)}$$

This expression can be simplified by first expanding the cosine factors, interpreted as the difference of two angles. Therefore, some new definitions are needed and they are shown in Equation A.7.a and A.7.b.

$$\alpha = \vec{k_1} \bullet \vec{r} + \varepsilon_1 \qquad \text{(A.7.a)}$$

$$\beta = \vec{k_2} \bullet \vec{r} + \varepsilon_2 \qquad \text{(A.7.b)}$$

Therefore, Equation A.6 reduces to a simpler equation shown in Equation A.8.

$$\vec{E_1} \bullet \vec{E_2} = \vec{E_{01}} \bullet \vec{E_{02}} \times \cos(\alpha - \omega \times t) \times \cos(\beta - \omega \times t) \qquad \text{(A.8)}$$

If the cosine function terms are expanded and multiplied to each other, the result is shown in Equation A.9.

$$\vec{E_1} \bullet \vec{E_2} = \vec{E_{01}} \bullet \vec{E_{02}} \times [\cos(\alpha) \times \cos(\beta) \times < \cos^2(\omega \times t) > + \sin(\alpha) \times \sin(\beta) \times < \sin^2(\omega \times t) > + (\cos(\alpha) \times \sin(\beta) + \sin(\alpha) \times \cos(\beta)) \times < \sin(\omega \times t) \times \cos(\omega \times t) >]$$

(A.9)

Where time average are indicated for each time dependent factor. Over any number of complete cycles, these time averages are shown in Equation A.10.

$$< \cos^2(\omega \times t) >= \frac{1}{2} \ , \ < \sin^2(\omega \times t) >= \frac{1}{2}$$

and

$$< \sin(\omega \times t) \times \cos(\omega \times t) >= 0$$

(A.10)

Therefore, Equation A.9 reduces to the form which is shown in Equation A.11.

$$< \vec{E_1} \bullet \vec{E_2} >= \frac{1}{2} \times \vec{E_{01}} \bullet \vec{E_{02}} \times \cos(\alpha - \beta)$$

Or

$$< \vec{E_1} \bullet \vec{E_2} >= \frac{1}{2} \times \vec{E_{01}} \bullet \vec{E_{02}} \times \cos[(\vec{k_1} - \vec{k_2}) \bullet \vec{r} + (\varepsilon_1 - \varepsilon_2)] \quad \text{(A.11)}$$

Where the expression in the brackets is the phase difference between $\vec{E_1}$ and $\vec{E_2}$ and it is denoted by δ which is shown in Equation A.12.

$$\delta = (\vec{k_1} - \vec{k_2}) \bullet \vec{r} + (\varepsilon_1 - \varepsilon_2) \quad \text{(A.12)}$$

Then, the interference term is equal to,

$$I_{12} = \varepsilon_0 \times c \times \vec{E_{01}} \bullet \vec{E_{02}} \times \cos(\delta) \quad \text{(A.13)}$$

Similarly, the irradiance terms I_1 and I_2 can be shown in Equation A.14.a and A.14.b, respectively.

$$I_1 = \varepsilon_0 \times c \times < \vec{E_1}^2 >= \frac{1}{2} \times \varepsilon_0 \times c \times {E_{01}}^2 \quad \text{(A.14.a)}$$

$$I_2 = \varepsilon_0 \times c \times < \vec{E_2}^2 >= \frac{1}{2} \times \varepsilon_0 \times c \times {E_{02}}^2 \quad \text{(A.14.b)}$$

Then, the interference term can be rewritten in terms of the irradiance terms I_1 and I_2 in Equation A.15.

$$I_{12} = 2 \times \sqrt{I_1 \times I_2} \times \cos(\delta) \quad \text{(A.15)}$$

Finally, the total intensity can be written in terms of the irradiance terms in Equation A.16.

$$I = I_1 + I_2 + 2 \times \sqrt{I_1 \times I_2} \times \cos(\delta) \quad \text{(A.16)}$$

APPENDIX B

SPECIFICATIONS OF EXPERIMENTAL INSTRUMENTATION

Table B.1. Specifications of the laser source

Wavelength	1550 nm
Wavelength accuracy	± 20 nm (nominal)
Bandwidth	1.5 nm
Optical Power (mW)	0.8–1 mW (standard)
Optical Power Stability	± 0.004 dB
Fiber Optic Cable End	FC/APC
Fiber Optic Cable Type	Single mode
Power Source	110/220 V AC 60/50 Hz
Dimensions (W*L*H)	260*209*90 mm
Operating Temperature Range (ºC)	0 - +50 ºC
Storing Temperature Range (ºC)	-40 - +70 ºC
Humidity	< 70%

.Table B.2. Specifications of the isolator

Wavelength	1550 nm
Bandwidth	± 10 nm
Maximum Isolation (dB)	45
Minimum Isolation (dB)	40
Typical Insertion Loss (dB)	0.5
Maximum Insertion Loss (dB)	0.6
Return Loss (dB)	55
Fiber Type	Single Mode
Operating Temperature Range (ºC)	0 - +70 ºC
Storing Temperature Range (ºC)	-40 - +85 ºC

Table B.3. Specifications of the beam-splitter

Wavelength	1550 nm
Bandwidth	± 10 nm
Maximum Isolation (dB)	45
Minimum Isolation (dB)	40
Typical Insertion Loss (dB)	0.5
Maximum Insertion Loss (dB)	0.6
Return Loss (dB)	55
Fiber Type	Single Mode
Split Ratio	1*4
Storing Temperature Range (ºC)	-40 - +85 ºC

Table B.4. Specifications of the circulator.

Wavelength	1550 nm
Extinction Ratio (dB)	30
Insertion Loss, Forward Direction (dB)	60
Insertion Loss, Reverse Direction (dB)	60
Peak Isolation (dB)	30
Power Handling (mW)	250
Fiber Type	Single Mode
Return Loss (dB)	60

Table B.5. Specifications of the photo-detector

Detector	Ge PIN
Active Area	Ø 5mm(19.6 mm^2)
Surface Depth	5.1 mm
Wavelength Range	800–1800 nm
Peak Wavelength (λ_p)	1550 nm
Peak Response	0.85 A/W @ λ_p
Output Voltage	0–10 V
Output Impedance	50 Ω
Maximum Output Current	100 mA
Load Impedance	50 Ω
Gain Range	70 dB
Gain Steps	8*10 dB
Gain Switch	8 pos rotary
On/Off Button	Slide
Output	BNC
Optical Head Size	70.1*52.8*21.1 mm
Weight	0.15 kg

Table B.6. Specifications of the fiber optic cable

.	
Wavelength	1550 nm
Bandwidth	± 50 nm
Length	1 m
Outer Diameter	1.8 mm PVC
Inner Diameter	9/125 μm
Fiber Type	Single Mode
Fiber Ends	FC/APC

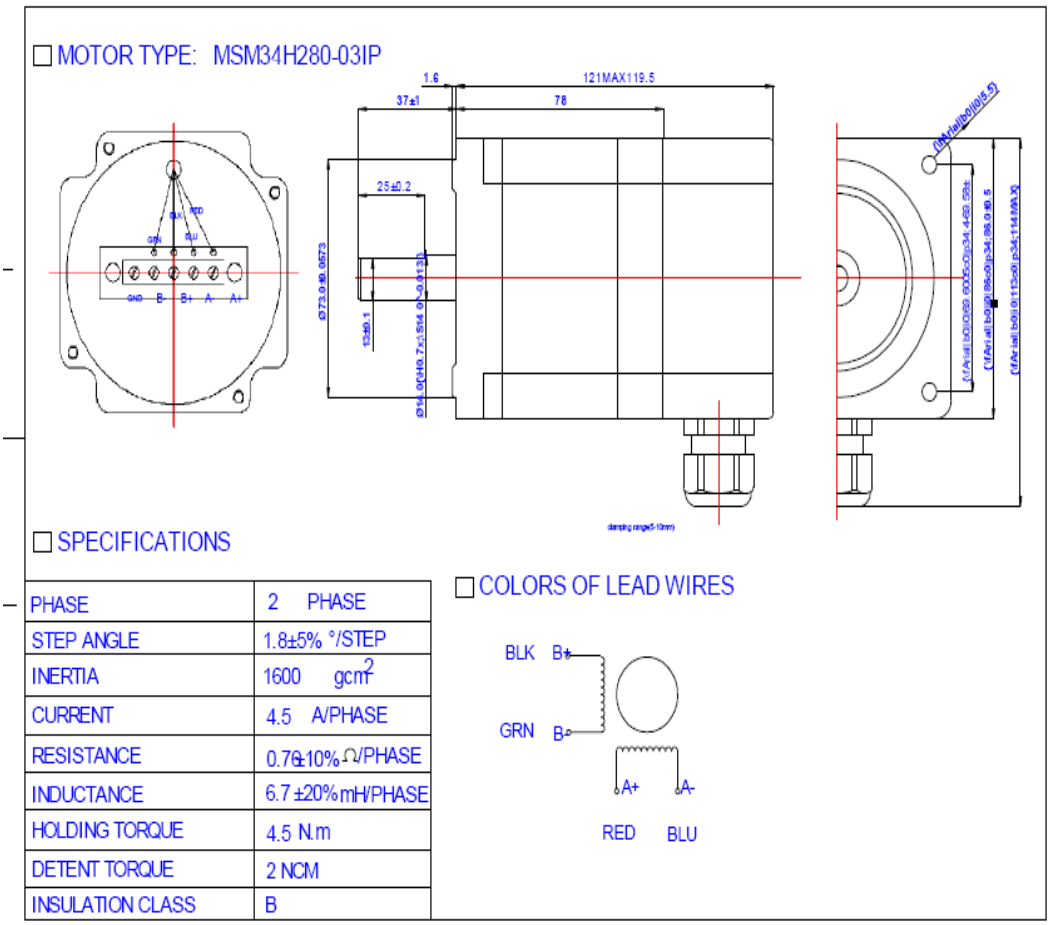

PHASE	2 PHASE
STEP ANGLE	1.8±5% °/STEP
INERTIA	1600 gcm^2
CURRENT	4.5 A/PHASE
RESISTANCE	0.76±10% Ω/PHASE
INDUCTANCE	6.7 ±20% mH/PHASE
HOLDING TORQUE	4.5 N.m
DETENT TORQUE	2 NCM
INSULATION CLASS	B

Figure B.1. Specifications of the step motor

M2MD Bipolar Stepper Motor Driver

TECHNICAL SPECIFICATIONS:

Supply Voltage	20 .. 80 V DC
Output Current	1.8 .. 6.0 A
Step Modes	1/2-, 1/4-, 1/8-, 1/16-, 1/32-, 1/64-step 1/ 5-, 1/10-,1/25-,1/50-,
Current Adjustment	via DIP Switches
Clock Frequency	0 .. 400 kHz max.
Pulse Width (Clock)	min. 1.25 µs high/low
Ambient Temperature	0 °C .. 50 °C (Note: Insure the driver temperature <65 °C)
Connection Type	Screw Type Terminals

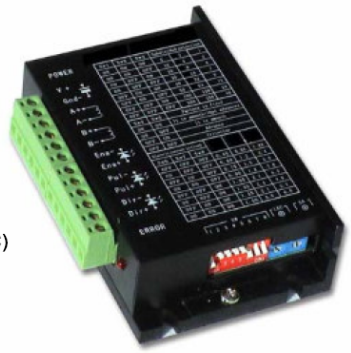

FEATURES:

- thermal protection
- short circuit and wrong polarity protection
- optoisolated signal input
- low vibration, high speed and high torque
- potentiometer LEC for adjustable current reduction
- potentiometer SA for adjustable precision of microstep

PIN- AND SIGNAL-DESCRIPTION:

V+	DC Power Supply 20 .. 80 VDC
GND-	DC Power GND A+,
A-, B+, B-	Motor Connections
ENA-	enable signal, - port
ENA+	enable signal, + port
PUL-	stepper pulse signal input, - port
PUL+	stepper pulse signal input, + port
DIR-	direction signal, - port
DIR+	direction signal, + port

MODE

Mode	SW4	SW5
(1) Itissmooth and Advance	On	On
(2) Itissmooth	On	Off
(3) Advance	Off	On
(4) Criterion	Off	Off

(1) suitable for high current stepper motors
(2) lower running noise
(3) higher torque at middle speed
(4) suitable for all stepper motors

STEP-MODE AND CURRENT ADJUSTMENT:

Step-Mode:

STEP-MODE	SW1	SW2	SW3
1/2	On	On	On
1/4	On	On	Off
1/8	On	Off	On
1/16	On	Off	Off
1/32	Off	On	On
1/64	Off	On	Off

Current:

Current [A]	SW6	SW7	SW8
1.8	Off	Off	Off
2.4	On	Off	Off
3.0	Off	On	Off
3.6	On	On	Off
4.2	Off	Off	On
4.8	On	Off	On
5.7	Off	On	On
6.0	On	On	On

Figure B.2. Specifications of the step motor driver

Specifications of the Data Acquisition Platform

The data acquisition platform is a type of National Instruments BNC-2110. It can be used with M Series, E Series, or S Series multifunction data acquisition (DAQ) devices and NI analog output devices. The NI BNC-2110 connector block simplifies the connection of analog signals, some digital signals, and two user-defined connections to the DAQ device while maintaining the integrity of the measurements with a shielded enclosure.

Specifications of the Data Acquisition Cable

The specifications of the data acquisition cable are listed below:

- Connects screw latching DAQCard devices to 68-pin accessories
- 0.5 m, 1 m, and 2 m lengths
- Shielded I/O cable
- For use with bottom PCMCIA slots

Specifications of the Data Acquisition Card

The data acquisition card is a 6036e National Instruments card. The specifications of the data acquisition card are listed below:

- 16 analog inputs (16-bit, 200 kS/s)
- 2 analog outputs (16-bit, 1 kS/s); 8 DIO; 24-bit counters
- Consider NI M Series multifunction DAQ for USB for higher performance and built-in connectivity
- Use with the NI LabVIEW PDA Module for handheld data acquisition applications
- Compatible with NI LabVIEW, LabWindows™/CVI, and Measurement Studio for Visual Studio
- NI-DAQmx driver software and NI LabVIEW SignalExpress LE interactive data-logging software

Specifications of the Laptop Computer

- Toshiba Intel® Centrino® Processor Technology
- 1.73 GHz

- 500 MB Ram
- 4 Gb memory

Specifications of the Desktop Computer

- Intel Q8200 3 GHz
- 250 Ggb Hdd 7200 rpm
- 4 Ggb DDR 2 RamToshiba Intel® Centrino® Processor Technology
- 22'' LCD Screen

APPENDIX C

TECHNICAL DRAWINGS OF EXPERIMENTAL INSTRUMENTATION

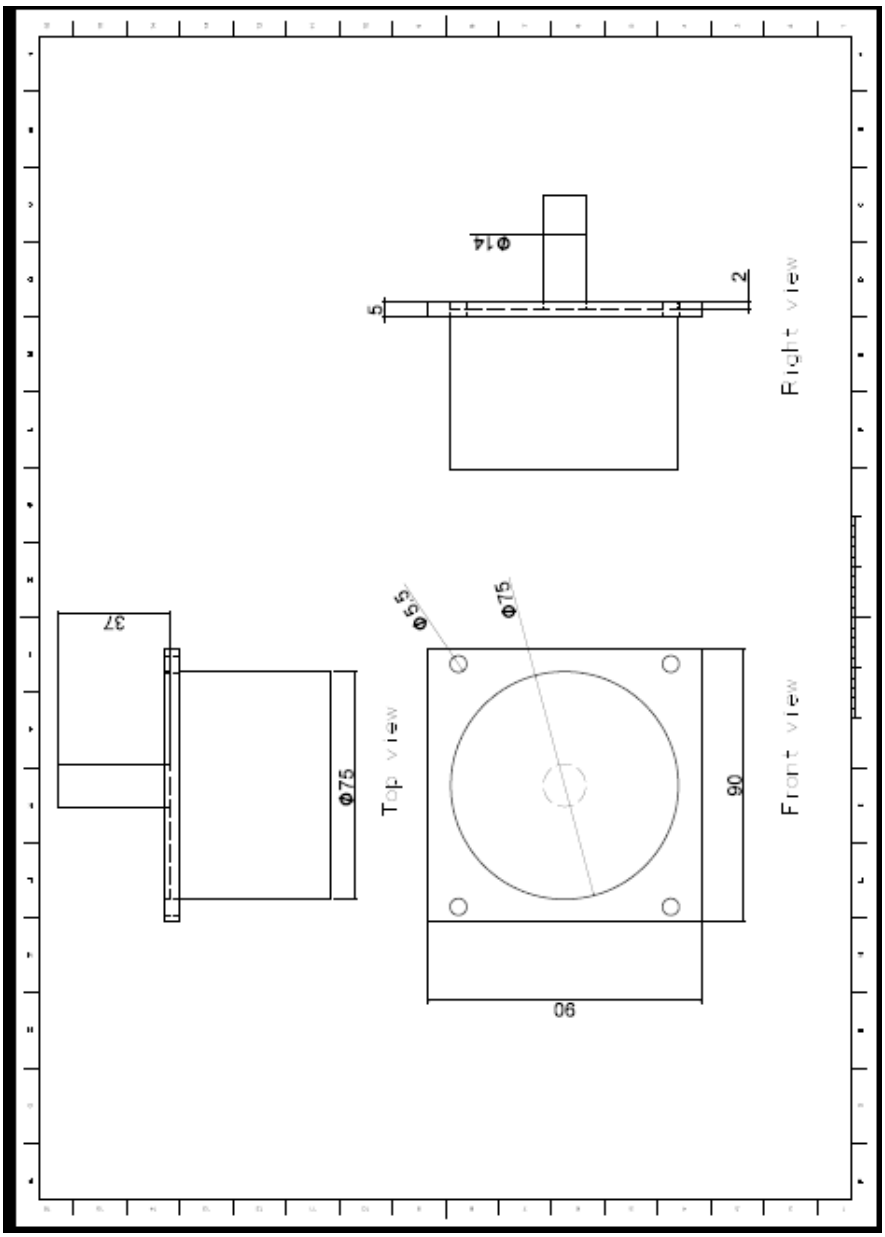

Figure C.1. Technical drawing of step motor

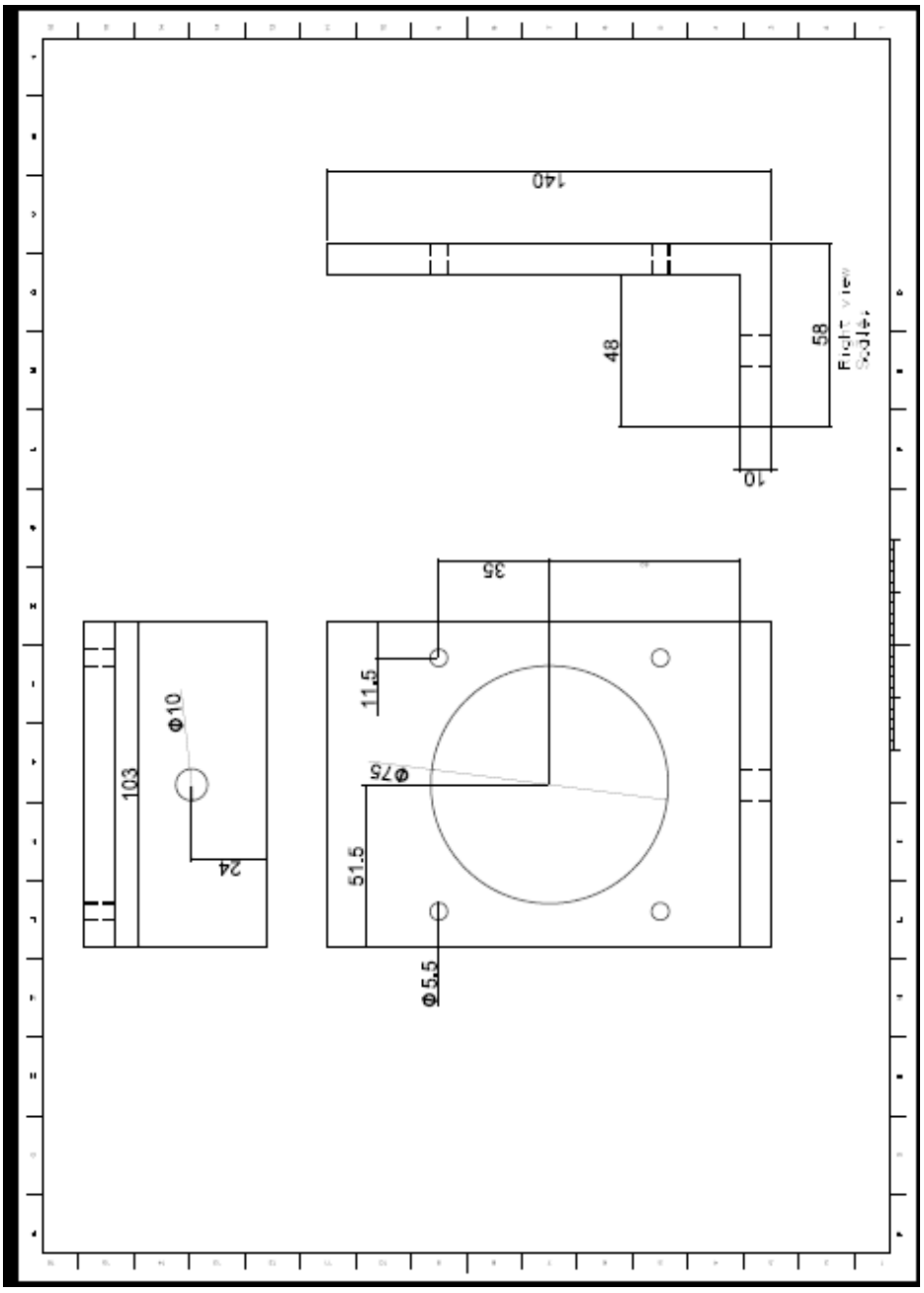

Figure C.2. Technical drawing of step motor casing

.

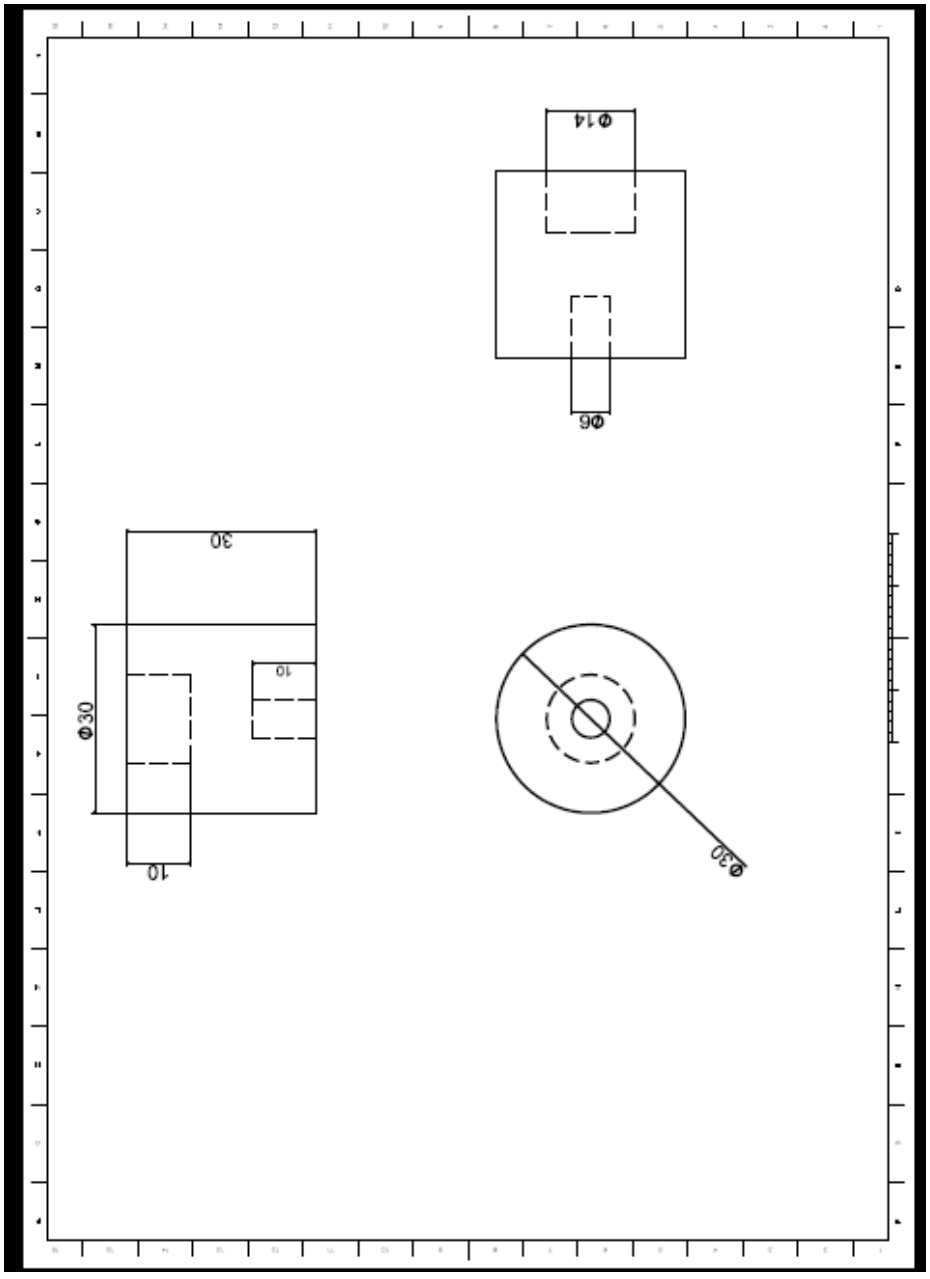

Figure C.3. Technical drawing of coupling

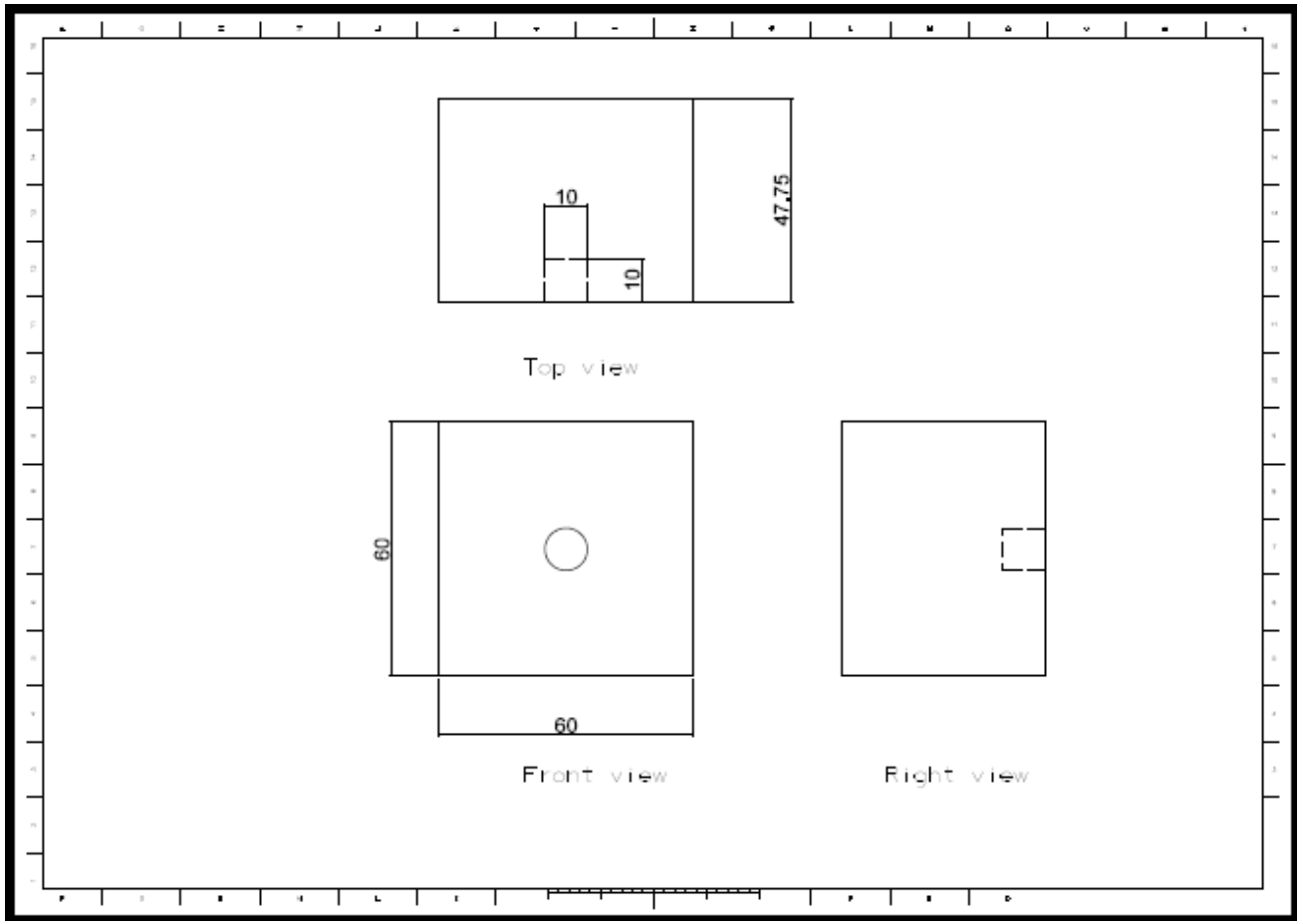

Figure C.4. Technical drawing of magnetic base

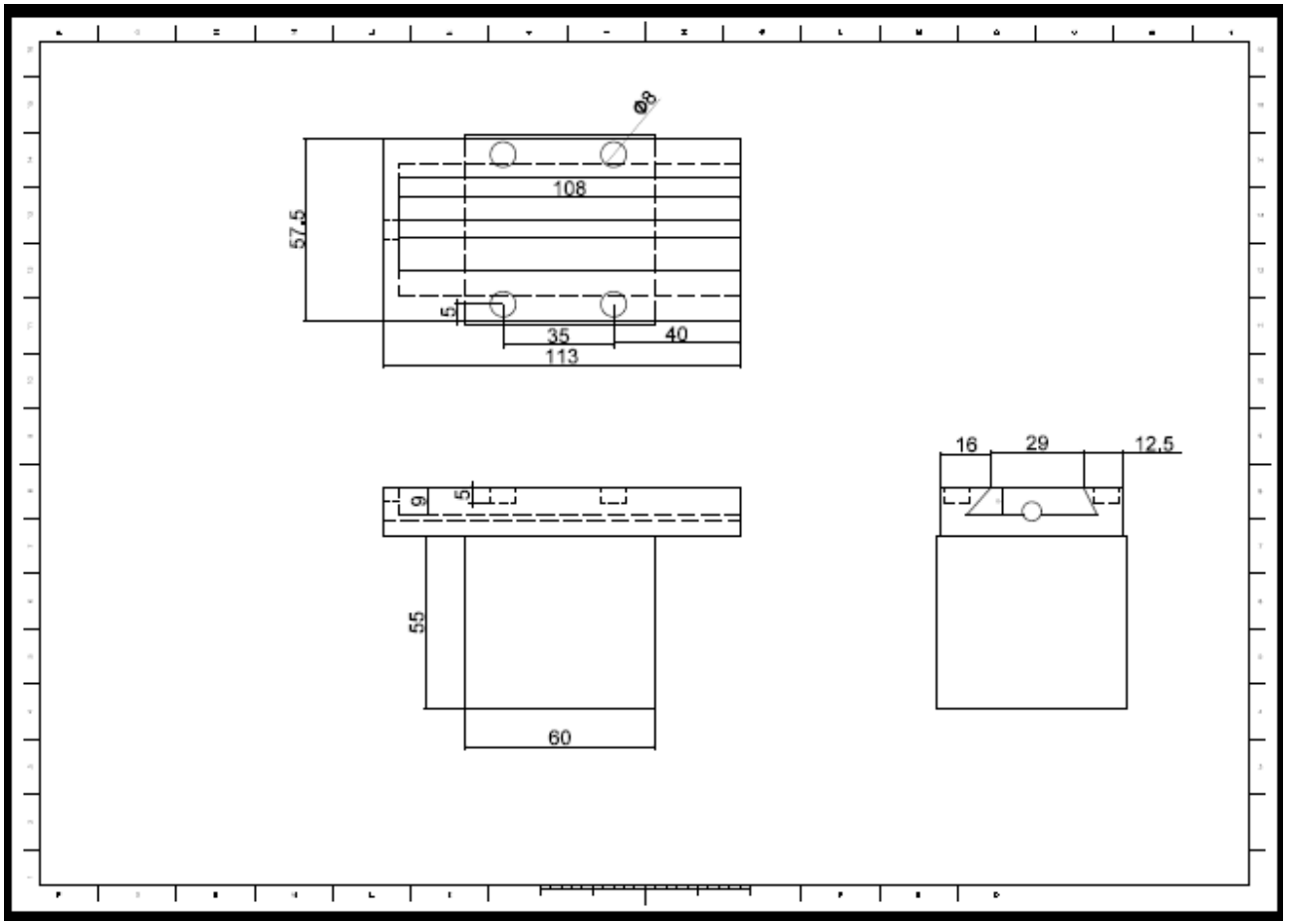

Figure C.5. Technical drawing of lateral motion carraige

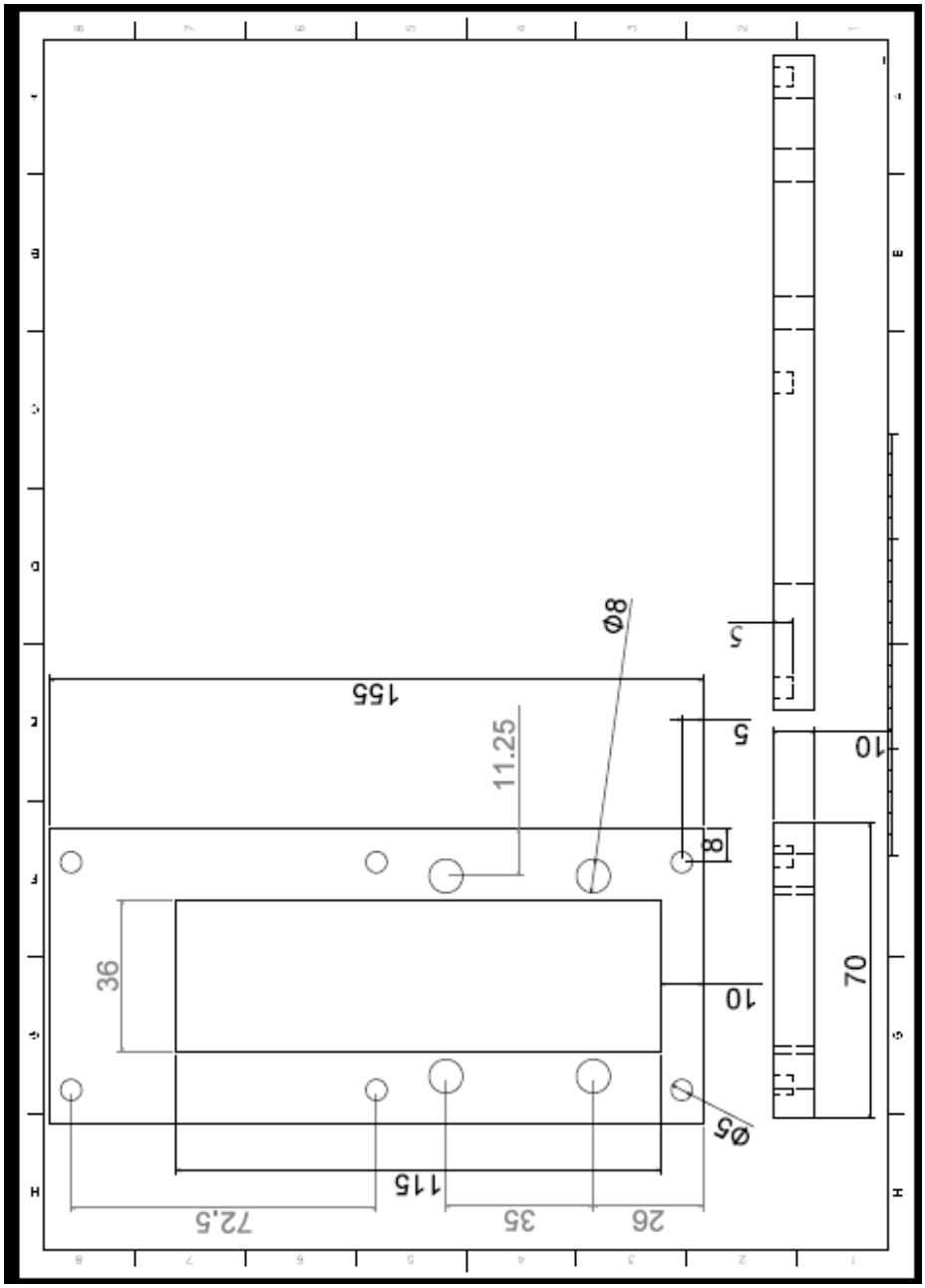

Figure C.6. Technical drawing of first plate

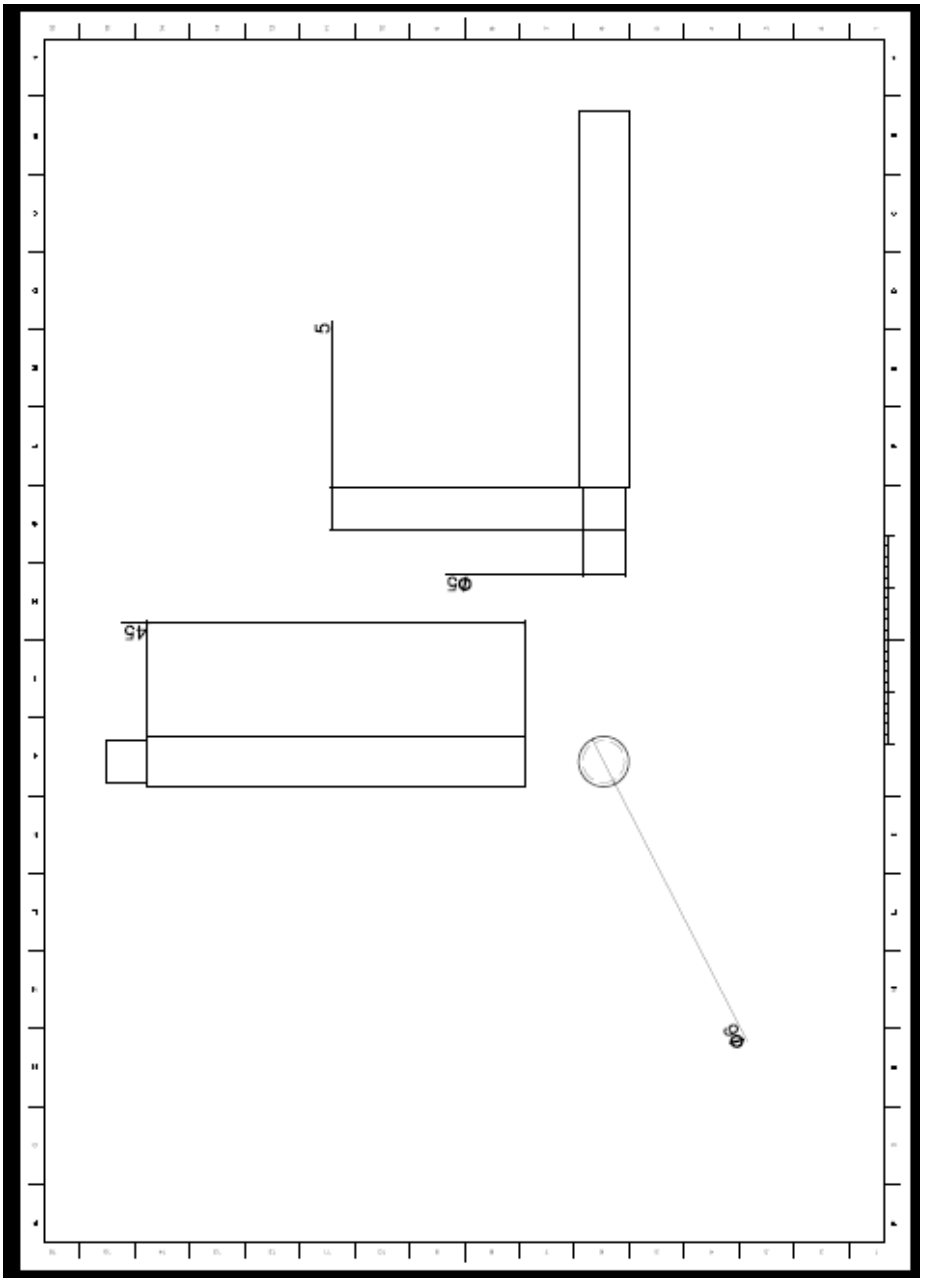

Figure C.7. Technical drawing of guide rails

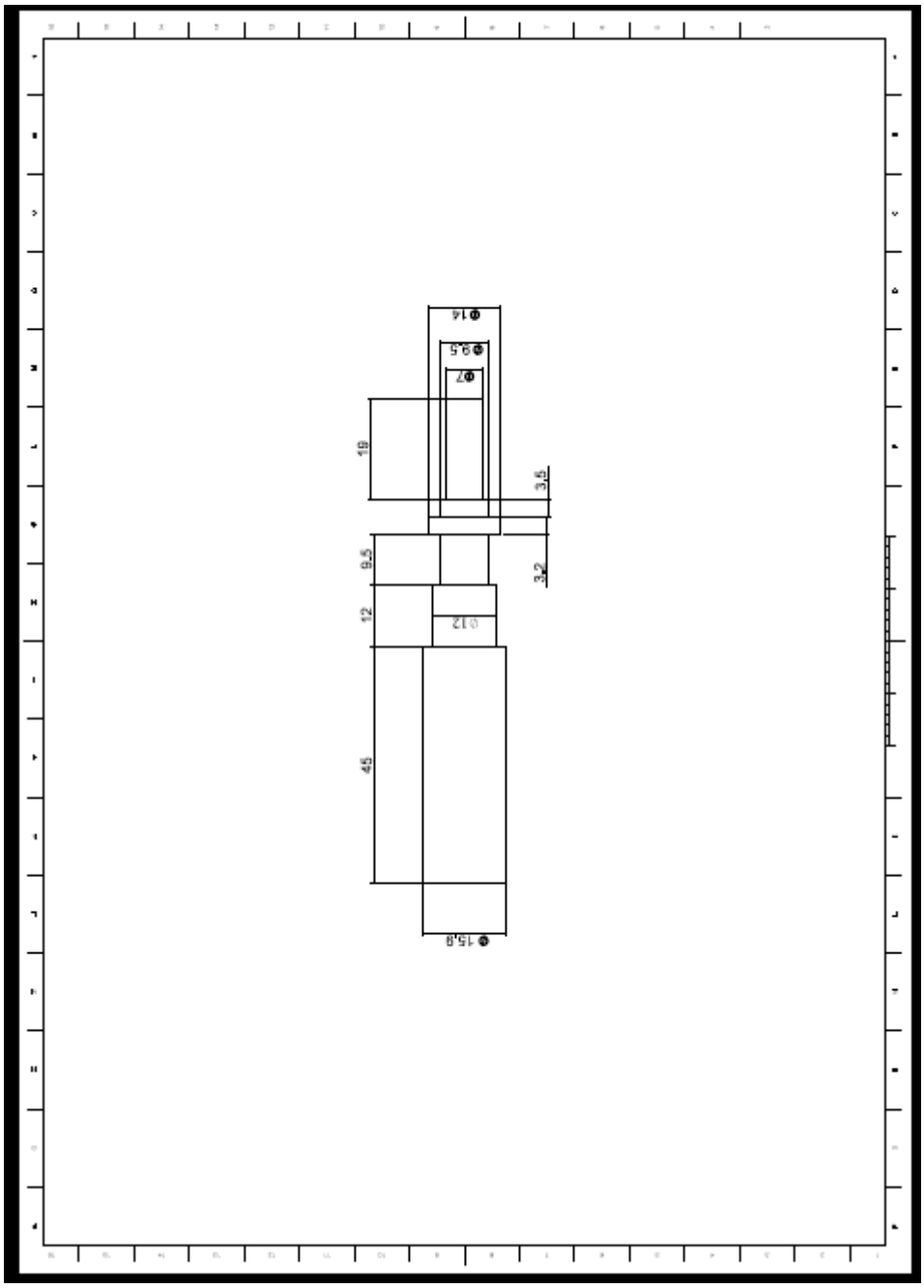

Figure C.8. Technical drawing of micrometer

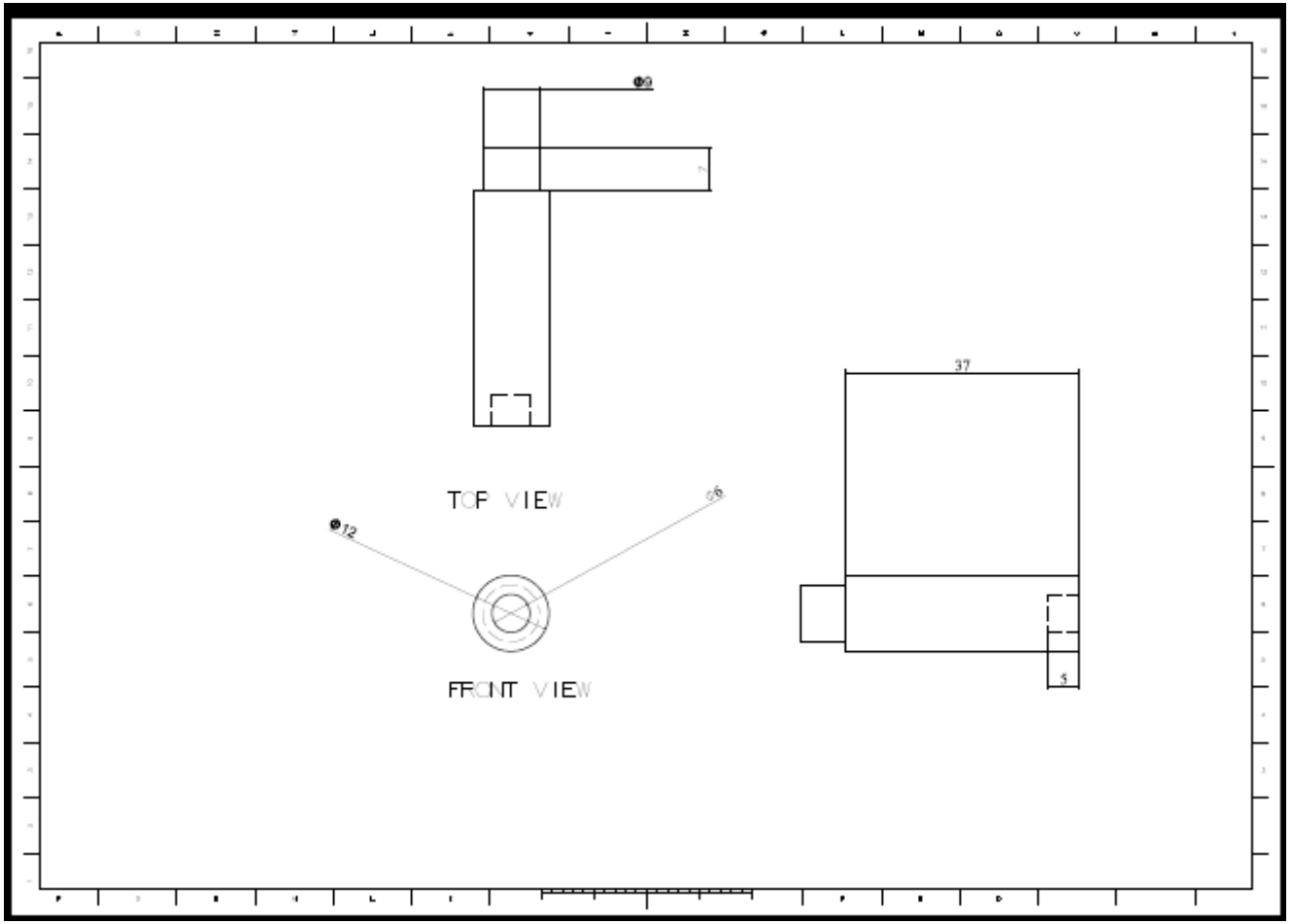

Figure C.9. Technical drawing of shaft

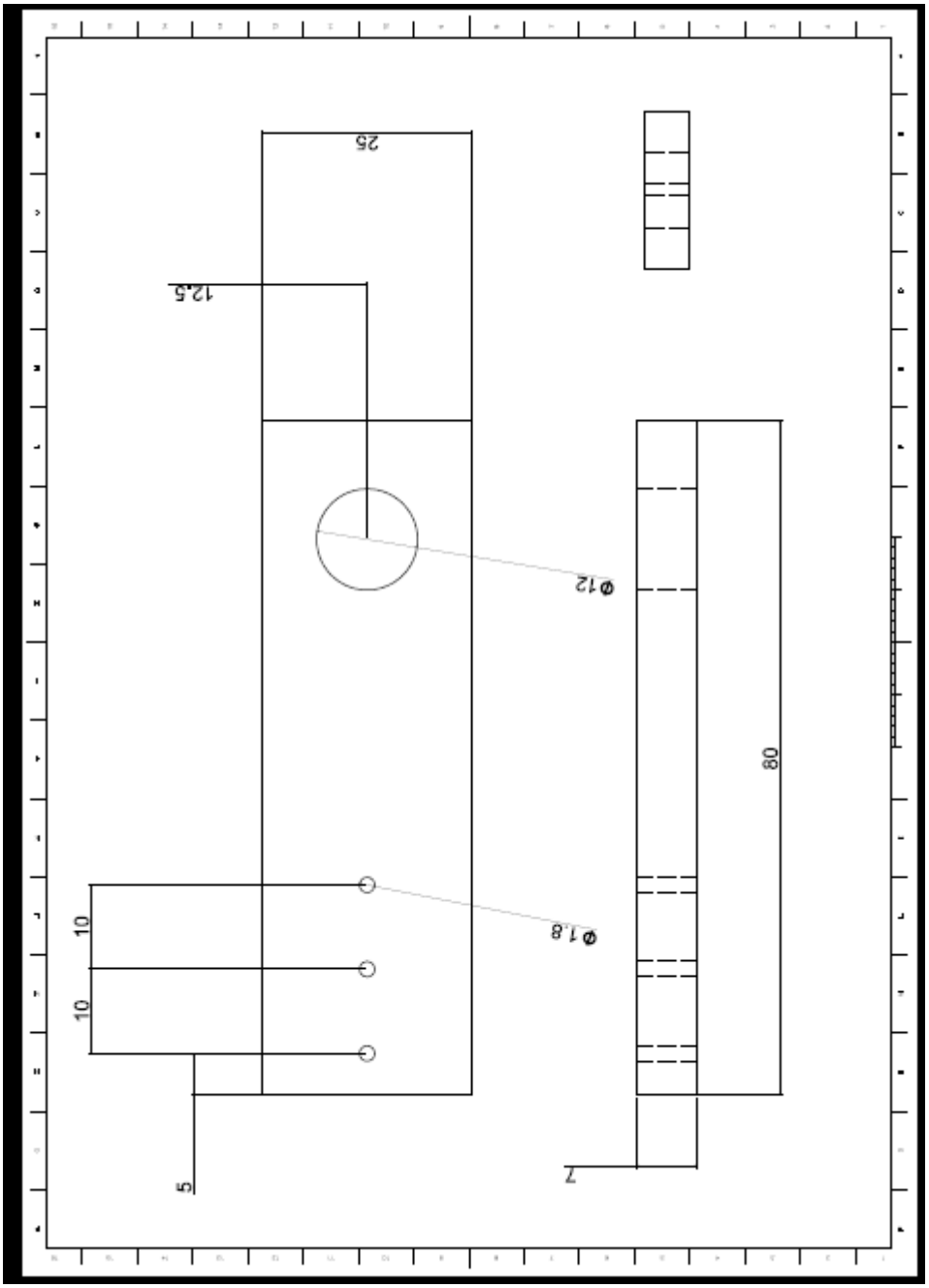

Figure C.10. Technical drawing of third plate

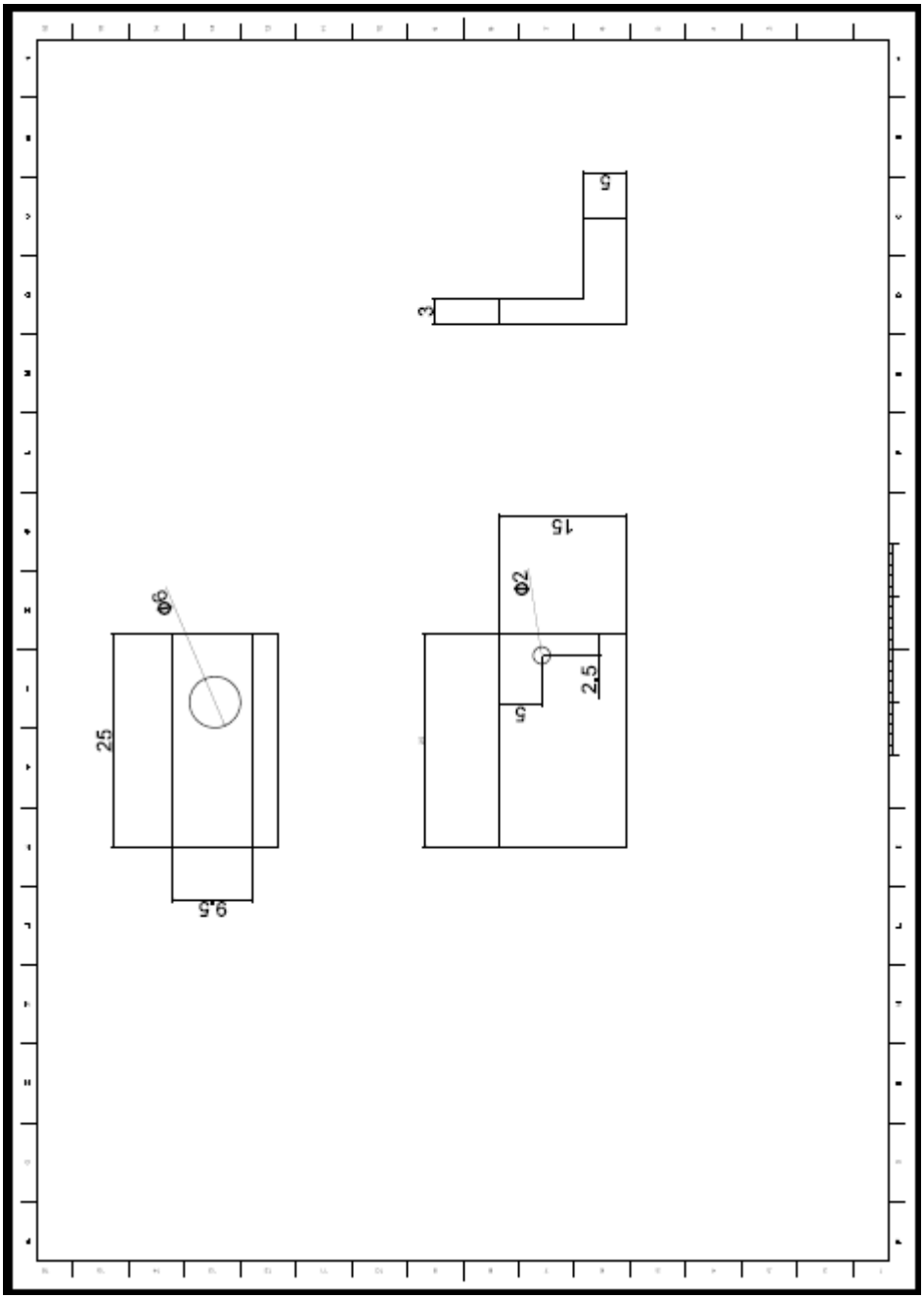

Figure C.11. Technical drawing of encoder probe holder

,

APPENDIX D

NUMERICAL CODE I

D.1. Numerical Code I

```
function [yscosinus] = surface5(input,ymaxlimin,yminlimin)

a=0;
b=0;
mic=0;
mac=0;
mini=[];
maxi=[];
xminnew=[];
xmaxnew=[];
ys=[];
ys(1)=0;

for i = 1:length(input)
    if input(i) > ymaxlimin && mac==0
        a = a+1;
        mic=0;
        mac=1;
        maxi(a)=i;
    end


    if input(i) < yminlimin && mic==0
        b = b+1;
        mic=1;
        mac=0;
        mini(b)=i;
    end
end

[ymax,xmax,k]=maxfind(input,maxi,mini,ymaxlimin,a,b);


[ymin,xmin,l]=minfind(input,maxi,mini,yminlimin,a,b);

[yscosinus]=cosinussurface5(xmax,xmin,k,l,input);




end
```

```
function [ymax,xmax,k]
=maxfind(input,maxi,mini,ymaxlimin,a,b,xmaxi)


    k=0;
    if maxi(1)<mini(1)
    if a==b
        for i=1:a
            ymaxi=ymaxlimin;
        for j=maxi(i):mini(i)
            if input(j+1)>ymaxi
                ymaxi=input(j+1);
                xmaxi=j+1;
            end
        end
        ymax(i)=ymaxi;
        xmax(i)=xmaxi;
        k=k+1;
    end
    end
    if a>b
        for i=1:min(a,b)
              ymaxi=ymaxlimin;
        for j=maxi(i):mini(i)
            if input(j+1)>ymaxi
                ymaxi=input(j+1);
                xmaxi=j+1;
            end
        end
        ymax(i)=ymaxi;
        xmax(i)=xmaxi;
        k=k+1;
        end


    for i=max(a,b):max(a,b)
          ymaxi=ymaxlimin;
        for j=maxi(i):(length(input)-1)
            if input(j+1)>ymaxi
                ymaxi=input(j+1);
                xmaxi=j+1;
            end
        end
        ymax(i)=ymaxi;
        xmax(i)=xmaxi;
        k=k+1;
    end

    end
    end

    if maxi(1)>mini(1)
    if a==b
        for i=1:(a-1)
```

```
            ymaxi=ymaxlimin;
    for j=maxi(i):mini(i+1)
        if input(j+1)>ymaxi
            ymaxi=input(j+1);
            xmaxi=j+1;
        end
    end
    ymax(i)=ymaxi;
    xmax(i)=xmaxi;
    k=k+1;
    end
for i=max(a,b):max(a,b)
       ymaxi=ymaxlimin;
    for j=maxi(i):(length(input)-1)
        if input(j+1)>ymaxi
            ymaxi=input(j+1);
            xmaxi=j+1;
        end
    end
    ymax(i)=ymaxi;
    xmax(i)=xmaxi;
    k=k+1;
end
end
if a<b
    for i=1:min(a,b)
            ymaxi=ymaxlimin;
    for j=maxi(i):mini(i+1)
        if input(j+1)>ymaxi
            ymaxi=input(j+1);
            xmaxi=j+1;
        end
    end
    ymax(i)=ymaxi;
    xmax(i)=xmaxi;
    k=k+1;
    end
end
end
```

```
function [ymin,xmin,l] = minfind(input,maxi,mini,yminlimin,a,b,l)
 l=0;
 ymini=yminlimin;

    if maxi(1)>mini(1)
    if a==b
        for i=1:a
             ymini=yminlimin;
        for j=mini(i):maxi(i)
            if input(j+1)<ymini
                ymini=input(j+1);
                xmini=j+1;
            end
        end
        ymin(i)=ymini;
        xmin(i)=xmini;
        l=l+1;
    end
    end
    if b>a
        for i=1:min(a,b)
             ymini=yminlimin;
        for j=mini(i):maxi(i)
            if input(j+1)<ymini
                ymini=input(j+1);
                xmini=j+1;
            end
        end
        ymin(i)=ymini;
        xmin(i)=xmini;
        l=l+1;
        end


    for i=max(a,b):max(a,b)
         ymini=yminlimin;
        for j=mini(i):(length(input)-1)
            if input(j+1)<ymini
                ymini=input(j+1);
                xmini=j+1;
            end
        end
        ymin(i)=ymini;
        xmin(i)=xmini;
        l=l+1;
    end

    end
    end

    if maxi(1)<mini(1)
    if a==b
        for i=1:(a-1)
             ymini=yminlimin;
        for j=mini(i):maxi(i+1)
```

```
        if input(j+1)<ymini
            ymini=input(j+1);
            xmini=j+1;
        end
    end
    ymin(i)=ymini;
    xmin(i)=xmini;
    l=l+1;
end
end
if a>b
    for i=1:min(a,b)
         ymini=yminlimin;
    for j=mini(i):maxi(i+1)
        if input(j+1)<ymini
            ymini=input(j+1);
            xmini=j+1;
        end
    end
    ymin(i)=ymini;
    xmin(i)=xmini;
    l=l+1;
    end
end
end
```

```
function [ys] =cosinussurface5 (xmax,xmin,k,l,input)

m=1;
n=1;
mac=0;
ys=[];
cons1=1.55/(4*pi);
cons2=1.55/4;


if xmax(1)<xmin(1)
    yref=0;
    xminnew(1)=xmin(1);
    for i=1:l
        xminnew(i+1)=xmin(i);
    end
    for i=1:(length(input))

    if i~=xmax(m) && i~=xminnew(n)
        if mac==0;
            A=(input(xmax(m))+input(xminnew(n)))/2;
            B=(input(xmax(m))-input(xminnew(n)))/2;
            ys(i)=yref+cons2-(acos((input(i)-A)/B)*cons1);
        else if mac==1
            A=(input(xmax(m))+input(xminnew(n)))/2;
            B=(input(xmax(m))-input(xminnew(n)))/2;
            ys(i)=yref+(acos((input(i)-A)/B)*cons1);
      %eski kod        ys(i+1)=ys(i)+((acos((input(i+1)-
((input(xmax(m))+input(xminnew(n)))/2))/((input(xmax(m))-
input(xminnew(n)))/2))-acos((input(i)-
((input(xmax(m))+input(xminnew(n)))/2))/((input(xmax(m))-
input(xminnew(n)))/2)))/pi*1.55/4);
            end
        end
    else if i==xmax(m)
            ys(i)=yref+cons2;
            yref=yref+cons2;
            n=n+1;
            if mac==0
                mac=1;
            else if mac==1
                    mac=0;
                end
            end
            if n>l+1
                n=n-1;
            end


        else if i==xminnew(n)
                ys(i)=yref+cons2;
                yref=yref+cons2;
                m=m+1;
                if mac==0
                    mac=1;
```

```
                else if mac==1
                        mac=0;
                    end
                end
                if m>k
                    m=m-1;
                end

            end
        end
    end
    end


else if xmax(1)>xmin(1)
        yref=0;
 xmaxnew(1)=xmax(1);
    for i=1:k
        xmaxnew(i+1)=xmax(i);
    end
    for i=1:(length(input))

    if i~=xmaxnew(m) && i~=xmin(n)
        if mac==0;
           A=(input(xmaxnew(m))+input(xmin(n)))/2;
            B=(input(xmaxnew(m))-input(xmin(n)))/2;
            ys(i)=yref+(acos((input(i)-A)/B)*cons1);
        else if mac==1
             A=(input(xmaxnew(m))+input(xmin(n)))/2;
            B=(input(xmaxnew(m))-input(xmin(n)))/2;
            ys(i)=yref+cons2-(acos((input(i)-A)/B)*cons1);
            end
        end
    else if i==xmaxnew(m)
             ys(i)=yref+cons2;
            yref=yref+cons2;
            n=n+1;
            if mac==0
                mac=1;
            else if mac==1
                    mac=0;
                end
            end
            if n>1
                n=n-1;
            end


        else if i==xmin(n)
                ys(i)=yref+cons2;
                yref=yref+cons2;
                m=m+1;
                if mac==0
                    mac=1;
                else if mac==1
                        mac=0;
                    end
```

```
                end
                if m>k+1
                    m=m-1;
                end

            end
        end
    end
    end
    end
end

end
```

APPENDIX E

SPREADING OF THE LUBRICANT

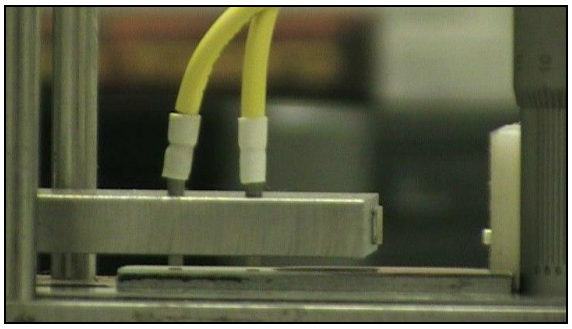

(a) Δt=60 minutes

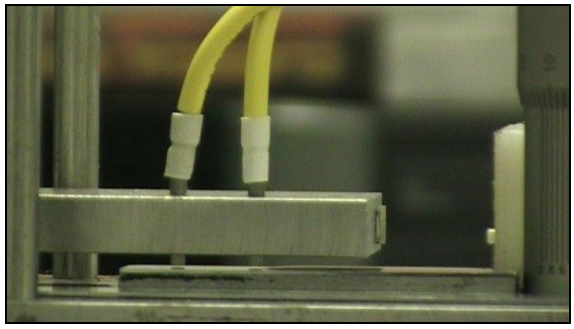

(b) Δt=80 minutes

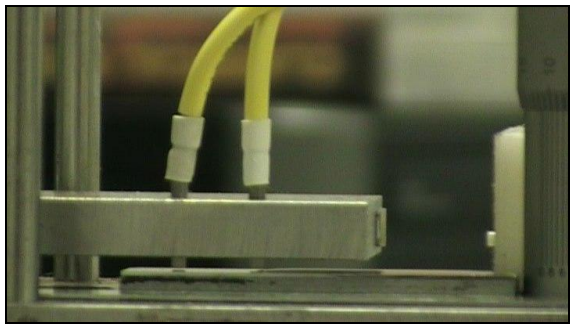

(c) Δt=90 minutes

Figure E.1. Spreading of the lubricant at different times

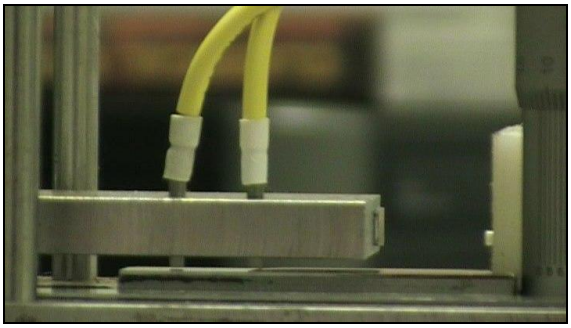

(d) Δt=100 minutes

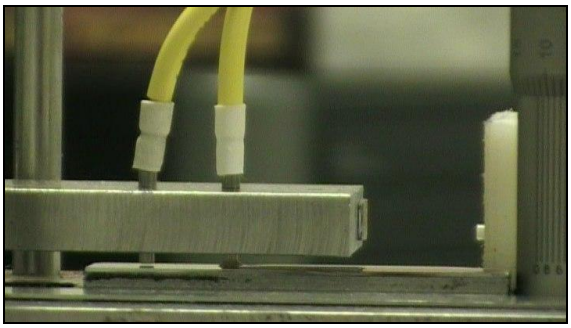

(e) Δt=110 minutes

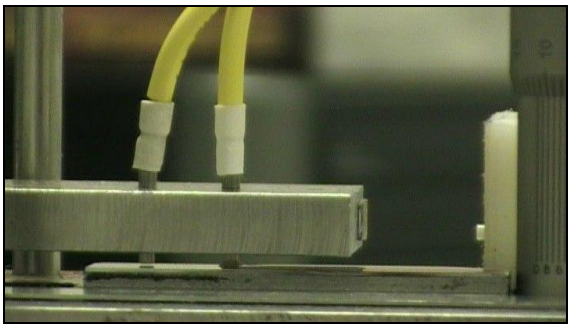

(f) Δt=111 minutes

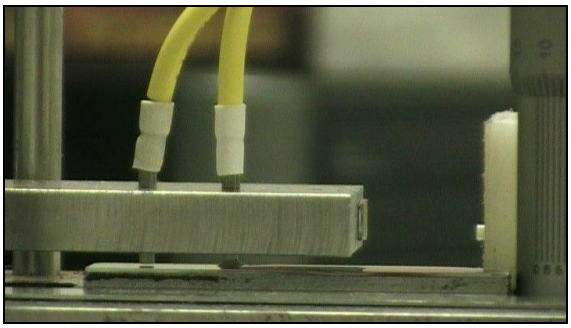

(g) Δt=112 minutes

Figure E.1. Spreading of the lubricant at different times (continued)

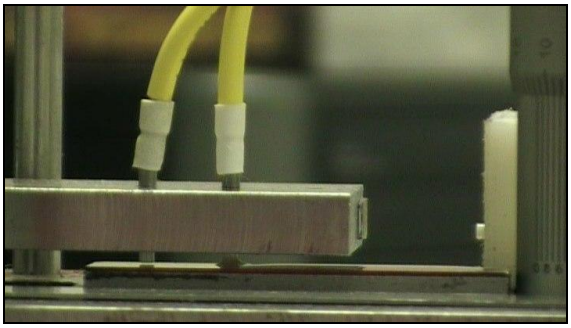

(h) Δt=115 minutes

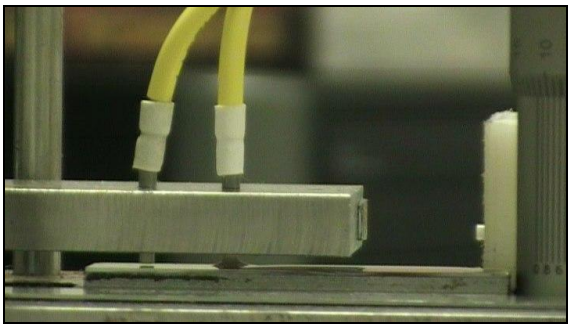

(i) Δt=120 minutes

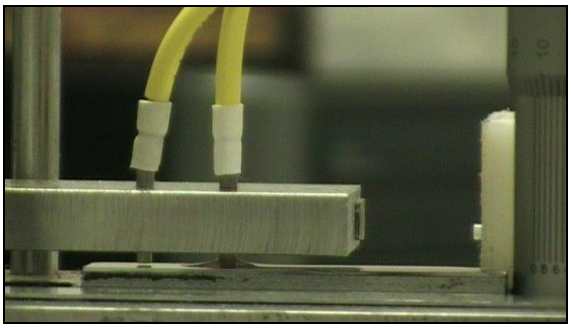

(j) Δt=130 minutes

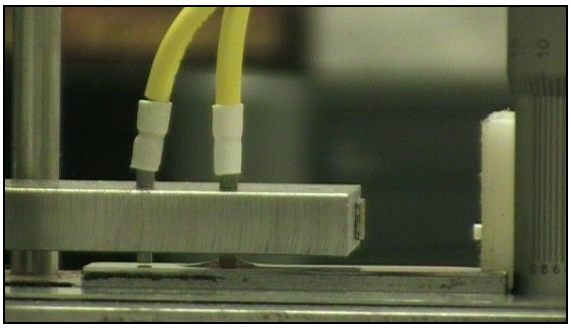

(k) Δt=140 minutes

Figure E.1. Spreading of the lubricant at different times (continued)

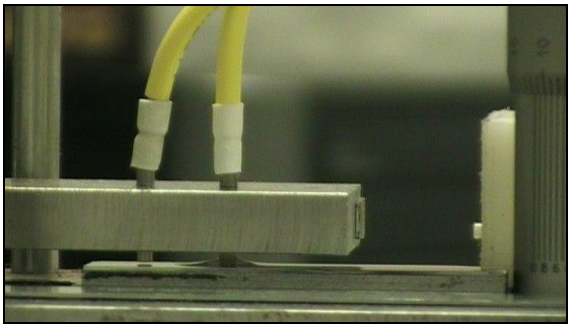

(l) Δt=150 minutes

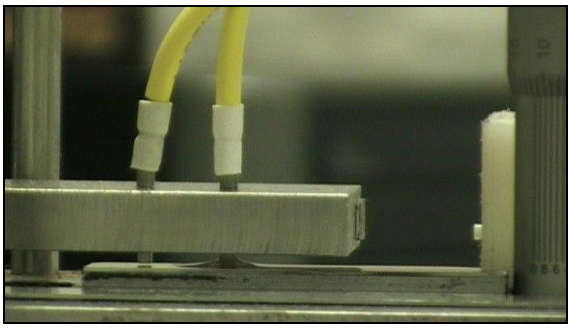

(m) Δt=160 minutes

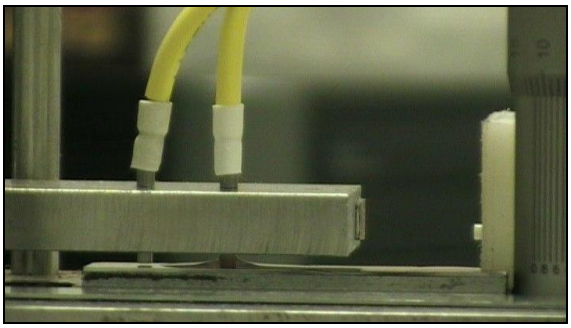

(n) Δt=180 minutes

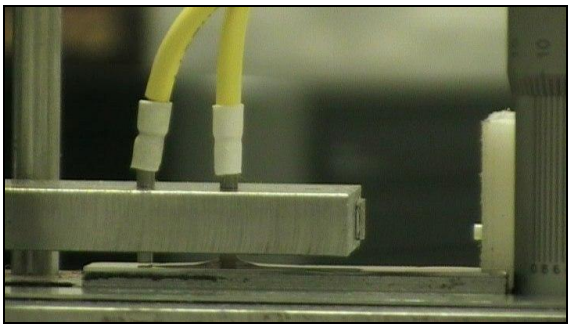

(o) Δt=190 minutes

Figure E.1. Spreading of the lubricant at different times (continued)

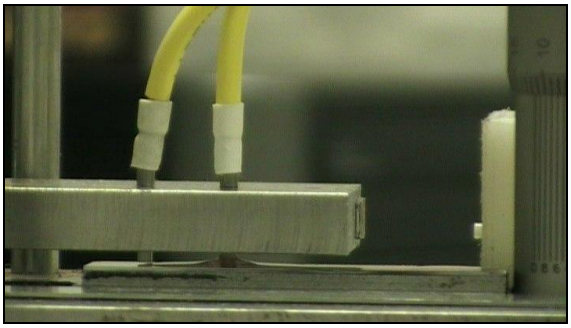

(p) Δt=200 minutes

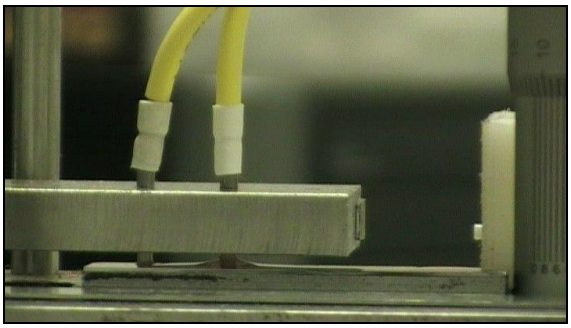

(r) Δt=210 minutes

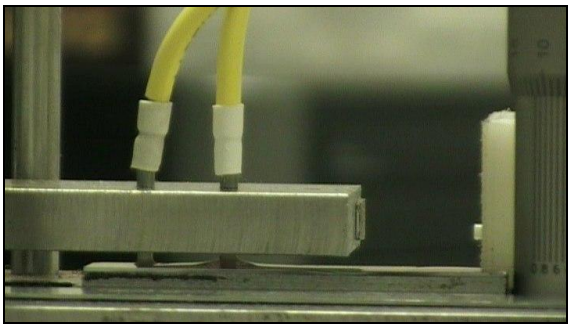

(s) Δt=211 minutes

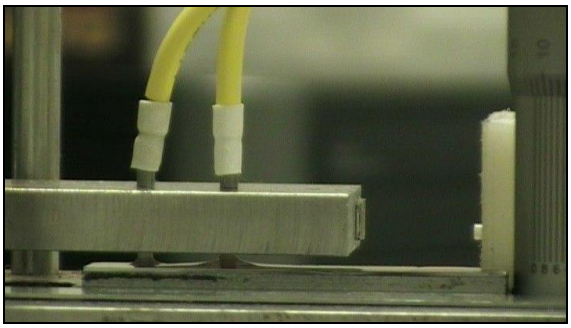

(t) Δt=212 minutes

Figure E.1. Spreading of the lubricant at different times (continued)

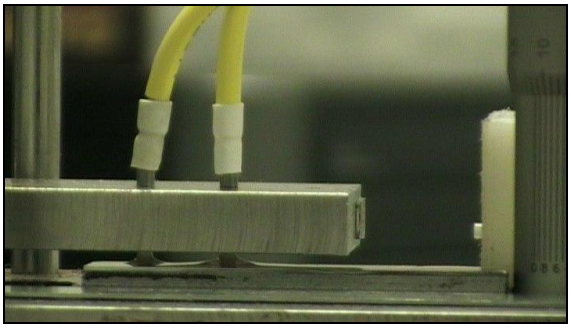

(u) Δt=213 minutes

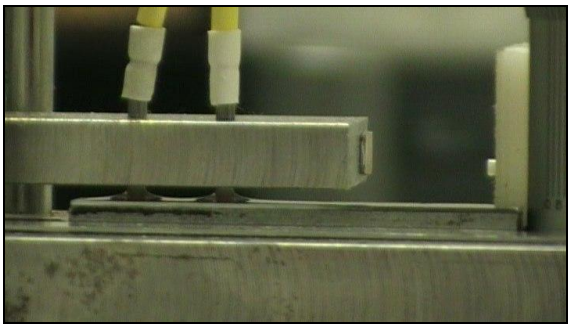

(v) Δt=240 minutes

Figure E.1. Spreading of the lubricant at different times (continued)

The injection process is performed on the right hand side of the probes where there is a gap between third plate and the encoder probe. The duration of the diffusion of the lubricant is 3.5-4 hours. When the lubricant comes closer to a probe 5 (at the right hand side probe) and it touches, it starts to rise on to the probe 5. After some time passes, then the lubricant continues to the diffusion motion to the probe 3. When it touches to the probe 3, again it starts to rise and after some time the lubricant diffuses to the whole gold coated mirror. The thickness of the lubricant is approximately 100 μm. However, since the most of the lubricant is piled up around the probe surfaces, the lubricant thickness is varying throughout the gold coated mirror.

APPENDIX F

NUMERICAL CODE II

```
function [hx1,hx2] = mikrometre(A,B,x1,N)
L=140;
b=A;
a=(B-b)/L;
x2=x1+(0.9*N);
hx1=a*x1+b;
hx2=a*x2+b;
end
```

%A: Height difference between left micrometer and the reference setting(if A is positive, micrometer is turned into the clockwise direction, if it is negative micrometer is turned into the counter clockwise direction)

%B: Height difference between right micrometer and the reference setting

%x1: x location of the probe at the beginning (units of mm) with respect to the left micrometer

%N: number of revolutions of the step motor

%L: distance between the two micrometers(units of mm)

%x2: x location of the probe at the end (units of mm) with respect to the left micrometer

%hx1: height difference between the probe and the reference setting at the beginning

%hx2: height difference between the probe and the reference setting at the end

%h(x)=a*x+b gives the x location of the probe during the experiment

% a,b: coefficients of the h(x)

APPENDIX G

MOVING AVERAGE METHOD

The moving average method is equivalent to low pass filtering with the response of the smoothing given by the difference equation.

$$y_s(i) = \frac{1}{2*N+1} * (y(i+N) + y(i+N-1) + ... + y(i-N)) \qquad \text{(G.1)}$$

Where $y_s(i)$ is the smoothed value for the i th data point , N is the number of neighboring data points on either side of $y_s(i)$, 2N+1 is the span size.

The moving average smoothing method follows these rules:

- The span must be odd.
- The data point to be smoothed must be at the center of the span.
- The span is adjusted for data points that cannot accommodate the specified number of neighbors on either side.
- The end points are not smoothed because a span cannot be defined.

APPENDIX H

EXCEL CODE

Input Parameters:

Back reflection percentage (R_1) : 0.035

Coherent Length of the laser (L) : 100 m

Wavelength of the laser (λ) : 1550 nm

Diameter of the fiber optic cable (D) : 9 μm

Numerical aperture of the fiber optic cable (α) : 7 °

The detected density can be calculated with the Equation H.1.

$$I = I_0 \times (R_1 + (1-R_1)^2 \times R + 2 \times (1-R_1) \times \sqrt{R \times R_1} \times \frac{\sin(\varepsilon)}{\varepsilon} \times \cos(4 \times \pi \times \frac{x_0}{\lambda})) \quad \text{(H.1)}$$

where

$R = (1\text{-}R_1)*(D/(D+(2*x*\tan(\alpha))))^2$

$\varepsilon = \pi*x/L$

The detected intensity versus gap between the fiber optic end and the reflector is shown in Figure H.1.

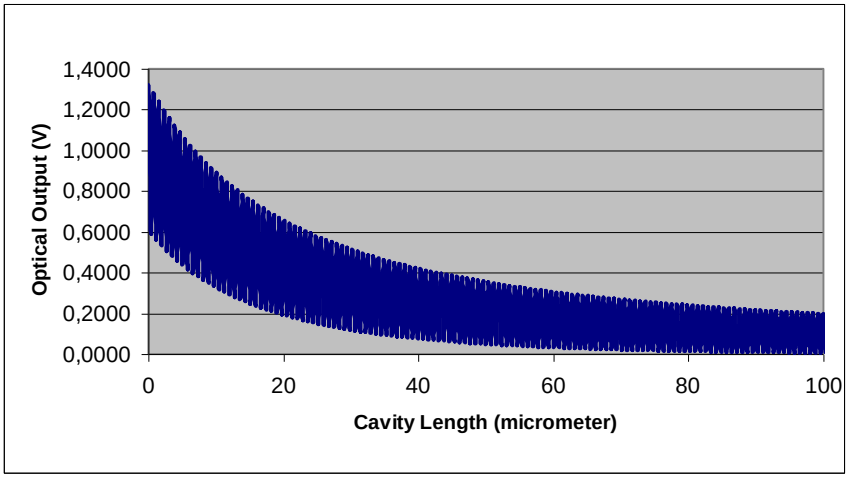

Figure H.1 The detected intensity versus gap length